Dr Florence Cavalli June 2017

Final progress report for the Stephen Buttrum Brain Tumour Research Fellowship

Summary of the outcome of my research project (2014-2016 fellowship postponed to 2017 due to maternity leave)

My prostdoctoral research project studies aimed at increasing our understanding of medulloblastoma (MB) tumours investigating characteristics within and between MB tumours. This work contributes to the foundation needed for further work for the discovery of new and more specific drugs and treatments. During my postdoctoral fellowship I focused on two main projects; investigating the (i) spatial heterogeneity and the (ii) intertumoural heterogeneity of primary MB tumours.

1) Spatial heterogeneity

This project is in collaboration with Dr A. Sorana Morrissy and Dr. Marc Remke. To determine the degree and clinical importance of the spatial heterogeneity, i.e differences between physically isolated biopsies of a single tumour, we analyzed multiple biopsied obtained for 9 MBs, 16 High Grade Gliomas (HGGs) and 10 Renal Cell Carcinomas (RCCs).

First, we were able to show that MB subgrouping -the classification of the tumour to a WNT, SHH, Group3 or Group 4 subgroup- using gene expression data is stable regardless of the primary biopsy used to define the subgroup. This reinforces the clinical relevance and importance of sample subgrouping. However this was not the case for most of the Glioblastoma (GBM, part of HGGs) samples we analysed. Different biopsies of the same tumour could be classified to different GBM subtypes, showing a larger intra tumoural heterogeneity in GBM than in MB.

We them explore the intratumoural heterogeneity at the genomic level somatic identifying copy number variants and mutation present in the different biopsies of the tumours. We found a range of heterogeneity levels among the samples, some samples being more homogeneous with somatic mutations and/or copy number variants present in all or most of the biopsies and others being more heterogeneous with many somatic mutations and/or copy number variants present only in a subset of biopsies or in a single biopsy coming from the tumours. We further show and proposed that at least two biopsies should be taken to estimate if a tumour is more likely more homogenous or heterogeneous.

Next, we focused on genes suitable for targeted therapeutics and observed that somatic mutations that affect those genes demonstrated high levels of spatial heterogeneity. Therefore, the extent of the spatial heterogeneity of somatic mutations observed in our

cohort suggests that clinical trials of molecularly targeted therapy should first assess the ubiquitous distribution of the target. The lack of actionable driver mutations that are ubiquitously present across all regions of a given brain tumour suggests that monotherapies that target a single gene from a single biopsy are unlikely to have dramatic effects in terms of improving the lives of patients with brain tumours.

Finally we observed that in MBs the expression of antigenes/genes that are the target of new immunotherapy that are currently being developed have a remarkable consistency of expression across multiregional biopsies. We concluded that this is a promising way to overcome the intratumoural heterogeneity observed in MB tumours.

This study has been published in May 2017 in the Nature Genetics journal. The full article is attached at the end of this report.

2) Intertumoural heterogeneity

This project is in collaboration with Dr. Marc Remke. In the second project we aimed at further investigating the intertumoural heterogeneity (i.e between patient samples) especially the heterogeneity observed inside each of the four MB subgroups. Indeed, it is accepted that MB comprises four distinct molecular variants, and current clinical trials are stratifying patients using a combined biological and clinical risk stratification. However inside each subgroup, we observe tremendous clinical heterogeneity suggesting additional substructure. What remained unclear was the degree of biological substructure within subgroups.

To investigate this, we generated a large dataset comprised of 763 primary MB samples for which we obtained both array-based gene expression and methylation data. Looking for group of samples more similar to each other inside each subgroups using either the gene expression or the methylation returned discordant results since different groups were obtained in function of the data type used. Since we wanted to use information present in both data types to discover clinically relevant groups, we took an integrative clustering approach to integrate the data. We therefore performed an integrative analysis of 763 primary MB samples with gene expression and genome-wide DNA methylation data with the Similarity Network Fusion method (SNF) to uncover the structure inside each MB subgroups.

The integrative clustering faithfully recapitulated the core subgroups with a clear boundary between Group 3 and 4, that is not readily apparent by either expression or methylation alone. A subsequent analysis within each subgroup revealed varying degrees of biological heterogeneity. After integration of somatic copy number alterations and clinical features, **we identified twelve medulloblastoma subtypes with clear clinical and molecular characteristics; two WNT, four SHH, three Group 3 and three Group 4 subtypes**. These subtypes are important clinically since they present distinct clinical outcome and/or distinct molecular characteristics at the copy number levels or pathway level for example. Figure 1 present a summary of the keys clinical and cytogenetic events in each of the twelve MB subtypes we identified.

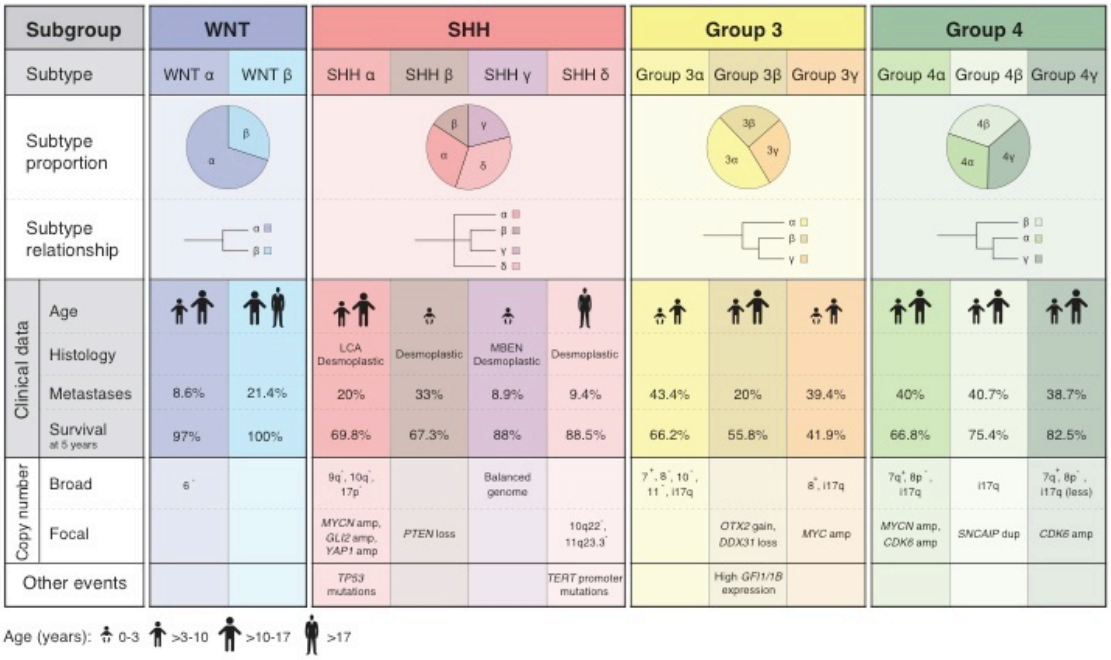

Figure 1: Graphical Summary of the 12 Medulloblastoma Subtypes
Schematic representation of key clinical data, copy-number events, and relationship between the subtypes inside each of the four medulloblastoma subgroups. The percentages of patients presenting with metastases and the 5-year survival percentages are presented. The age groups are: infant 0–3 years, child >3–10 years, adolescent >10–17 years, and adult >17 years.

We discovered two infants SHH subtypes with disparate outcomes and distinct copy number profiles, a childhood subtype with poor prognosis and an adult subtype. Notably, *TP53* mutation is enriched and prognostic only in the childhood SHH subtype. The worst prognosis Group 3 subtype had *MYC* amplicons and isochromosome 17q without other focal aberrations. The other two have more favourable prognosis, one harbours similar focal copy number aberrations as the first one without high level *MYC* amplifications. Pathway analysis revealed subtype specific biological processes and transcriptional networks. For example, we observed an enrichment of developmental pathways in one of the two SHH infant subtypes.

The identification of subtypes has significant biological and clinical implications. Several previously described focal copy-number alterations within MB subgroups as well as several arm-level events clearly segregate between subtypes. Our identification of unique cytogenetic aberrations that occur in concert, as well as specific biological pathways enriched within specific subtypes, will serve to inform creation of rational preclinical models that closely mirror the human diseases. Several of these aberrations are actionable, as defined by the availability of approved drugs, and largely restricted to subtypes. These results will therefore allow follow up studies to further explore the possible use and benefit of particular drugs on the different subtypes. Several subtypes, particularly in SHH and group 3, have clear and drastic clinical and prognostic differences, which will allow for more robust risk stratification in future clinical trials.

As current therapies result in significant long-term neurocognitive and neuroendocrine sequelae, the identification of distinct biological processes within each subgroup allows for more refinement in biological risk stratification as well as the possible identification of novel agents for future targeted therapies.

This study has been published in June 2017 in the Cancer Cell journal. The full article is attached at the end of this report as well as a preview of our paper written by Drs Bavle and Parsons published in the same journal issue.

Financial Statement

Expenses	Amount
Salary	$45,000
Computer Supplies	$4,072.24
Hard drives	$927.76
Total	$50,000

Bibliography

Cavalli FMG[*], Remke M[*], Rampasek L, Peacock J, Shih DJH, Luu B, Garzia L, Torchia J, Nor C, Morrissy AS, Agnihotri S, Thompson YY, Kuzan-Fischer CM, Farooq H, Isaev K, Cho B-K, Kim S-K, Wang K-C, Lee JY, Grajkowska WA, Perek-Polnik M, Vasiljevic A, Faure-Conter C, Jouvet A, Giannini C, Nageswara Rao AA, Li KWK, Ng H-K, Eberhart CG, Pollack IF, Hamilton RL, Gillespie GY, Olson JM, Leary S, Weiss WA, Lach B, Chambless LB, Thompson RC, Cooper MK, Vibhakar R, Hauser P, van Veelen M-LC, Kros JM, French PJ, Shin Ra Y, Kumabe T, López-Aguilar E, Zitterbart K, Sterba J, Finocchiaro G, Massimino M, Van Meir EG, Osuka S, Shofuda T, Klekner A, Zollo M, Leonard JR, Rubin JB, Jabado N, Albrecht S, Mora J, Van Meter TE, Jung S, Moore AS, Hallahan AR, Chan JA, Tirapelli DPC, Carlotti CG, Fouladi M, Pimentel J, Faria CC, Saad, AG, Massimi L, Liau LM, Wheeler H, Nakamura H, Elbabaa SK, Perezpeña-Diazconti M, Ponce de León FC, Robinson S, Zapotocky M, Lassaletta A, Huang A, Hawkins CE, Tabori U, Bouffet E, Bartels U, Dirks P, Rutka JT, Bader GD, Reimand J, Goldenberg A, Ramaswamy V, Taylor MD **(2017). Intertumoral heterogeneity within medulloblastoma subgroups, Cancer Cell 31(6): 737-754. *Shared first co-authorship.**

Morrissy AS*, **Cavalli FMG***, Remke M*, Ramaswamy V, Shih DJH, Holgado BL, Farooq H, Donovan LK, Garzia L, Agnihotri S, Kiehna EN, Mercier E, Mayoh C, Papillon-Cavanagh S, Nikbakht H, Gayden T, Torchia J, Picard D, Merino DM, Vladoiu M, Luu B, Wu X, Daniels C, Horswell S, Thompson YY, Hovestadt V, Northcott PA, Jones DTW, Peacock J, Wang X, Mack SC, Reimand J, Albrecht S, Fontebasso AM, Thiessen N, Li Y, Schein JE, Lee D, Carlsen R, Mayo M, Tse K, Tam A, Dhalla N, Ally A, Chuah E, Cheng Y, Plettner P, Li HI, Corbett RD, Wong T, Long W, Loukides J, Buczkowicz P, Hawkins CE, Tabori U, Rood BR, Myseros JS, Packer RJ, Korshunov A, Lichter P, Kool M, Pfister SM, Schüller U, Dirks P, Huang A, Bouffet Eric, Rutka JT, Bader GD, Swanton C, Ma Y, Moore RA, Mungall AJ, Majewski J, Jones SJM, Das S, Malkin D, Jabado N, Marra MA, Taylor MD **(2017). Spatial heterogeneity in medulloblastoma, Nature Genetics 49(5): 780-788. *Shared first co-authorship.**

Oral Presentation

DSCB Trainee seminar, Toronto, ON, Canada, September 2016.
Intertumoral heterogeneity within medulloblastoma subgroups

Poster presentations

Forum de la Recherche en Cancérologie Auvergne-Rhône-Alpes, Lyon, France, April 2017
Integrative analysis reveals novel subtypes of medulloblastoma subgroups

GFCC Cancer Research Day, Toronto, ON, Canada, January 2017.
Integrative analysis reveals novel subtypes of medulloblastoma subgroups

Best Poster Presentation –Research Fellow category

Beyond the Genome: Cancer genomics, Boston, MA, USA, October 2014.
Relative Spatial Homogeneity in embryonic brain tumors showed by multi layer genomic analysis.

nature genetics

Spatial heterogeneity in medulloblastoma

A Sorana Morrissy[1,2,37], Florence M G Cavalli[1,2,37], Marc Remke[1–5,37], Vijay Ramaswamy[1,2,6], David J H Shih[1,2,7], Borja L Holgado[1,2], Hamza Farooq[1,2,7], Laura K Donovan[1,2], Livia Garzia[1,2,8], Sameer Agnihotri[9], Erin N Kiehna[10], Eloi Mercier[11], Chelsea Mayoh[11], Simon Papillon-Cavanagh[12], Hamid Nikbakht[12], Tenzin Gayden[12], Jonathon Torchia[2,6,7], Daniel Picard[3–5], Diana M Merino[2,6,13], Maria Vladoiu[1,2], Betty Luu[1,2], Xiaochong Wu[1,2], Craig Daniels[1,2], Stuart Horswell[14], Yuan Yao Thompson[1,2,7], Volker Hovestadt[15], Paul A Northcott[16], David T W Jones[16], John Peacock[1,2,7], Xin Wang[1,2,7], Stephen C Mack[1,2,7], Jüri Reimand[17–19], Steffen Albrecht[20], Adam M Fontebasso[21], Nina Thiessen[11], Yisu Li[11], Jacqueline E Schein[11], Darlene Lee[11], Rebecca Carlsen[11], Michael Mayo[11], Kane Tse[11], Angela Tam[11], Noreen Dhalla[11], Adrian Ally[11], Eric Chuah[11], Young Cheng[11], Patrick Plettner[11], Haiyan I Li[11], Richard D Corbett[11], Tina Wong[11], William Long[11], James Loukides[2], Pawel Buczkowicz[22], Cynthia E Hawkins[2,22], Uri Tabori[2,6], Brian R Rood[23], John S Myseros[24], Roger J Packer[25], Andrey Korshunov[26], Peter Lichter[15,27], Marcel Kool[16], Stefan M Pfister[16,27,28], Ulrich Schüller[29–31], Peter Dirks[2,10], Annie Huang[2,6], Eric Bouffet[2,6], James T Rutka[2,7,10], Gary D Bader[19], Charles Swanton[32,33], Yusanne Ma[11], Richard A Moore[11], Andrew J Mungall[11], Jacek Majewski[21], Steven J M Jones[11,34,35], Sunit Das[1,2,36], David Malkin[6], Nada Jabado[21], Marco A Marra[11,34] & Michael D Taylor[1,2,7]

Spatial heterogeneity of transcriptional and genetic markers between physically isolated biopsies of a single tumor poses major barriers to the identification of biomarkers and the development of targeted therapies that will be effective against the entire tumor. We analyzed the spatial heterogeneity of multiregional biopsies from 35 patients, using a combination of transcriptomic and genomic profiles. Medulloblastomas (MBs), but not high-grade gliomas (HGGs), demonstrated spatially homogeneous transcriptomes, which allowed for accurate subgrouping of tumors from a single biopsy. Conversely, somatic mutations that affect genes suitable for targeted therapeutics demonstrated high levels of spatial heterogeneity in MB, malignant glioma, and renal cell carcinoma (RCC). Actionable targets found in a single MB biopsy were seldom clonal across the entire tumor, which brings the efficacy of monotherapies against a single target into question. Clinical trials of targeted therapies for MB should first ensure the spatially ubiquitous nature of the target mutation.

Many cancer types show considerable intertumoral heterogeneity between individuals[1–3]. Molecular biomarkers are intended to (i) tailor treatment intensities[4,5], (ii) define oncogenic drivers for targeted therapies[5–7], and (iii) identify diagnostic mutations (e.g., *SMARCB1* mutations in atypical teratoid/rhabdoid tumors)[8]. Currently, clinical diagnoses are based on single biopsies, with the assumption of spatial homogeneity across tumors; however, spatial heterogeneity could lead to erroneous tumor classification or the selection of therapies against targets that are present only in a locally restricted portion of the tumor. These implications were recently highlighted in late-stage RCC[9,10], with highly divergent mutational profiles affecting *MTOR* and *TP53*, as well as demonstrating good and poor prognostic gene signatures in multiregion biopsies from the same tumor[10,11].

To determine the degree and clinical importance of spatial heterogeneity in MB, we performed multiregional biopsies and compared gene expression profiles, DNA copy-number alterations (CNAs), and somatic mutations. Our cohort included 9 primary MBs, 16 HGGs (10 with gene expression only[12]), and 10 RCCs[10], with 4–11 spatially distinct biopsies from each (median: 6). An overview of the data types available for each patient is presented in **Supplementary Table 1a** and **Supplementary Figure 1**.

Glioblastoma[13] and MB[14] each comprise four distinct molecular subgroups that are discerned through analysis of transcriptional data. Unsupervised hierarchical clustering (HCL) of expression data has shown that MB biopsies form tight clusters apart from single samples[15–20] (8/8; **Fig. 1a**, **Supplementary Fig. 2a**,**b**), whereas in HGGs (3/3) and RCCs (8/9), multiregion biopsies from single individuals clustered apart when combined with single samples (**Supplementary Fig. 2c**–**f**). Overall, on the basis of the s.d. of expression, intertumoral differences were greater than intratumoral heterogeneity in each tumor type (**Fig. 1b**). Subtype prediction with Predictive Analysis of Microarrays (PAM) showed that 21% (13/63) of glioblastoma multiregion samples diverged from the most commonly observed subtype for each patient, compared with only 2% (1/52) of MB biopsies (P = 0.003; **Fig. 1c**–**e**, **Supplementary Figs. 3**–**6**). When we considered only

A full list of affiliations appears at the end of the paper.

Received 3 November 2014; accepted 17 March 2017; published online 10 April 2017; doi:10.1038/ng.3838

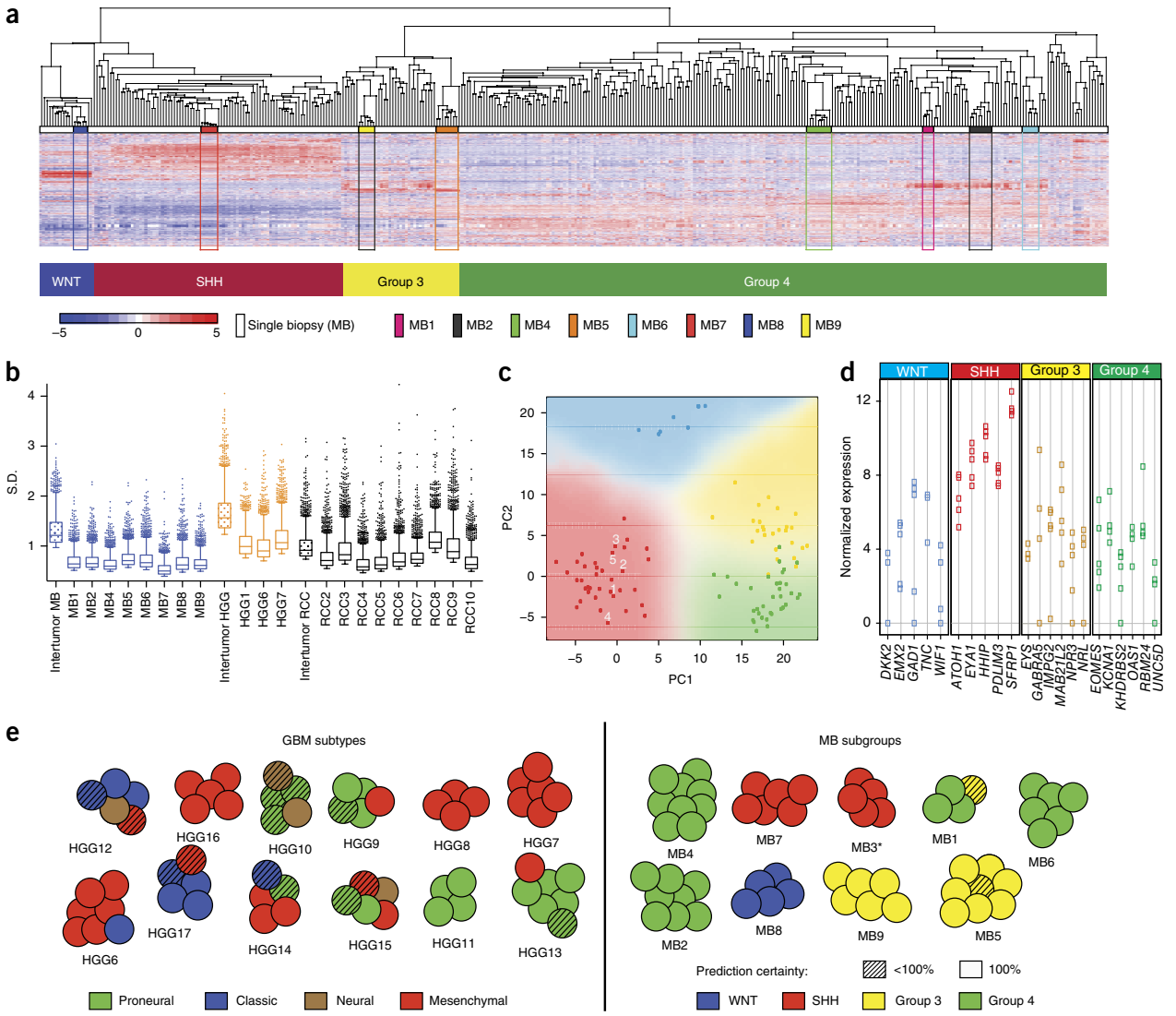

Figure 1 Medulloblastomas, but not glioblastomas, show reliable transcriptome-based subgroup prediction. (**a**) Unsupervised HCL using 1,000 high-s.d. transcripts of eight multiregion MB samples combined with single biopsies ($n = 334$) demonstrates tight clustering of matched multiregion MB samples across subgroups. (**b**) The top 2,000 s.d.-transcript values determined on intra- and intertumor levels in MB, HGG, and RCC samples. Center lines indicate data medians; box limits indicate the 25th and 75th percentiles; whiskers extend 1.5 times the interquartile range from the 25th and 75th percentiles; outliers are represented by individual points. Intertumoral and intratumoral values are indicated by patterned and white boxes, respectively. (**c**) Principal component analysis (PCA) of 22 MB subgroup marker genes confirmed a low degree of transcriptional intratumoral heterogeneity, exemplified in MB3. Multiregion biopsy numbers of MB3 are indicated in the red-shaded region of the plot. PCA was conducted with 103 single-biopsy samples analyzed by NanoString. (**d**) Dot plot illustrating highly similar marker-gene expression in all multiregion biopsies for MB3. (**e**) Glioblastoma (GBM) subtype and MB subgroup predictions based on PAM results. The SHH subgroup affiliation of MB3 (marked with an asterisk) was inferred from NanoString results. Hashed circles indicate biopsies with <100% prediction certainty.

biopsies with subgroup predictions of 100% confidence, we found that all MB tumors had concordant subgroup calls between multiple biopsies (9/9), compared with only 55% of glioblastomas (6/11; $P = 0.038$; **Fig. 1e**). We conclude that MB can be robustly and reliably subgrouped from only a single biopsy, but glioblastoma cannot.

We identified somatic CNAs by using a custom pipeline based on the TITAN algorithm[21], which is robust to high levels of normal contamination (Online Methods). Regions of CNA were identified in all three tumor types (**Fig. 2a**, **Supplementary Figs. 7** and **8**, **Supplementary Table 1b**,**c**), and unsupervised HCL of clonal segments showed tight clustering of individual biopsies in the cohort across all tumor entities (**Fig. 2b**, **Supplementary Fig. 9**). CNA-derived measurements of spatial heterogeneity highlighted the variance between individuals for each tumor type (**Fig. 2c**). Somatic single-nucleotide variants (SNVs) and insertions/deletions (indels) recapitulated a similar pattern of spatial heterogeneity across tumors (**Fig. 2d**, **Supplementary Table 1d**). Overall, on the basis of the mutation and CNA data, none of the three tumor types comprised only homogeneous or heterogeneous tumors; rather, each had a repertoire of tumors residing along a continuum of genetic heterogeneity.

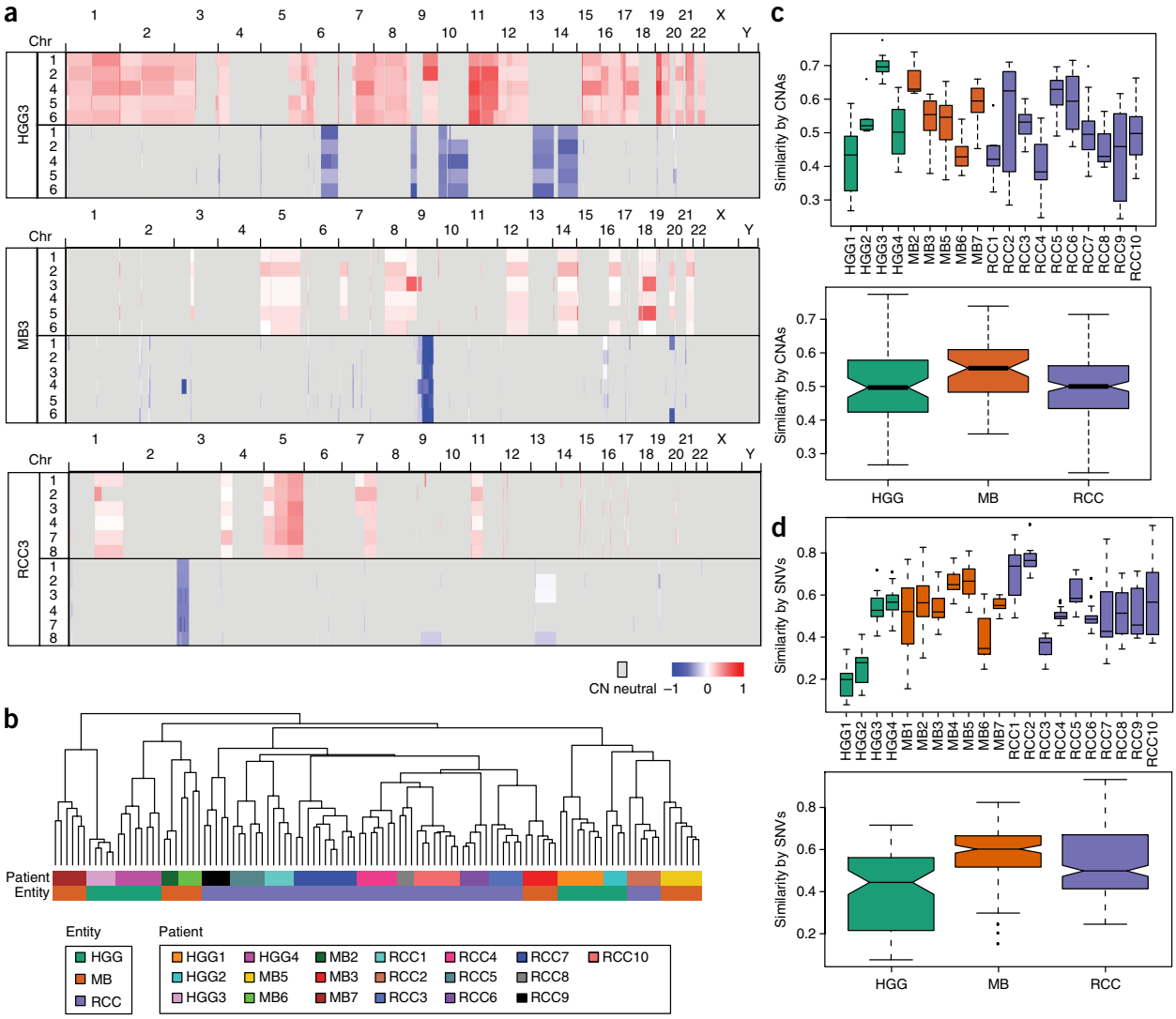

Figure 2 The variable intratumoral heterogeneity of somatic alterations in all tumor entities. Genome-wide analysis of CNAs did not recapitulate the striking expression-based spatial homogeneity of MBs. (**a**) Copy-number (CN) segments of gain (red) and loss (blue) across the genomes of three individual patients for each biopsy. (**b**) Unsupervised HCL of copy-number segments shows tight clustering of individual biopsies across all tumors in the cohort. (**c**,**d**) The intratumoral heterogeneity measured from CNAs (**c**; $n = 19$) or SNVs (**d**; $n = 21$), both in individual patients (top) and summarized by entity (bottom), shows that tumors in all entities range from high (e.g., HGG3 and MB2) to low (e.g., HGG1 and RCC3) spatial similarity. Similarity was measured as the binary distance between all pairs of tumor-matched biopsies. Box plot center lines indicate data medians; box limits indicate the 25th and 75th percentiles; whiskers extend 1.5 times the interquartile range from the 25th and 75th percentiles; outliers are represented by individual points. Notches in box plots (the lower plots in **c**,**d**) indicate where the 95th percentile of the data falls.

This genomic complexity results from a process of clonal evolution whereby the successive acquisition of mutations and CNAs generates genetically related subpopulations of cells or lineages within each tumor. We integrated CNA and mutational data using the EXPANDS algorithm[22], to infer the cellular lineage composition in each biopsy. EXPANDS detects multiple genetically distinct coexisting subpopulations of cells and allows phylogenetic reconstruction of their evolutionary relationships. **Figure 3a**, which describes the spatial distribution of genetically distinct subpopulations throughout a tumor, illustrates the clonal intermixing detected in many samples of the cohort (**Fig. 3b–d**, **Supplementary Fig. 10**, **Supplementary Table 1e**,**f**). Many tumor biopsies had a major clone (i.e., a genotype present in >70% of tumor cells) that was also detected in a minority of cells in other biopsies from the same tumor (i.e., subclonal) or that was absent in other biopsies (for example, biopsies 3, 5, and 6 from tumor RCC7 were genetically similar to some cells in biopsy 4 (4a), but not all cells (4b clustered separately); **Fig. 3c**). In some tumors, individual biopsies contained two or more cell lineages that independently accumulated distinct repertoires of mutations not found elsewhere in the tumor (e.g., HGG2 biopsies 1 and 5; **Fig. 3c**). The presence of multiple genetically distinct cellular lineages within single biopsies has previously been linked to poor prognosis and treatment response across a variety of cancer types[23].

This surprising but common pattern of major genetic clones in one biopsy that are subclonal or absent in spatially distinct locations in the same tumor prompted us to investigate observable mutation clonality

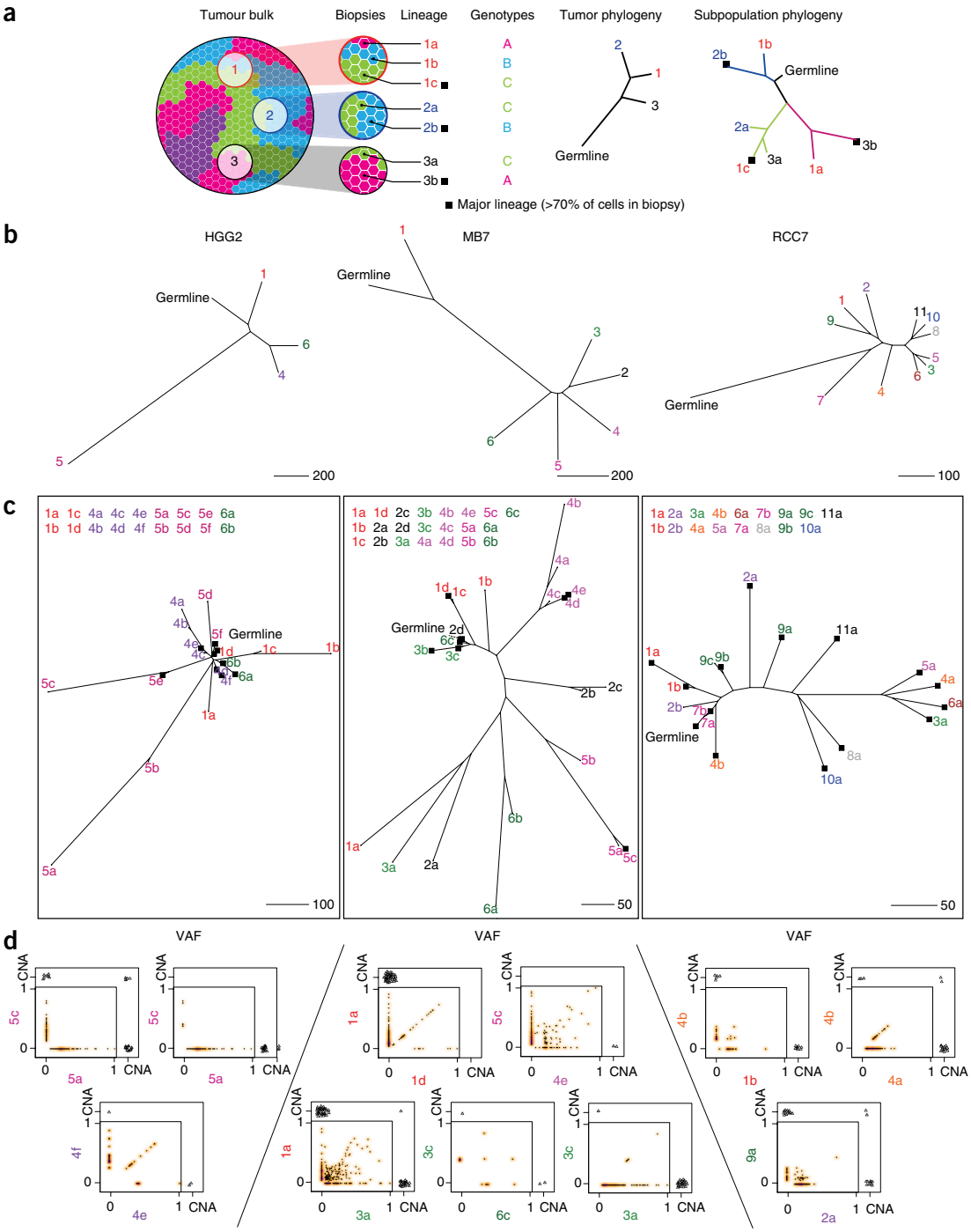

Figure 3 Spatial intermixing of clonal lineages. (**a**) Example illustration of a tumor with four clonal lineages that are spatially dispersed (color-coded in blue, green, pink, and purple), demonstrating how data from three biopsies can be used to build a typical biopsy-level phylogenetic tree as well as a subpopulation-level tree that reflects intermixing of the three detected genetic lineages. Branch tips are color-coded according to biopsy number, and labeled according to biopsy number (1, 2, 3) and clonal lineage (a, b, c). Branch colors correspond to the cellular genotype; black squares indicate major cellular lineages (>70% of tumor cells in the biopsy, scaled by the largest detectable population). Note that the number of biopsies may not be sufficient to 'discover' all distinct clonal lineages (e.g., purple clone). (**b**) Biopsy-level trees of three representative tumors: HGG2, MB7, and RCC7. (**c**) Subpopulation-level trees showing that some cellular lineages have high similarity to lineages in other biopsies, thus suggesting spatial intermixing (e.g., MB7 biopsies 1, 2, and 3; RCC7 biopsy 4). Conversely, some biopsies harbored more than one distinct lineage (e.g., HGG2 biopsy 5). (**d**) Variant allele frequencies (VAFs) of mutations are shown along with CNAs exclusive to or shared by pairs of biopsies or subpopulations. VAF scatter plots have a smoothed color density; black dots represent individual mutations. CNA events (triangles) are shown (with some jitter) if they were present in either compartment, or shared.

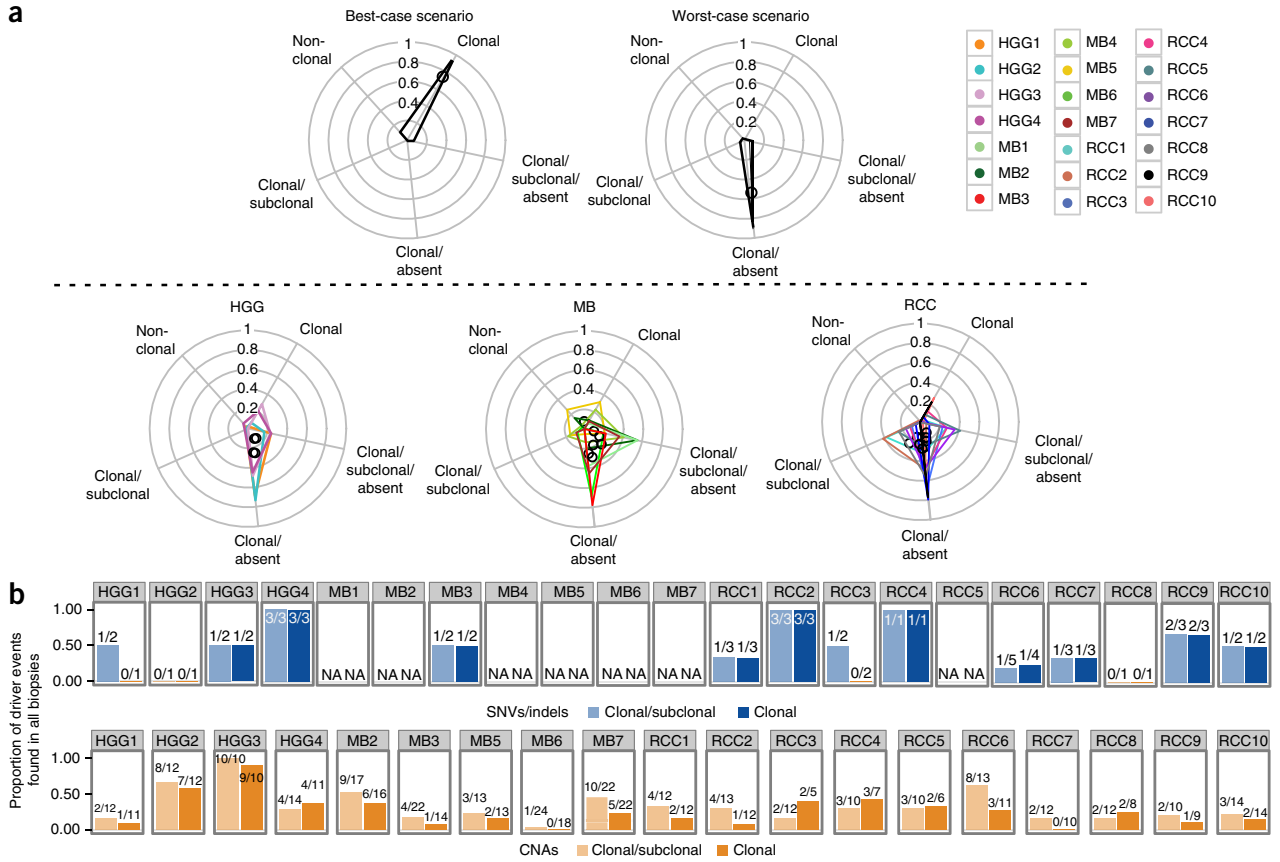

Figure 4 Genetically distinct clonal lineages yield ON/OFF mutation patterns between spatially separated biopsies. (**a**) Nonsynonymous mutations binned into five categories: clonal in all biopsies (clonal); clonal in some biopsies and subclonal in others (clonal/subclonal); clonal in some biopsies and completely absent in others (clonal/absent); clonal in some biopsies, and subclonal or absent in others (clonal/subclonal/absent); and never detected as clonal (non-clonal). Top, illustration of the most favorable clinical scenario, in which most mutations are clonal across all biopsies (left), and the worst-case scenario, in which mutations are clonal in some biopsies but absent in others (right). Bottom, mutation patterns follow a worst-case scenario across tumor types. Tumor-specific polygons on radial plots indicate the proportion of mutations on each of the five axes, with polygon centers marked by black circles. (**b**) The proportion of driver mutations/indels (top) or CNAs (bottom) that are found in every biopsy of a given tumor (i.e., trunk events) when both clonal and subclonal or only clonal driver events are considered. The absolute numbers are shown above the bars.

across biopsies, as clonality is a key requirement of clinically actionable therapeutic targets[24]. We classified mutations into clonal and subclonal populations (**Supplementary Fig. 11**, **Supplementary Table 1g**) and determined whether the status of the subset of damaging clonal mutations changed between spatially separated tumor biopsies. In nearly all tumors we found a predominance of clonal mutations that were subclonal or completely absent in additional biopsies (**Fig. 4a**, **Supplementary Fig. 12**; validation set of seven mutations with a 96% validation rate across biopsies; **Supplementary Fig. 13**, **Supplementary Table 1h**). This observation held when we considered only driver events[25–28] (**Fig. 4b**, **Supplementary Table 1i–k**). We predict that monotherapies against a single target identified in a single biopsy are unlikely to show dramatic clinical effects, as targets are not ubiquitous; this would leave untargeted clones in unsampled portions of the tumor free to survive and repopulate the tumor.

When the goal of a cancer therapy is improved patient treatment, the clinically relevant question is whether the observed level of genomic spatial heterogeneity affects actionable or driver alterations. As proof of concept, we focused on a set of genes with known roles in cancer initiation and/or progression[29], or with defined drug interactions[30]. These genes are enriched in relevant or actionable targets in a manner that is unbiased toward either of the cancer types we included (**Supplementary Table 1l,m**). When we investigated the spectrum of SNVs, indels, and CNAs affecting these genes (**Supplementary Figs. 14** and **15**), we found a remarkable variety of patterns across tumors, including cases with only a small set of shared alterations across biopsies but with many events present in single biopsies (e.g., *MET* amplification in HGG4); homogeneous tumors with many shared actionable events (e.g., HGG3); cases without ubiquitous actionable targets, which may require multiagent targeted therapeutics (e.g., MB6); tumors that lacked vulnerability to any of the considered actionable targets in a subset of biopsies (e.g., MB7); and tumors with alterations that may predict resistance (e.g., *TP53* compound loss and somatic mutation in RCC7).

Considering the full set of identified actionable mutations per tumor across all biopsies, we calculate that in each tumor entity, an average of at least five biopsies is required to provide an 80% chance of identifying at least 80% of these alterations. If these measures were reduced to 50%, sampling of at least two biopsies would be required, or as many as four for highly heterogeneous tumors (**Fig. 5a**). This is probably an underestimation, as the detection of actionable mutations does not plateau in most patients (**Supplementary Fig. 16**).

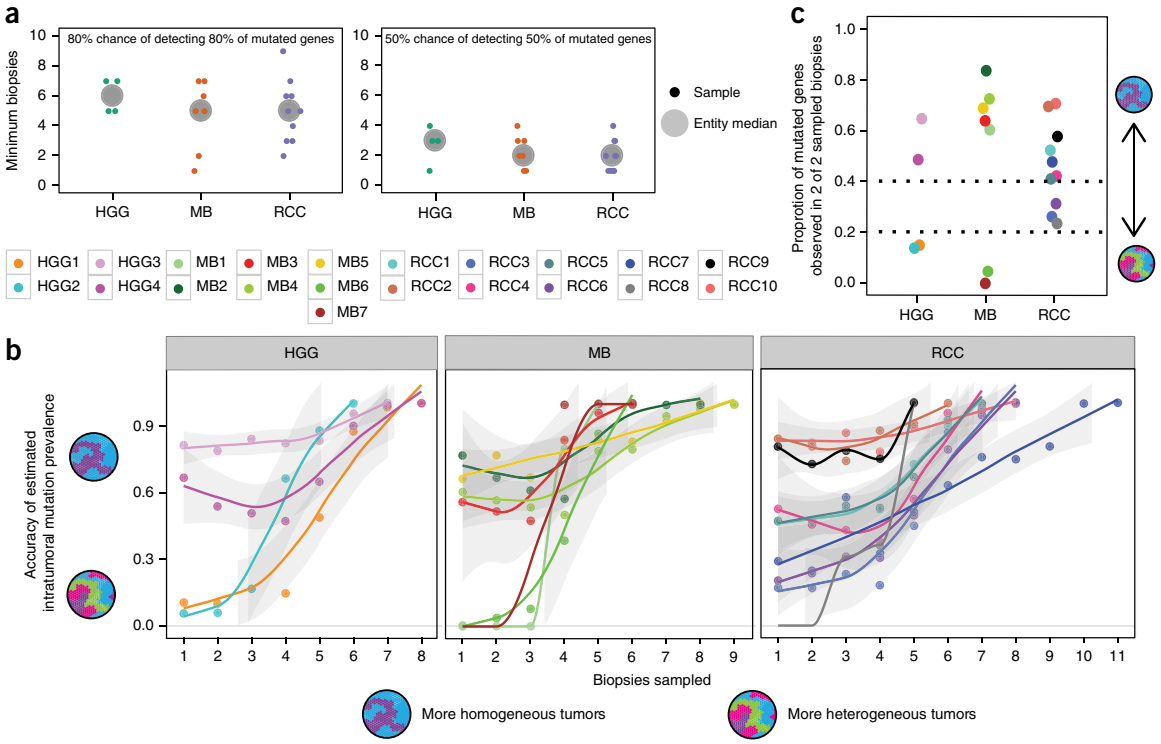

Figure 5 Quantification of variable genetic heterogeneity across tumor entities. (**a**) Our analysis of all mutated genes (from the list of actionable targets) identified in each tumor across all biopsies suggests that an average of five biopsies of an individual tumor is required to provide an 80% likelihood of recovering 80% of the known mutated genes (left). At least two biopsies are required to achieve a 50% likelihood of recovering 50% of mutated genes (right). (**b**) The likelihood of correctly inferring the frequency of a mutation in a whole tumor depends on the number of biopsies sampled, and whether the tumor is more or less genetically homogeneous. The accuracy of frequency prediction for brain tumors shows a bimodal pattern, with low-genetic-variance tumors having higher accuracy (>0.6) even with few biopsies, whereas at least five biopsies are required to achieve the same confidence in high-genetic-variance tumors (HGG and MB). RCCs additionally show an intermediate pattern. Accuracy was measured as the proportion of times that a gene's observed frequency in a selection of biopsies was within 10% of the known frequency across all biopsies. Lines represent a Loess fit to the points per tumor; gray shading indicates the 95% confidence interval. (**c**) Given a random selection of two biopsies, we ranked patients on the basis of the proportion of mutated genes (from the actionable target list) present in both biopsies. Patients with genetically heterogeneous tumors had median values < 0.2. Points represent the median value of all possible biopsy pairs per patient, and are color-coded according to the key in **a**.

Up-front profiling of numerous tumor regions to identify the full repertoire of actionable targets is neither practical nor likely, given the amount of sequencing required; thus we focused on maximizing the information derived from a minimal set of biopsies. Specifically, we wanted to determine how well we could predict the frequency of individual mutations across a tumor with an increasing number of biopsies, noting that prediction accuracy for mutations identified in a single fraction would be high only in very homogeneous tumors. We empirically determined the frequency of each alteration, considering all possible pairs of an increasing number of biopsies, and compared this observed quantity to the known frequency of the alteration in all biopsies; the difference between these values was the inference error of mutation frequency resulting from an insufficient number of biopsies from genetically heterogeneous tumors (**Supplementary Fig. 17**). Using a 10% error rate as an acceptable threshold, we calculated for each tumor the number of observed mutation frequencies that fell within this range (i.e., accuracy). As expected, we found that accuracy improved with increasing numbers of biopsies, and also that brain tumors fall into two patterns. The first comprises more homogeneous tumors, which have fairly high prediction accuracy even with a low number of biopsies, and the second comprises more heterogeneous tumors for which multiple biopsies are required to ensure an accurate determination of mutation frequency (**Fig. 5b**). In our cohort of MBs and glioblastomas, considering just two biopsies per tumor enabled the distinction of tumors with high versus low genetic heterogeneity, with high specificity especially for highly heterogeneous tumors (**Fig. 5c**, **Supplementary Fig. 18**).

Although spatial heterogeneity is clearly a barrier to highly effective therapeutics against an entire primary tumor, the extent of heterogeneity between primary and recurrent MB[31] is many fold greater (**Fig. 6a**, **Supplementary Fig. 19**). This vast discordance at relapse is therefore unlikely to be secondary solely to inadequate spatial sampling of the therapeutically naive primary tumor. In gliomas[32], the recurrent disease resembles the primary tumor more closely, and only in rare cases diverges to the extent seen in MB, possibly as a result of less complete success in the resection of this more diffuse and infiltrating tumor. MB is known to recur from very rare populations of cells[31]; thus, therapeutic approaches that can eradicate such cellular lineages despite their low prevalence in the primary tumor are severely needed.

Targeted cancer immunotherapy is based on the presence of tumor-specific cell-surface antigens, as opposed to cell-autonomous somatic mutations. We examined the expression of the antigens/genes for which chimeric antigen receptor T cells or monoclonal antibodies

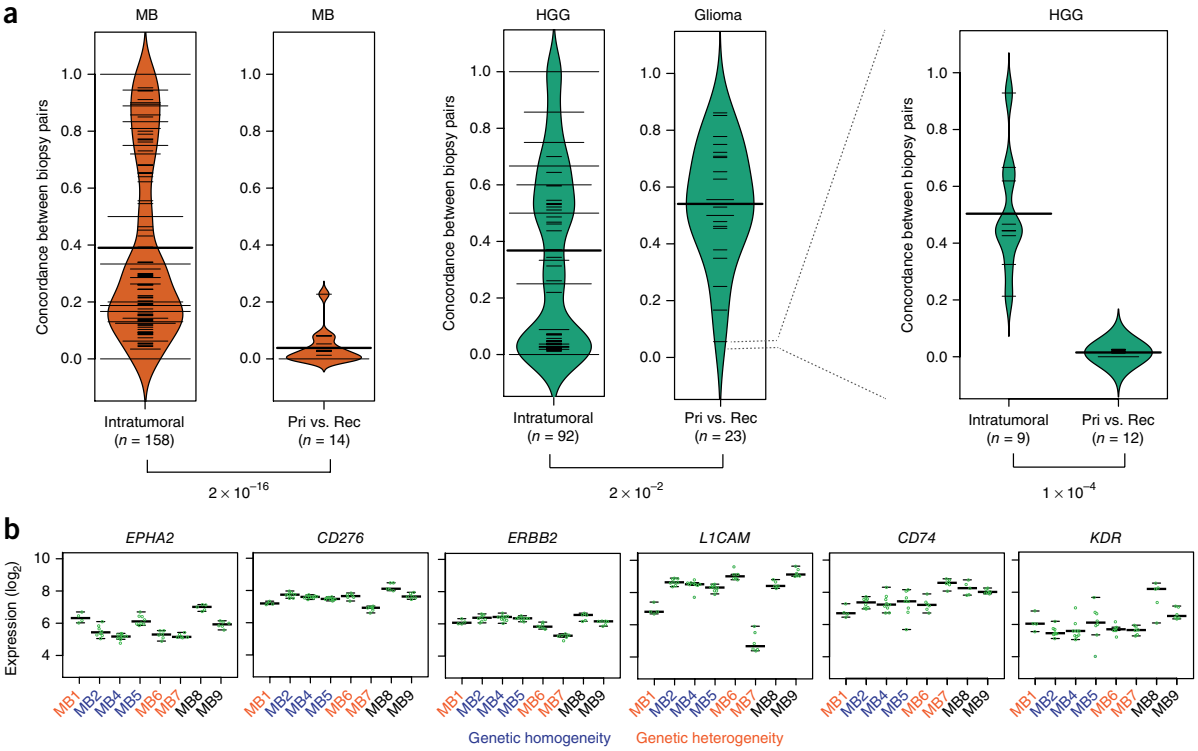

Figure 6 Genetic heterogeneity at recurrence greatly exceeds spatial heterogeneity in MB. (**a**) The genetic concordance of pre- versus post-therapy biopsies (data from ref. 31) was an order of magnitude lower than the up-front genetic spatial heterogeneity in MB samples ($P < 10^{-16}$, Welch two-sample *t*-test; $n = 14$ primary (Pri)–recurrence (Rec) pairs; $n = 158$ spatial comparisons from seven tumors). HGGs in our cohort showed a similar overall distribution of spatial heterogeneity ($n = 92$ comparisons from four tumors), and were not dramatically different compared with the low concordance of low-grade gliomas (LGGs) to HGGs post-therapy[41] ($n = 23$ glioma primary–recurrence pairs; data from ref. 32). One LGG relapse to HGG exhibited post-therapeutic genetic concordance values on par with those for MBs ($P < 10^{-4}$, Welch two-sample *t*-test; $n = 12$ primary–recurrence comparisons from patient 17 of ref. 32; $n = 9$ spatial comparisons). Concordance was measured as the proportion of clonal somatic mutations in common between a pair of biopsies, given the total number of clonal somatic mutations in the two samples. The width of the bean plots scales with the number of measurements with a similar *y*-value, showing data distribution. Thin horizontal lines indicate individual observations; multiple observations with the same value were added together to form wider lines. Thick horizontal bars indicate averages. (**b**) Low expression variance was observed across multiregion biopsies of cell-surface molecules with immunotherapies currently in clinical trials. This indicates that tumors with high genetic spatial heterogeneity may respond well to chimeric antigen receptor T cell or antibody-based therapy. Green points mark the expression of target genes in individual biopsies; horizontal lines indicate the median expression and the 25th and 75th percentiles of expression per tumor.

already exist[33–43], and we observed remarkable consistency of expression across multiregional biopsies, which contrasts sharply with the heterogeneity of somatic mutations across fractions in the same set of tumors. This was the case in all MBs examined, including those with high levels of genetic heterogeneity and for which targeted therapy would be problematic[33–43] (**Fig. 6b**, **Supplementary Fig. 20**). The homogeneity of the transcriptome versus the heterogeneity of somatic mutations in our MB cohort suggests that targeted immunotherapeutic approaches could potentially overcome the hurdle of spatial genetic heterogeneity.

The vast majority of patients with brain tumors have their tumor classified from a single tumor biopsy, which is potentially adequate for MB, but not for glioblastoma. The extent of the spatial heterogeneity of somatic mutations observed in our cohort suggests that clinical trials of molecularly targeted therapy should first assess the ubiquitous distribution of the target. The lack of clonal actionable driver mutations that are ubiquitously present across all regions of a given brain tumor suggests that monotherapies that target a single gene from a single biopsy are unlikely to have dramatic effects in terms of improving the lives of patients with brain tumors.

URLs. Gene Expression Omnibus, https://www.ncbi.nlm.nih.gov/geo/; European Genome-phenome Archive, https://www.ebi.ac.uk/ega/.

METHODS

Methods, including statements of data availability and any associated accession codes and references, are available in the online version of the paper.

Note: Any Supplementary Information and Source Data files are available in the online version of the paper.

ACKNOWLEDGMENTS

The MAGIC project (M.D.T. and M.A.M.) is financially supported by Genome Canada, Genome BC, Terry Fox Research Institute, Ontario Institute for Cancer Research, Pediatric Oncology Group Ontario, funds from The Family of Kathleen Lorette and the Clark H. Smith Brain Tumour Centre, Montreal Children's Hospital Foundation, Hospital for Sick Children: Sonia and Arthur Labatt Brain Tumour Research Centre, Chief of Research Fund, Cancer Genetics Program, Garron Family Cancer Centre, B.R.A.I.N. Child, M.D.T.'s Garron Family Endowment, and the BC Childhood Cancer Parents Association. M.D.T. is supported by a Stand Up To Cancer St. Baldrick's Pediatric Dream Team Translational Research Grant (SU2C-AACR-DT1113); Stand Up To Cancer is a program of the Entertainment Industry Foundation administered by the American Association for Cancer

Research. M.D.T. is also supported by The Garron Family Chair in Childhood Cancer Research, and grants from the Cure Search Foundation, the US National Institutes of Health (R01CA148699 and R01CA159859), The Pediatric Brain Tumor Foundation, The Terry Fox Research Institute, and Brainchild. This study was conducted with the support of the Ontario Institute for Cancer Research through funding provided by the Government of Ontario, as well as The Brain Tumour Foundation of Canada Impact Grant of the Canadian Cancer Society and Brain Canada with the financial assistance of Health Canada (grant 703202 to M.D.T.). This work was also supported by a Program Project Grant from the Terry Fox Research Institute (to M.D.T.), a Grand Challenge Award from CureSearch for Children's Cancer (to M.D.T.), and the PedBrain Tumor Project contributing to the International Cancer Genome Consortium, funded by German Cancer Aid (109252) and by the German Federal Ministry of Education and Research (BMBF; grants 01KU1201A and MedSys 0315416C to S.M.P. and P.L.). We acknowledge the Labatt Brain Tumour Research Centre Tumour and Tissue Repository, which is supported by B.R.A.I.N. Child and Megan's Walk (M.D.T.). M.A.M. acknowledges support from the Canadian Institutes of Health Research (CIHR; FDN-143288). M.R. is supported by a fellowship from the Dr. Mildred Scheel Foundation for Cancer Research/German Cancer Aid. F.M.G.C. is supported by the Stephen Buttrum Brain Tumour Research Fellowship, granted by the Brain Tumour Foundation of Canada. V.R. is supported by a CIHR fellowship and an Alberta Innovates–Health Solutions Clinical Fellowship. For technical support and expertise in next-generation sequencing efforts, we thank The Centre for Applied Genomics (Toronto, Ontario, Canada). We thank S. Archer for technical writing, and C. Smith for artwork.

AUTHOR CONTRIBUTIONS

A.S.M., F.M.G.C., M.R., M.D.T., and M.A.M. led the study and wrote the manuscript. A.S.M. and F.M.G.C. designed, supervised, and performed bioinformatic analyses. M.R. led the collection of samples and data generation, and performed bioinformatic analyses. B.L. extracted nucleic acids, managed biobanking, and maintained the patient database. S.H., A.M.F., B.L.H., C.D., D.J.H.S., D.M.M., D.P., D.T.W.J., E.N.K., H.F., J.M., J.P., J.R., J.T., L.G., L.K.D., M.V., P.A.N., S. Agnihotri, S. Albrecht, S.C.M., S.P.-C., V.H., V.R., X. Wu, X. Wang, and Y.Y.T. provided technical and bioinformatic support. A.A., A.T., C.M., D.L., E.C., E.M., H.I.L., J.E.S., K.T., M.M., N.D., P.P., R.C., R.D.C., T.W., W.L., Y.C., and Y.L. led and performed RNA-seq and whole-genome sequencing library preparation and sequencing experiments, and performed data analyses. N.T. and Y.M. supervised bioinformatic analyses at the Genome Sciences Center. H.N. and T.G. performed whole-exome sequencing library preparation and sequencing experiments, and performed data analyses. B.R.R., C.S., C.E.H., J.L., J.S.M., N.J., P.B., R.J.P., S.D., and U.S. provided the patient samples and clinical details that made the study possible. A.H., A.J.M., A.K., D.M., E.B., G.D.B., J.T.R., M.K., P.D., P.L., R.A.M., S.J.M.J., S.M.P., and U.T. provided valuable input regarding study design, data analysis, and interpretation of results. M.D.T. and M.A.M. provided financial and technical infrastructure and oversaw the study, and served as joint senior authors and project co-leaders.

COMPETING FINANCIAL INTERESTS

The authors declare no competing financial interests.

1. Northcott, P.A. *et al.* Medulloblastoma comprises four distinct molecular variants. *J. Clin. Oncol.* **29**, 1408–1414 (2011).
2. Kleinman, C.L. *et al.* Fusion of TTYH1 with the C19MC microRNA cluster drives expression of a brain-specific DNMT3B isoform in the embryonal brain tumor ETMR. *Nat. Genet.* **46**, 39–44 (2014).
3. Versteege, I. *et al.* Truncating mutations of hSNF5/INI1 in aggressive paediatric cancer. *Nature* **394**, 203–206 (1998).
4. Pietsch, T. *et al.* Prognostic significance of clinical, histopathological, and molecular characteristics of medulloblastomas in the prospective HIT2000 multicenter clinical trial cohort. *Acta Neuropathol.* **128**, 137–149 (2014).
5. Remke, M., Ramaswamy, V. & Taylor, M.D. Medulloblastoma molecular dissection: the way toward targeted therapy. *Curr. Opin. Oncol.* **25**, 674–681 (2013).
6. Kool, M. *et al.* Genome sequencing of SHH medulloblastoma predicts genotype-related response to smoothened inhibition. *Cancer Cell* **25**, 393–405 (2014).
7. Kieran, M.W. Targeted treatment for sonic hedgehog-dependent medulloblastoma. *Neuro-oncol.* **16**, 1037–1047 (2014).
8. Louis, D.N. *et al.* The 2007 WHO classification of tumours of the central nervous system. *Acta Neuropathol.* **114**, 97–109 (2007).
9. Gerlinger, M. *et al.* Genomic architecture and evolution of clear cell renal cell carcinomas defined by multiregion sequencing. *Nat. Genet.* **46**, 225–233 (2014).
10. Gerlinger, M. *et al.* Intratumor heterogeneity and branched evolution revealed by multiregion sequencing. *N. Engl. J. Med.* **366**, 883–892 (2012).
11. Gulati, S. *et al.* Systematic evaluation of the prognostic impact and intratumour heterogeneity of clear cell renal cell carcinoma biomarkers. *Eur. Urol.* **66**, 936–948 (2014).
12. Sottoriva, A. *et al.* Intratumor heterogeneity in human glioblastoma reflects cancer evolutionary dynamics. *Proc. Natl. Acad. Sci. USA* **110**, 4009–4014 (2013).
13. Verhaak, R.G. *et al.* Integrated genomic analysis identifies clinically relevant subtypes of glioblastoma characterized by abnormalities in PDGFRA, IDH1, EGFR, and NF1. *Cancer Cell* **17**, 98–110 (2010).
14. Taylor, M.D. *et al.* Molecular subgroups of medulloblastoma: the current consensus. *Acta Neuropathol.* **123**, 465–472 (2012).
15. Northcott, P.A. *et al.* Enhancer hijacking activates GFI1 family oncogenes in medulloblastoma. *Nature* **511**, 428–434 (2014).
16. Northcott, P.A. *et al.* Subgroup-specific structural variation across 1,000 medulloblastoma genomes. *Nature* **488**, 49–56 (2012).
17. Vanner, R.J. *et al.* Quiescent sox2^{+} cells drive hierarchical growth and relapse in sonic hedgehog subgroup medulloblastoma. *Cancer Cell* **26**, 33–47 (2014).
18. Beuselinck, B. *et al.* Molecular subtypes of clear cell renal cell carcinoma are associated with sunitinib response in the metastatic setting. *Clin. Cancer Res.* **21**, 1329–1339 (2015).
19. Thibodeau, B.J. *et al.* Characterization of clear cell renal cell carcinoma by gene expression profiling. *Urol. Oncol.* **34**, 168.e1–168.e9 (2016).
20. Gravendeel, L.A. *et al.* Intrinsic gene expression profiles of gliomas are a better predictor of survival than histology. *Cancer Res.* **69**, 9065–9072 (2009).
21. Ha, G. *et al.* TITAN: inference of copy number architectures in clonal cell populations from tumor whole-genome sequence data. *Genome Res.* **24**, 1881–1893 (2014).
22. Andor, N., Harness, J.V., Müller, S., Mewes, H.W. & Petritsch, C. EXPANDS: expanding ploidy and allele frequency on nested subpopulations. *Bioinformatics* **30**, 50–60 (2014).
23. Andor, N. *et al.* Pan-cancer analysis of the extent and consequences of intratumor heterogeneity. *Nat. Med.* **22**, 105–113 (2016).
24. Hiley, C., de Bruin, E.C., McGranahan, N. & Swanton, C. Deciphering intratumor heterogeneity and temporal acquisition of driver events to refine precision medicine. *Genome Biol.* **15**, 453 (2014).
25. Northcott, P.A. *et al.* Medulloblastomics: the end of the beginning. *Nat. Rev. Cancer* **12**, 818–834 (2012).
26. Sturm, D. *et al.* Paediatric and adult glioblastoma: multiform (epi)genomic culprits emerge. *Nat. Rev. Cancer* **14**, 92–107 (2014).
27. Shih, D.J. *et al.* Cytogenetic prognostication within medulloblastoma subgroups. *J. Clin. Oncol.* **32**, 886–896 (2014).
28. Linehan, W.M. *et al.* Comprehensive molecular characterization of papillary renal-cell carcinoma. *N. Engl. J. Med.* **374**, 135–145 (2016).
29. Futreal, P.A. *et al.* A census of human cancer genes. *Nat. Rev. Cancer* **4**, 177–183 (2004).
30. Griffith, M. *et al.* DGIdb: mining the druggable genome. *Nat. Methods* **10**, 1209–1210 (2013).
31. Morrissy, A.S. *et al.* Divergent clonal selection dominates medulloblastoma at recurrence. *Nature* **529**, 351–357 (2016).
32. Johnson, B.E. *et al.* Mutational analysis reveals the origin and therapy-driven evolution of recurrent glioma. *Science* **343**, 189–193 (2014).
33. Geldres, C. *et al.* T lymphocytes redirected against the chondroitin sulfate proteoglycan-4 control the growth of multiple solid tumors both in vitro and in vivo. *Clin. Cancer Res.* **20**, 962–971 (2014).
34. Stein, R. *et al.* CD74: a new candidate target for the immunotherapy of B-cell neoplasms. *Clin. Cancer Res.* **13**, 5556s–5563s (2007).
35. Wu, M.R., Zhang, T., DeMars, L.R. & Sentman, C.L. B7H6-specific chimeric antigen receptors lead to tumor elimination and host antitumor immunity. *Gene Ther.* **22**, 675–684 (2015).
36. Chinnasamy, D. *et al.* Gene therapy using genetically modified lymphocytes targeting VEGFR-2 inhibits the growth of vascularized syngenic tumors in mice. *J. Clin. Invest.* **120**, 3953–3968 (2010).
37. Craddock, J.A. *et al.* Enhanced tumor trafficking of GD2 chimeric antigen receptor T cells by expression of the chemokine receptor CCR2b. *J. Immunother.* **33**, 780–788 (2010).
38. Hong, H. *et al.* Diverse solid tumors expressing a restricted epitope of L1-CAM can be targeted by chimeric antigen receptor redirected T lymphocytes. *J. Immunother.* **37**, 93–104 (2014).
39. Kakarla, S. *et al.* Antitumor effects of chimeric receptor engineered human T cells directed to tumor stroma. *Mol. Ther.* **21**, 1611–1620 (2013).
40. Lanitis, E. *et al.* Primary human ovarian epithelial cancer cells broadly express HER2 at immunologically-detectable levels. *PLoS One* **7**, e49829 (2012).
41. Pule, M.A. *et al.* Virus-specific T cells engineered to coexpress tumor-specific receptors: persistence and antitumor activity in individuals with neuroblastoma. *Nat. Med.* **14**, 1264–1270 (2008).
42. Tang, X. *et al.* T cells expressing a LMP1-specific chimeric antigen receptor mediate antitumor effects against LMP1-positive nasopharyngeal carcinoma cells in vitro and in vivo. *J. Biomed. Res.* **28**, 468–475 (2014).
43. Wang, W. *et al.* Specificity redirection by CAR with human VEGFR-1 affinity endows T lymphocytes with tumor-killing ability and anti-angiogenic potency. *Gene Ther.* **20**, 970–978 (2013).

[1]Developmental & Stem Cell Biology Program, The Hospital for Sick Children, Toronto, Ontario, Canada. [2]The Arthur and Sonia Labatt Brain Tumour Research Centre, The Hospital for Sick Children, Toronto, Ontario, Canada. [3]Department of Pediatric Oncology, Hematology, and Clinical Immunology, Medical Faculty, University Hospital Düsseldorf, Düsseldorf, Germany. [4]Department of Neuropathology, Medical Faculty, University Hospital Düsseldorf, Düsseldorf, Germany. [5]Department of Pediatric Neuro-Oncogenomics, German Cancer Consortium (DKTK) and German Cancer Research Center (DKFZ), Düsseldorf, Germany. [6]Division of Haematology/Oncology, Department of Pediatrics, The Hospital for Sick Children, Toronto, Ontario, Canada. [7]Department of Laboratory Medicine and Pathobiology, University of Toronto, Toronto, Ontario, Canada. [8]Cancer Research Program, McGill University Health Centre Research Institute, Montreal, Quebec, Canada. [9]MacFeeters-Hamilton Brain Tumour Centre, Princess Margaret Cancer Centre, University Health Network, Toronto, Ontario, Canada. [10]Division of Neurosurgery, The Hospital for Sick Children, Toronto, Ontario, Canada. [11]Canada's Michael Smith Genome Sciences Centre, BC Cancer Agency, Vancouver, British Columbia, Canada. [12]Departments of Pediatrics and Human Genetics, McGill University, Montreal, Quebec, Canada. [13]Program in Genetics and Genome Biology, The Hospital for Sick Children, Toronto, Ontario, Canada. [14]Cancer Research UK London Research Institute, London, UK. [15]Division of Molecular Genetics, German Cancer Research Center (DKFZ), Heidelberg, Germany. [16]Division of Pediatric Neurooncology, German Cancer Research Center (DKFZ), Heidelberg, Germany. [17]Informatics and Biocomputing, Ontario Institute for Cancer Research, Toronto, Ontario, Canada. [18]Department of Medical Biophysics, University of Toronto, Toronto, Ontario, Canada. [19]The Donnelly Centre, University of Toronto, Toronto, Ontario, Canada. [20]Department of Pathology, Montreal Children's Hospital, McGill University Health Centre, Montreal, Quebec, Canada. [21]Division of Experimental Medicine, McGill University, Montreal, Quebec, Canada. [22]Division of Pathology, The Hospital for Sick Children, Toronto, Ontario, Canada. [23]Division of Pediatric Oncology, Children's National Medical Center, Washington, DC, USA. [24]Division of Pediatric Neuro-Surgery, Children's National Medical Center, Washington, DC, USA. [25]Department of Neurology, Children's National Medical Center, Washington, DC, USA. [26]Clinical Cooperation Unit Neuropathology, German Cancer Research Center (DKFZ), Heidelberg, Germany. [27]German Cancer Consortium (DKTK), Heidelberg, Germany. [28]Department of Pediatric Oncology, Hematology, Immunology and Pulmonology, University Hospital Heidelberg, Heidelberg, Germany. [29]Institute of Neuropathology, University Medical Center, Hamburg-Eppendorf, Germany. [30]Research Institute Children's Cancer Center, Hamburg, Germany. [31]Pediatric Hematology and Oncology, University Medical Center, Hamburg-Eppendorf, Germany. [32]Translational Cancer Therapeutics Laboratory, The Francis Crick Institute, London, UK. [33]Cancer Research UK Lung Cancer Centre of Excellence, University College London, London, UK. [34]Department of Medical Genetics, University of British Columbia, Vancouver, British Columbia, Canada. [35]Department of Molecular Biology & Biochemistry, Simon Fraser University, Burnaby, British Columbia, Canada. [36]Division of Neurosurgery, St. Michael's Hospital, University of Toronto, Toronto, Ontario, Canada. [37]These authors contributed equally to this work. Correspondence should be addressed to M.A.M. (mmarra@bcgsc.ca) or M.D.T. (mdtaylor@sickkids.ca).

ONLINE METHODS

Patients and samples. Multiregion tumor biopsies and clinical data were gathered for 35 tumors (9 primary medulloblastomas, 16 high-grade gliomas (10 with gene expression only[12]), and 10 renal cell carcinomas[10]); peripheral blood samples were included as germline controls for all cases with exome sequencing. All multiregion biopsies for unpublished cases were obtained *in situ* during tumor resection, by mimicking the previous sample-preparation conditions of published cases to the best of our knowledge. Medulloblastoma tumors are similar in size to glioblastomas, with an average diameter of 8–12 cm; biopsies were taken from regions as far apart as possible by the surgeon. Owing to their localization in the abdomen, renal cancers may be larger in size. Detailed information on multiregion tumor samples is provided in **Supplementary Table 1a** and **Supplementary Figure 1**. All patient material and clinical information was obtained after informed consent had been received and was approved by the institutional review boards of the contributing institutions. DNA and RNA extractions were performed as previously described[16]. RNA quality was assessed on a 2100 Bioanalyzer (Agilent Technologies, Santa Clara, CA). Only high-quality RNA (RNA integrity number ≥ 7) was included for further study.

Gene expression profiling. We carried out expression profiling on eight MB and three HGG multiregion biopsies, with a total of 72 biopsies and a median number of 6 multiregion biopsies per primary tumor (range: 4–9). We used Affymetrix HU133 Plus 2.0 microarrays for HGG samples, and Affymetrix Gene 1.1 ST arrays (Affymetrix, Santa Clara, CA) for MB samples, to ensure that these multiregion biopsies could be compared to published data sets[15–17,20]. Microarrays were processed according to the manufacturer's guidelines. Raw data were normalized with a transcript-level robust multi-array average (RMA) algorithm[44], and subsequently clustered by unsupervised HCL (Pearson's dissimilarity – average linkage) in Partek Genomics Suite. The molecular classification of the multiregion biopsy samples was done with the class-prediction algorithm PAM[45], as implemented in the pamr package (v. 1.51). Markers for glioblastoma (GBM) subtypes were obtained from the Verhaak classifier[13]. We note that classification was done for the GBM samples only, thus excluding HGG1. Subgroup-specific markers for MB were identified on the basis of one-way analysis of variance with multiple hypothesis correction by the Bonferroni method in previously published data sets with known subgroup affiliation[46]. On the basis of the misclassification error values in core GBM[13] and MB[15–17] training data sets (**Supplementary Fig. 6**), we chose threshold values of 1.75 and 1 for multiregion samples from published[12] and unpublished GBM and MB patient data, respectively. The published GBM data set[12] was quantile-normalized with Partek Genomics Suite. Predicted subtypes or subgroups with confidence probabilities higher than established thresholds[46] were considered *bona fide* subgroup assignments. Samples with less than 500 ng of remaining RNA were analyzed with NanoString as previously described[46]. MB3 was analyzed exclusively with NanoString, as only limited amounts of RNA were available for all multiregion biopsies. NanoString counts were normalized to the three housekeeping genes (*GAPDH*, *ACTB* and *LDHA*). We prepared dot plots and principal component analyses based on normalized NanoString calls using the R statistical environment (v2.15.1). Pearson correlation was used to determine the correlation of marker gene expression for each biopsy per patient (intratumor comparison) and between each biopsy and all others samples from different patients of the same subgroups (intertumor comparison). The Wilcoxon rank-sum test was used to infer differences in intra- and intertumor marker gene expression in a subgroup-specific fashion.

A previously published data set of nine multiregion RCC samples[9] profiled with the Affymetrix Human Gene 1.0 ST array was included in the analysis, as well as two RCC data sets[18,19] with 53 and 29 single RCC samples, respectively. The RCC expression data sets were processed together in R (v3.1.1) with the oligo package (rma normalization), and the combat package was used for batch-effect correction. Unsupervised HCL (Pearson's dissimilarity – average linkage) was carried out with the Partek Genomics Suite.

Whole-exome sequencing. DNA libraries (MB1–5) from multiregion samples were exome-captured with Agilent SureSelect V5+UTR probes and subjected to eight cycles of PCR, and then paired-end 75-base reads were sequenced over two lanes on an Illumina HiSeq 2000 instrument per pool of six libraries. Reads were aligned to the human reference genome hg19a with Burrows–Wheeler Aligner (BWA) (version 0.5.7)[47]. Two lanes were merged with duplicates marked with Picard Tools (version 1.71). Additional samples (MB6–7 and HGG1–5) were subjected to paired-end library construction using Illumina's Nextera Rapid Capture Exome kit. Captured exome DNA sequences were then sequenced with Illumina HiSeq 2000 (rapid-run mode) for 100-bp paired-end reads. We used the FASTX toolkit to remove adaptor sequences and to trim low-quality reads. Quality trimmed reads were then aligned to the human reference genome (hg19) using BWA (version 0.5.9)[47]. We used Genome Analysis Toolkit (GATK)[48] for indel realignment. We marked duplicate reads with Picard so we could exclude them further in our analysis.

Somatic SNV detection and filtering. SNVs were called exome-wide with SAMtools mpileup (v0.1.7), and indels were called with VarScan. We carried out stringent filtering requiring no reads in the germline sample supporting an SNV to ensure conservative selection of somatic events. Variants with sufficient coverage (≥10) were further annotated with Annovar[49] (table_annovar.pl; RefSeq gene annotations, amino acid change annotation, SIFT, PolyPhen, LRT, and MutationTaster scores, PhyloP and GERP++ conservation scores, dbSNP identifiers, 1000 Genomes Project allele frequencies, NHLBI-ESP 6500 exome project allele frequencies).

Mutation validation. We validated a subset of somatic mutations using PCR amplification from all tumor biopsies, matched germline, and a healthy control sample. We amplified regions of interest from genomic DNA with primers flanking each SNV (**Supplementary Table 1h,n**), using Q5 High-Fidelity DNA polymerase (NEB). PCR specificity was determined by agarose gel electrophoresis followed by gel extraction of specific bands using a Gel Extraction/PCR clean-up kit (Qiagen) according to the manufacturer's instructions. Purified amplicons were sequenced by Sanger sequencing, and traces were reviewed manually for the expected presence or absence of the mutated base.

Droplet digital PCR. For the validation and quantification of the frequency of the PIK3CA SNV detected in MB3, we used droplet digital PCR (ddPCR), as Sanger traces were of poor quality in the region of interest. We used genomic DNA from six spatially distinct biopsies from MB3, as well as matched germline and a healthy donor control, in the assay. We validated the *PIK3CA* mutation (chr 3:178936091 G>A) by using the PrimePCR ddPCR mutation assay kit, PIK3CA p.E545K, human (Bio-Rad; dHsaCP2000075 (mutant, FAM) and dHsaCP2000076 (wild-type, VIC)), according to the manufacturer's instructions. Fluorescence measurement with a QX100 ddPCR droplet reader (Bio-Rad) was used to detect the presence of mutant and wild-type alleles. QuantaSoft Analysis software (Bio-Rad) was used in the quantification.

Copy-number analysis. TITAN[21] estimates the cellular prevalence of tumor cell populations (lineages) on the basis of a user-defined number of clonal clusters, and user-defined ploidy estimation. Thus, we carried out 20 runs of TITAN for each exome, with cluster numbers 1–10 (representing one clonal lineage through to ten coexisting clonal lineages with distinct genotypes), and ploidy set to either 2 or 4. Copy-number segments from the 20 parameter combinations were analyzed and merged into larger segments if they were on the same chromosome arm, were <10 Mb apart, and had the same state (loss or gain). We compared merged results from each of the 20 parameter combinations for each biopsy in order to select the optimal parameter combination as the highest-scoring, considering the following criteria:

```
# maximize the largest contig size
# maximize the median contig size
# minimize the number of contigs
# minimize the number of clonal clusters
```

The parameter combination with the largest x value was selected as optimal:

$$x = ((L * M) * (M^2/10^9)^* (1/T)^* (1/(C+1)^2))/M/10^9$$

where L is the largest contig size (Gb), M is the median contig size (Gb), T is the total number of contigs, and C is the number of clonal clusters.

We next assessed the prevalence of copy-number segments (loss or gain) identified in the best parameter combination of a unique biopsy (i.e., target segments), using either all segments or clonal segments only (logratio ≥ |0.2|). A target segment was considered as found in another biopsy from the same tumor if any of the 20 parameter combinations contained a segment with the same state (loss or gain), and whose span had a minimum reciprocal overlap of at least 70% with the target segment.

Concordance of driver regions of loss and gain in the RCC tumor cohort was performed for our calls and the published data[9]. With our computational approach, we achieved 97% concordance compared with the manual curation performed previously[9], indicating that this method is specific and sensitive despite the high level of normal cell contamination in these tumors. Conversely, compared to our results for the subset of copy-number gains and losses identified in ref. 9, the manual curation showed 89% concordance to the TITAN pipeline, indicating that our approach is more sensitive, and that the homogeneity of certain copy-number driver events may be greater than previously estimated (**Supplementary Table 1c**). Finally, our approach is applicable genome-wide and across tumor types in a highly parallel fashion.

SNV classification using mclust. We classified variant allele frequencies (VAFs) of somatic SNVs into distinct clusters using the R package mclust[50], which uses finite mixture estimation via iterative expectation maximization steps and the Bayesian information criterion. Each cluster is manually categorized as 'homozygous', 'clonal', or 'subclonal', depending on the cluster VAF and the uncertainty separating it from the next cluster, and taking into account the biopsy tumor cell content value reported by TITAN. Multiple subclonal populations are numbered sequentially, starting with the most highly prevalent population. Clonal and subclonal mutation details per biopsy are summarized in **Supplementary Table 1d,g**.

Phylogenetic reconstruction from combined SNV and CNA data. We combined copy number and loss-of-heterozygosity (LOH) information derived from TITAN (including the clonal and subclonal events identified in the best parameter combination run for each biopsy), as well as somatic mutations and SNPs in areas of LOH, to infer tumor phylogenies using EXPANDS[22]. We ran EXPANDS v1.7.2 with the runExPANdS function. All parameters were set to default, with the exception of maxScore, which was lowered to 1.5 to reduce the false positive rate of subpopulation detection. Only subpopulations with a minimum size (cellular frequency) of 0.1 were considered. Mutations that could not be assigned to a high-confidence subpopulation were discarded, so that no ambiguous assignments were made. In addition, ambiguous subpopulations (i.e., groups of mutations and copy-number events) were dropped from the analysis. Mutations were assigned to all nested subpopulations (i.e., if a mutation was found in a subpopulation of cells at a high frequency of 0.8, it was also assigned to 'daughter' subpopulations of, for instance, frequency 0.5), to report the assignment of every mutation to all detected subpopulations in all biopsies of the tumor (assuming that the mutation could be assigned unambiguously as mentioned above; **Supplementary Table 1f**).

Phylogenetic relationships between the subpopulations inferred by the EXPANDS algorithm in all biopsies per patient were generated using both SNV and copy-number segments. The Manhattan distance metric was used to calculate pairwise distances between all pairs of biopsies on the basis of these data, and a complete linkage HCL was performed to generate phylogenies. Germline-rooted trees were generated with the as.phylo R function from the ape package.

Error inference of actionable genetic alterations. In order to analyze genetic heterogeneity affecting actionable and putative driver genes in a way that was unbiased toward any of the tumor types, we opted to use general lists of known cancer drivers and druggable targets. Sets of genes known to be drivers in GBM, MB, and RCC tumors come from studies of different cohort sizes, with sometimes unknown subgroup affiliations, and thus are not equally comprehensive. To overcome this, we used a list of genes of interest that included putative driver genes found in the Cancer Gene Census database[29] (n = 572) and actionable genes from the Drug-Gene Interaction Database[30] (n = 426 genes) (**Supplementary Table 1l,m**).

Oncoprint plots (R package ComplexHeatmap v1.6.0) were built for the combination list of these genes for all tumors, using (a) clonal mutations and indels and (b) clonal mutations and indels plus high-level CNAs (>4 copies gained; homozygous loss). A manual review of the results showed that the absence of clonal somatic mutations in subsets of biopsies is not explained by concordant copy-number loss. Because not all biopsies had copy-number data, we carried out further analyses using results from strategy (a) in order to maximize the number of usable biopsies per tumor.

Driver event lists. The MB CNA driver events listed in **Supplementary Table 1i,j** and **Figure 4b** were taken mainly from Shih *et al.*[27], with a subset of the mostly highly recurrent genes listed in Northcott *et al.*[25]. The HGG chromosome arm and recurrent driver gene events were retrieved from Tables 1 and 2 of ref. 26. RCC chromosome arm and gene-level driver events were retrieved from Supplementary Figure 2 (threshold FDR q-value < 10^{-15}) and Table S4 (q-value threshold: 0.05) of the ccRCC TCGA paper[28]. The cancer cell fraction values presented in **Supplementary Figure 10b** for driver mutations were calculated as previously described[51]:

$$\mathrm{CCF} = \mathrm{VAF}^{*}(1/\mathrm{Purity})(\mathrm{CN}^{*}\mathrm{Purity} + 2(1 - \mathrm{Purity}))$$

where CCF is the cancer cell fraction, VAF is the variant allele frequency, CN is the copy number at the mutation, and Purity is the tumor purity as calculated by EXPANDS.

Accuracy of mutation-frequency detection. We calculated the inferred error of the prevalence of each mutation across biopsies by using a subsampling approach. In each tumor, given a subset of biopsies from 1 to n (where n is the total number of biopsies per tumor), we calculated the frequency of each identified mutation in the biopsies sampled as f_o. We subtracted this value from the 'ground truth' expected frequency for that mutation across all n biopsies (f_e). When the observed and expected values were identical, then the inferred error ($f_e - f_o$) was 0. In the majority of tumors, there is a predominance of genes with mutations in single biopsies, leading to negative values of error for many genes, as the frequency of the mutation is often overestimated (**Supplementary Fig. 17**). In contrast, genes that are present in all but one or two biopsies will often have an error value greater than 0, as their frequency can be underestimated.

The likelihood of being within ±0.1 of 0 (i.e., close to perfect accuracy, given the data from all biopsies) is calculated as the proportion of genes at each sampling of 1:n biopsies where the error rate was within those bounds. For instance, we sampled all possible combinations of a certain number of biopsies from the total number of biopsies, and in each case calculated the inferred error of each detected mutation's prevalence. The proportion of the total set of error values < |0.1| represented the likelihood of a correct interpretation of mutation frequency given that number of biopsies (**Fig. 5b**).

Estimation of genetic heterogeneity from two biopsies. To address the practical issue of estimating genetic heterogeneity from a minimum number of informative biopsies, we implemented a simple metric of the proportion of mutated genes in a set of two biopsies that was ubiquitous (i.e., present in two of two biopsies). The mean value of all pairs of biopsies from a total of n biopsies per tumor showed a strong divergence in HGG and MB tumors, with high- versus low-variability tumors well separated (**Fig. 5c**). These were the same tumors that scored as high versus low variability on the basis of the accuracy metric described above.

We also observed clear separation of these two classes with the R package mclust (**Supplementary Fig. 18a**), which models univariate mixtures of Gaussian distributions (i.e., corresponding to a mixture of high- and low-genetic-variance brain tumors) via expectation maximization and the Bayesian information criterion[50]. Using two thresholds from the mclust density peaks (low, 0.55; high, 0.75), we calculated the accuracy of the classification of high-variance versus low-variance tumors on the basis of a single pair of biopsies, and observed that high-variance tumors in particular had high true positive and low false positive classification rates (**Supplementary Fig. 18b**). On the basis of this metric, the vast majority of pairs of biopsies from tumors with high genetic heterogeneity have a low percentage of gene mutations found in both biopsies, such that they are always classified as heterogeneous tumors, and almost never as homogeneous tumors.

doi:10.1038/ng.3838

Expression analysis of immunotherapeutic targets in MB tumors. Microarray expression data from the Affymetrix Gene 1.1 ST array (Affymetrix, Santa Clara, CA) for the MB samples were analyzed in the R environment (v3.1.1). We used the affy package (v1.44.0) and the custom CDF hugene11sthsensgcdf (v19.0.0) to summarize the expression of 21,641 Ensembl (ENSG) genes and process the data. Expression data were normalized via the rma method.

Spatial genetic variance versus post-treatment clonal evolution. To directly measure the relative contributions of spatial heterogeneity and clonal evolution induced by treatment, we used our previously published cohort of matched pre- and post-therapeutic MB samples[31]. This comparison showed that in MB, the amount of divergence observed between primary and relapse compartments far exceeded the spatial genetic variance in the primary tumor.

To assess whether the observed divergence between primary and recurrent MB is greater than the observed divergence between intratumoral biopsies, we reanalyzed the 14 primary–relapse tumor whole-genome sequencing (WGS) samples with matched germline, using the same pipeline as presented above. Briefly, mutations were called using SAMtools mpileup, filtered stringently against the germline, and shortlisted to those mutations with at least ten-reads coverage in both primary and recurrent samples, and are in areas of normal copy number and LOH. Because the samples in this work were exomes, we restricted the analysis of the primary–relapse samples to the same exonic regions. After removing the major analysis pipeline differences, we addressed differences in depth of coverage. The exome libraries were sequenced to an average of 60×, and the WGS samples were sequenced to 30× coverage. Thus, our ability to assess the similarity between regions in the exome libraries was more sensitive to subclonal events present at low levels (and therefore preferentially detectable by exome sequencing, and not by WGS). We addressed this bias by restricting the analysis to clonal events in the exomes, as clonal mutations are detectable in both exomes and genomes. To verify that this was a reasonable assumption, we compared the VAF of mutations found in the exomes to those found in matched WGS data generated from the same samples, but sequenced at 30× coverage. Matched WGS samples were available for biopsy 1 in each MB tumor with multiregional profiling. In all cases, we found that >75% of mutations with a VAF < 0.18 in the MB exomes were not found in the matched genomes sequenced from the same samples, which indicates that subclonal events are typically not well profiled at the shallower depths of a genomic library. Therefore, we restricted our analysis to clonal events in both exomes and genomes.

Focusing on the clonal and homozygous events detectable in both exome and genome data, we hypothesized that any differences between primary and relapse samples that were greater than the differences expected from different biopsies in a primary tumor would be largely attributable to clonal evolution as a consequence of therapy. To see whether the data supported this conclusion, we used the mutations in each biopsy to measure the pairwise concordance between all biopsies of individual tumors. Concordance was measured as the number of mutations in common between two biopsies, as a fraction of the total number of mutations present in both. In parallel, we used the mutations in the primary and relapse samples to measure pairwise concordance values between disease compartments. As a positive control, we compared the interbiopsy and intercompartmental concordance values of an adult GBM sample with multiple biopsies profiled before and after therapy (patient 17 from ref. 32).

In MB samples we found a mean pairwise concordance of 0.3903 between biopsies of the same tumor—nearly an order of magnitude higher than the mean concordance (0.03852) observed between disease compartments (Wilcoxon rank-sum test P value < 2.2×10^{-16}). One sample stood out as an outlier (MB-REC-04), and we note that in that case the tumor was a group 4 local recurrence. This unusual pattern of recurrence for a group 4 tumor may indicate that the primary mass was sub-totally resected rather than grossly resected, thus explaining the higher similarity of the recurrent compartment to the primary.

In the case of the adult GBM patient (patient 17) with multiregionally sampled primary (three regions; low-grade glioma) and recurrent disease (four regions; high-grade glioma), we found the same trend: the primary–relapse mean concordance of 0.01506 was an order of magnitude smaller than the mean intrabiopsy concordance of 0.5036 (Wilcoxon rank-sum test P value = 0.0001406). There was no significant difference between the primary–relapse MB concordance and the primary–relapse GBM concordance observed in patient 17 (Wilcoxon rank-sum test P value = 0.5458). Similarly, there was no significant difference between the regional biopsies in GBM versus MB (Wilcoxon rank-sum test P value = 0.09926).

Finally, the primary–relapse divergence calculated from reprocessed data from patient 17 was on par with that initially presented in the glioma paper[41]; thus we included, for visual comparison, all the primary–relapse values for the glioma cohort in **Figure 6a** (middle panel; values directly derived from Supplementary Table 4 of ref. 32).

Statistical analysis. All statistical analyses were performed in the R statistical environment. Comparisons of categorical variables between entity types were done by two-sided Fisher's exact test. Comparisons of distributions were done by Welch two-sample t-test (parametric) or Wilcoxon rank-sum test (nonparametric). P values < 0.05 were considered statistically significant.

Data availability. The Gene Expression Omnibus accession codes for the previously unpublished gene expression data are GSE62802 (HGG samples) and GSE62803 (MB samples). The Toronto whole-exome sequencing data sets have been deposited in the European Genome-phenome Archive under accession codes EGAD00001000723 and EGAS00001001014.

44. Irizarry, R.A. *et al.* Summaries of Affymetrix GeneChip probe level data. *Nucleic Acids Res.* **31**, e15 (2003).
45. Tibshirani, R., Hastie, T., Narasimhan, B. & Chu, G. Diagnosis of multiple cancer types by shrunken centroids of gene expression. *Proc. Natl. Acad. Sci. USA* **99**, 6567–6572 (2002).
46. Northcott, P.A. *et al.* Rapid, reliable, and reproducible molecular sub-grouping of clinical medulloblastoma samples. *Acta Neuropathol.* **123**, 615–626 (2012).
47. Li, H. & Durbin, R. Fast and accurate short read alignment with Burrows-Wheeler transform. *Bioinformatics* **25**, 1754–1760 (2009).
48. McKenna, A. *et al.* The Genome Analysis Toolkit: a MapReduce framework for analyzing next-generation DNA sequencing data. *Genome Res.* **20**, 1297–1303 (2010).
49. Wang, K., Li, M. & Hakonarson, H. ANNOVAR: functional annotation of genetic variants from high-throughput sequencing data. *Nucleic Acids Res.* **38**, e164 (2010).
50. Fraley, C., Raftery, A., Murphy, T.B. & Scrucca,, L. *mclust Version 4 for R: Normal Mixture Modeling for Model-Based Clustering, Classification, and Density Estimation* (University of Washington, 2012).
51. Stephens, P.J. *et al.* The landscape of cancer genes and mutational processes in breast cancer. *Nature* **486**, 400–404 (2012).

Article

Cancer Cell

Intertumoral Heterogeneity within Medulloblastoma Subgroups

Graphical Abstract

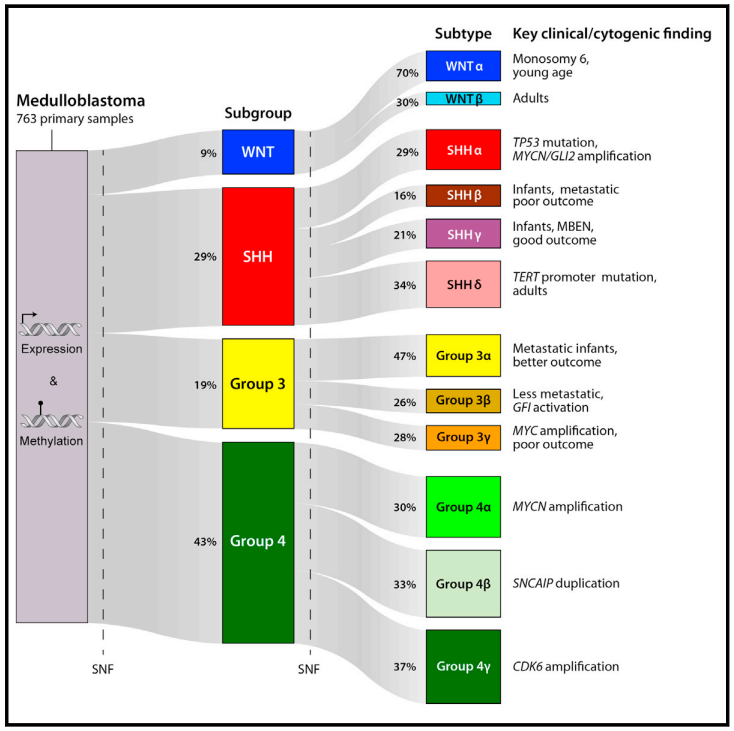

Highlights

- Medulloblastoma comprises 12 subtypes; 2 WNT, 4 SHH, 3 group 3, and 3 group 4 groups
- Heterogeneity within subgroups accounts for previously unexplained variation
- Groups 3 and 4 medulloblastoma are molecularly distinct entities
- Clinically and biologically relevant subtypes exist for each subgroup

Authors

Florence M.G. Cavalli, Marc Remke, Ladislav Rampasek, ..., Anna Goldenberg, Vijay Ramaswamy, Michael D. Taylor

Correspondence

anna.goldenberg@utoronto.ca (A.G.), vijay.ramaswamy@sickkids.ca (V.R.), mdtaylor@sickkids.ca (M.D.T.)

In Brief

Cavalli et al. analyze 763 primary medulloblastoma samples using the similarity network fusion approach. They identify subtypes that have distinct somatic copy-number aberrations, activated pathways, and clinical outcomes within each of the four known subgroups and further delineate group 3 from group 4 MB.

Cavalli et al., 2017, Cancer Cell *31*, 737–754
June 12, 2017
http://dx.doi.org/10.1016/j.ccell.2017.05.005

Cancer Cell
Article

Intertumoral Heterogeneity within Medulloblastoma Subgroups

Florence M.G. Cavalli,[1,2,80] Marc Remke,[3,4,71,80] Ladislav Rampasek,[5,6] John Peacock,[1,2,4] David J.H. Shih,[1,2,4] Betty Luu,[1,2] Livia Garzia,[1,2] Jonathon Torchia,[1,4] Carolina Nor,[1,2] A. Sorana Morrissy,[1,2] Sameer Agnihotri,[7] Yuan Yao Thompson,[1,2,4] Claudia M. Kuzan-Fischer,[1,2] Hamza Farooq,[1,2,4] Keren Isaev,[8,9] Craig Daniels,[1,2] Byung-Kyu Cho,[10] Seung-Ki Kim,[10] Kyu-Chang Wang,[10] Ji Yeoun Lee,[10] Wieslawa A. Grajkowska,[11]

(Author list continued on next page)

[1]The Arthur and Sonia Labatt Brain Tumour Research Centre
[2]Developmental & Stem Cell Biology Program
The Hospital for Sick Children, Toronto, ON M5G 1X8, Canada
[3]Department of Pediatric Oncology, Hematology, and Clinical Immunology, Medical Faculty, University Hospital Düsseldorf, Düsseldorf 40225, Germany
[4]Department of Laboratory Medicine and Pathobiology, University of Toronto, Toronto, ON M5S 1A1, Canada
[5]Department of Computer Science, University of Toronto, Toronto, ON M5S 2E4, Canada
[6]Program in Genetics and Genome Biology, The Hospital for Sick Children, Toronto, ON M5G 1X8, Canada
[7]UPCI Brain Tumor Program, University of Pittsburgh, Children's Hospital of Pittsburgh, Pittsburgh, PA 15224, USA
[8]Informatics Program, Ontario Institute for Cancer Research, Toronto, ON M5G 0A3, Canada
[9]Department of Medical Biophysics, University of Toronto, Toronto, ON M5G 1L7, Canada
[10]Department of Neurosurgery, Division of Pediatric Neurosurgery, Seoul National University Children's Hospital, Seoul 30322, South Korea
[11]Department of Pathology

(Affiliations continued on next page)

SUMMARY

While molecular subgrouping has revolutionized medulloblastoma classification, the extent of heterogeneity within subgroups is unknown. Similarity network fusion (SNF) applied to genome-wide DNA methylation and gene expression data across 763 primary samples identifies very homogeneous clusters of patients, supporting the presence of medulloblastoma subtypes. After integration of somatic copy-number alterations, and clinical features specific to each cluster, we identify 12 different subtypes of medulloblastoma. Integrative analysis using SNF further delineates group 3 from group 4 medulloblastoma, which is not as readily apparent through analyses of individual data types. Two clear subtypes of infants with Sonic Hedgehog medulloblastoma with disparate outcomes and biology are identified. Medulloblastoma subtypes identified through integrative clustering have important implications for stratification of future clinical trials.

INTRODUCTION

Genomics has substantially advanced our understanding of medulloblastoma (Northcott et al., 2012a; Ramaswamy et al., 2011). While historically considered one entity, it is now clearly accepted that medulloblastoma comprises at least four distinct entities: WNT, SHH, group 3, and group 4; as reflected in the current revision of the WHO classification (Louis et al., 2016;

Significance

While medulloblastoma is widely recognized as comprising four distinct subgroups, the degree of heterogeneity within the four subgroups, and the extent of overlap between the four subgroups is unknown. Applying similarity network fusion to integrate gene expression and DNA methylation profiling, we demonstrate that the degree of overlap between groups 3 and 4 is minimal after accounting for both expression and DNA methylation data. We identify medulloblastoma subtypes within each of the subgroups that have distinct somatic copy-number aberrations, differentially activated pathways, and disparate clinical outcomes. Integrated analysis has refined the boundaries between the four medulloblastoma subgroups, and identified clinically and biologically relevant subtypes, which will inform and improve preclinical modeling, as well as refine our current clinical classification.

Marta Perek-Polnik,[12] Alexandre Vasiljevic,[13,72] Cecile Faure-Conter,[14] Anne Jouvet,[15] Caterina Giannini,[16] Amulya A. Nageswara Rao,[17] Kay Ka Wai Li,[18] Ho-Keung Ng,[18] Charles G. Eberhart,[19] Ian F. Pollack,[20] Ronald L. Hamilton,[21] G. Yancey Gillespie,[22] James M. Olson,[23,24] Sarah Leary,[24] William A. Weiss,[25] Boleslaw Lach,[26,73] Lola B. Chambless,[27] Reid C. Thompson,[27] Michael K. Cooper,[28] Rajeev Vibhakar,[29] Peter Hauser,[30] Marie-Lise C. van Veelen,[31] Johan M. Kros,[32] Pim J. French,[33] Young Shin Ra,[34] Toshihiro Kumabe,[35] Enrique López-Aguilar,[36] Karel Zitterbart,[37] Jaroslav Sterba,[37] Gaetano Finocchiaro,[38] Maura Massimino,[39] Erwin G. Van Meir,[40] Satoru Osuka,[40] Tomoko Shofuda,[41] Almos Klekner,[42] Massimo Zollo,[43] Jeffrey R. Leonard,[44] Joshua B. Rubin,[45] Nada Jabado,[46] Steffen Albrecht,[47,74] Jaume Mora,[48] Timothy E. Van Meter,[49] Shin Jung,[50]

(Author list continued on next page)

[12]Department of Oncology
The Children's Memorial Health Institute, University of Warsaw, Warsaw 04-730, Poland
[13]Centre de Pathologie et Neuropathologie Est, Centre de Biologie et Pathologie Est, Groupement Hospitalier Est, Hospices Civils de Lyon, Bron 69677, France
[14]Institute of Pediatric Hematology and Oncology, Lyon 69008, France
[15]Centre de Pathologie EST, Groupement Hospitalier EST, Université de Lyon, Bron 69677, France
[16]Department of Laboratory Medicine and Pathology
[17]Division of Pediatric Hematology/Oncology
Mayo Clinic, Rochester, MN 55905, USA
[18]Department of Anatomical and Cellular Pathology, The Chinese University of Hong Kong, Shatin, New Territories, Hong Kong, China
[19]Departments of Pathology, Ophthalmology and Oncology, John Hopkins University School of Medicine, Baltimore, MD 21287, USA
[20]Department of Neurological Surgery, University of Pittsburgh School of Medicine, Pittsburgh, PA 15213, USA
[21]Department of Pathology, University of Pittsburgh School of Medicine, Pittsburgh, PA 15261, USA
[22]Department of Surgery, Division of Neurosurgery, University of Alabama at Birmingham, Birmingham, AL 35233, USA
[23]Clinical Research Division, Fred Hutchinson Cancer Research Center, Seattle, WA 98109-1024, USA
[24]Division of Pediatric Hematology/Oncology, University of Washington School of Medicine, Seattle Children's Hospital, Seattle, WA 98145-5005, USA
[25]Departments of Pediatrics, Neurological Surgery and Neurology, University of California San Francisco, San Francisco, CA 94143-0112, USA
[26]Division of Anatomical Pathology, Department of Pathology and Molecular Medicine, McMaster University, Hamilton, ON L8S 4K1, Canada
[27]Department of Neurological Surgery
[28]Department of Neurology
Vanderbilt Medical Center, Nashville, TN 37232, USA
[29]Department of Pediatrics, University of Colorado Denver, Aurora, CO 80045, USA
[30]2nd Department of Pediatrics, Semmelweis University, Budapest 1094, Hungary
[31]Department of Neurosurgery, Erasmus University Medical Center, Rotterdam 3015 CE, the Netherlands
[32]Department of Pathology, Erasmus University Medical Center, Rotterdam 3015 CN, the Netherlands
[33]Department of Neurology, Erasmus University Medical Center, Rotterdam 3015 CE, the Netherlands
[34]Department of Neurosurgery, University of Ulsan, Asan Medical Center, Seoul 05505, South Korea
[35]Department of Neurosurgery, Kitasato University School of Medicine, Sagamihara, Kanagawa 252-0374, Japan
[36]Division of Pediatric Hematology/Oncology, Hospital Pediatría Centro Médico Nacional Century XXI, Mexico City 06720, Mexico
[37]Department of Pediatric Oncology, School of Medicine, Masaryk University, Brno 625 00, Czech Republic
[38]Department of Neuro-Oncology, Istituto Neurologico Besta
[39]Fondazione IRCCS Istituto Nazionale Tumori
Milan 20133, Italy
[40]Department of Hematology & Medical Oncology, School of Medicine and Winship Cancer Institute, Emory University, Atlanta, GA 30322, USA
[41]Division of Stem Cell Research, Institute for Clinical Research, Osaka National Hospital, Osaka 540-0006, Japan
[42]Department of Neurosurgery, University of Debrecen, Medical and Health Science Centre, Debrecen 4032, Hungary
[43]Dipartimento di Biochimica e Biotecnologie Mediche, University of Naples, Naples 80145, Italy

(Affiliations continued on next page)

Ramaswamy et al., 2016a). These four subgroups have distinct transcriptional profiles, copy-number aberrations, somatic mutations, and clinical outcomes (Morrissy et al., 2016; Northcott et al., 2012a; Ramaswamy et al., 2016b; Ramaswamy et al., 2013). Indeed, current clinical trials and risk stratification biomarkers incorporate the four molecular subgroups (Ramaswamy et al., 2016a), as do preclinical modeling and the development of novel therapeutics (Pei et al., 2016). However, the extent to which there are additional layers of heterogeneity within the medulloblastoma subgroups is unknown, and a concerted global effort to analyze a very large cohort of tumors will be needed to resolve the question.

WNT and SHH medulloblastomas are clearly identifiable and separable across the majority of transcriptional and methylation profiling studies, demonstrating minimal overlap with other subgroups (Taylor et al., 2012). Clear heterogeneity exists within the SHH subgroup, which includes infants, children, and adults, although the extent and nature of the substructure is not clearly

Andrew S. Moore,[51,75] Andrew R. Hallahan,[51,75] Jennifer A. Chan,[52] Daniela P.C. Tirapelli,[53] Carlos G. Carlotti,[53] Maryam Fouladi,[54] José Pimentel,[55] Claudia C. Faria,[56] Ali G. Saad,[57] Luca Massimi,[58] Linda M. Liau,[59] Helen Wheeler,[60] Hideo Nakamura,[61] Samer K. Elbabaa,[62] Mario Perezpeña-Diazconti,[63] Fernando Chico Ponce de León,[64] Shenandoah Robinson,[65] Michal Zapotocky,[66] Alvaro Lassaletta,[66] Annie Huang,[1,66] Cynthia E. Hawkins,[1,67] Uri Tabori,[1,66] Eric Bouffet,[1,66] Ute Bartels,[66] Peter B. Dirks,[1,68] James T. Rutka,[1,4,68] Gary D. Bader,[69,76,77,78,79] Jüri Reimand,[8,9] Anna Goldenberg,[5,6,*] Vijay Ramaswamy,[1,66,70,**] and Michael D. Taylor[1,2,4,68,81,***]

[44]Division of Pediatric Neurosurgery, Department of Neurosurgery
[45]Departments of Pediatrics, Anatomy and Neurobiology
Washington University School of Medicine and St. Louis Children's Hospital, St. Louis, MO 63110, USA
[46]Division of Hematology/Oncology, Department of Pediatrics
[47]Department of Pathology
McGill University, Montreal, QC H4A 3J1, Canada
[48]Developmental Tumor Biology Laboratory, Hospital Sant Joan de Déu, Esplugues de Llobregat, Barcelona 08950, Spain
[49]Department of Pediatrics, Virginia Commonwealth University, School of Medicine, Richmond, VA 23298-0646, USA
[50]Department of Neurosurgery, Chonnam National University Research Institute of Medical Sciences, Chonnam National University Hwasun Hospital and Medical School, Hwasun-gun 519-763, Chonnam South Korea
[51]Lady Cilento Children's Hospital, The University of Queensland, Brisbane QLD 4102, Australia
[52]Department of Pathology and Laboratory Medicine, University of Calgary, Calgary, AB T2N 2T9, Canada
[53]Department of Surgery and Anatomy, Faculty of Medicine of Ribeirão Preto, University of São Paulo, São Paulo 14049-900, Brazil
[54]Division of Hematology/Oncology, University of Cincinnati, Cincinnati Children's Hospital Medical Center, Cincinnati, OH 45229, USA
[55]Divison of Pathology
[56]Division of Neurosurgery
Centro Hospitalar Lisboa Norte, Hospital de Santa Maria, Lisbon 1649-035, Portugal
[57]Department of Pathology, University of Arkansas for Medical Sciences, Little Rock, AR 72205, USA
[58]Department of Pediatric Neurosurgery, Catholic University Medical School, Rome 00198, Italy
[59]Department of Neurosurgery, David Geffen School of Medicine at UCLA, Los Angeles, CA 90095, USA
[60]Kolling Institute of Medical Research, The University of Sydney, Sydney, NSW 2065, Australia
[61]Department of Neurosurgery, Kumamoto University Graduate School of Medical Science, Kumamoto 860-8555, Japan
[62]Division of Pediatric Neurosurgery, Department of Neurosurgery, Saint Louis University School of Medicine, St. Louis, MO, USA
[63]Department of Pathology
[64]Department of Neurosurgery
Hospital Infantil de Mexico Federico Gomez, Mexico City 06720, Mexico
[65]Division of Pediatric Neurosurgery, Rainbow & Babies Children's Hospital, Case Western Reserve, Cleveland, OH 44106, USA
[66]Division of Haematology / Oncology
[67]Division of Pathology
[68]Division of Neurosurgery
The Hospital for Sick Children, Toronto, ON M5G 1X8, Canada
[69]The Donnelly Centre, University of Toronto, Toronto, ON M5S 3E1, Canada
[70]Program in Neuroscience and Mental Health and Division of Neurology, The Hospital for Sick Children, Toronto, ON M5G 1X8, Canada
[71]Department of Pediatric Neuro-Oncogenomics, German Cancer Consortium (DKTK) and German Cancer Research Center (DKFZ), Düsseldorf 40225, Germany
[72]ONCOFLAM - Neuro-Oncologie et Neuro-Inflammation Centre de Recherche en Neurosciences de Lyon, Lyon 69008, France
[73]Department of Pathology and Laboratory Medicine, Hamilton General Hospital, Hamilton, ON L8L 2X2, Canada
[74]Department of Pathology, Montreal Children's Hospital, Montreal, QC H4A 3J1, Canada
[75]Oncology Service, Children's Health Queensland Hospital and Health Service, South Brisbane, QLD 4029, Australia
[76]Banting and Best Department of Medical Research, University of Toronto, Toronto, ON M5G 1L6, Canada
[77]McLaughlin Centre, University of Toronto, Toronto, ON M5G 0A4, Canada
[78]Department of Molecular Genetics, University of Toronto, Toronto, ON M5S 1A8, Canada
[79]Samuel Lunenfeld Research Institute at Mount Sinai Hospital, University of Toronto, Toronto, ON M5G 1X5, Canada
[80]These authors contributed equally
[81]Lead Contact
*Correspondence: anna.goldenberg@utoronto.ca (A.G.), vijay.ramaswamy@sickkids.ca (V.R.), mdtaylor@sickkids.ca (M.D.T.)
http://dx.doi.org/10.1016/j.ccell.2017.05.005

defined (Northcott et al., 2011; Kool et al., 2014; Lafay-Cousin et al., 2016). The transcriptomes of group 3 and group 4 medulloblastoma are more similar to each other, and several cytogenetic features, such as isochromosome 17q (i17q), are found in both groups (Taylor et al., 2012). In response to this, the recent revision of WHO Classification of CNS Tumors has assigned groups 3 and 4 as provisional entities, and a recent consensus on high-risk medulloblastoma left this question unresolved (Louis et al., 2016). Establishing the nature of the boundary between group 3 and group 4 is of clinical importance as outcomes differ, particularly in the setting of upfront metastatic dissemination (Ramaswamy et al., 2016a, 2016b; Thompson et al., 2016).

Genome-wide transcriptional arrays and/or genome-wide methylation arrays are the current gold standard for medulloblastoma subgrouping (Ramaswamy et al., 2016a). These approaches have been used independently with the underlying assumption that they identify similar, perhaps even identical

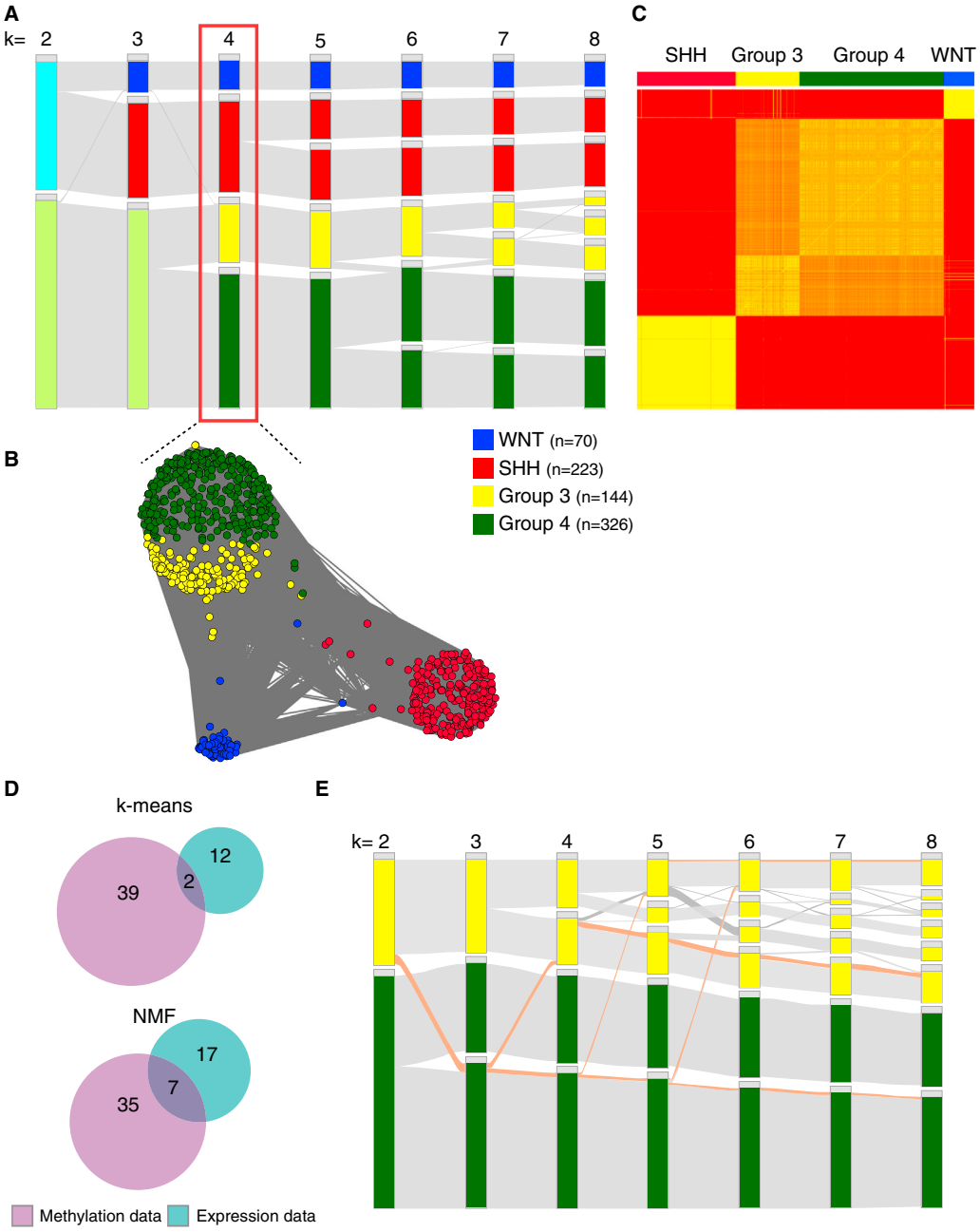

Figure 1. Clear Separation of the Four Medulloblastoma Subgroups through Integrative SNF Clustering

(A) Tumor clusters obtained by spectral clustering (for k = 2 to 8 groups) on the SNF network fused data obtained from both gene expression and DNA methylation data on 763 primary medulloblastomas. Relationships between tumors are indicated by the gray bars between columns. k = 4 (red box), defines the four recognized subgroups.

(B) Network representation of the relationships between tumors (k = 4). The shorter the edge between samples (nodes) is the more similar the samples are (only edges with a similarity value above the median value of all patient to patient similarity values are displayed).

(C) Heatmap representation of the sample-to-sample fused network data sorted by cluster for k = 4. Sample similarity is represented by red (less similar) to yellow (more similar) coloring inside the heatmap.

(D) Venn diagram showing the number of samples intermediate between groups 3 and 4 when using k-means or NMF clustering method on just expression or just methylation datasets of group 3 and 4 tumors (n = 470) between k = 2 and 3.

(legend continued on next page)

patient clusters. However, the subgroups identified using the two data types in isolation have not been compared head to head. More recently, methods of integrative clustering that analyze multiple data types in aggregate have been developed, including similarity network fusion (SNF) (Wang et al., 2014). Integrative approaches using multiple data types have been suggested to provide superior results compared with the analysis of single data types in isolation. SNF creates a unified view of patients based on multiple heterogeneous data sources, as it can integrate both gene- and non-gene-based data. SNF avoids the bias of genes or features pre-selection, is robust to different types of noise, is highly scalable, and has been shown to outperform other approaches for data integration (Wang et al., 2014).

Prior reports have recognized the existence of additional substructure within the four consensus subgroups, particularly within groups 3 and 4 (Cho et al., 2011). Consequently, a medulloblastoma consensus conference established that subdivisions within the known subgroups would be defined as subtypes, and labeled α, β, γ, δ, ε, etc. (Taylor et al., 2012). In this study our goal was to resolve intra-subgroup heterogeneity and identify biologically distinct and clinically relevant medulloblastoma subtypes by studying a very large cohort of primary tumor samples.

RESULTS

Integrated Clustering of Primary Medulloblastomas Recovers the Four Subgroups and Further Separates Group 3 from Group 4 Tumors

Through the Medulloblastoma Advanced Genomics International Consortium, we assembled a cohort of 763 primary frozen medulloblastoma samples with high-quality DNA and RNA, and generated genome-wide methylation and expression profiles. Of these, 491 had DNA copy-number profiles generated by Affymetrix SNP6 microarrays (Northcott et al., 2012b). Clinical data including age, tumor histology, metastatic status, and survival were available on 95.7%, 76.9%, 75.2%, and 82% of cases, respectively (Table S1). Arm-level somatic copy-number aberrations (SCNA) were inferred from methylation arrays in 100% of cases.

To these samples, we applied SNF to integrate both gene expression and DNA methylation data, followed by spectral clustering ranging from 2 to 12 groups. At k = 4, four distinct subgroups are clearly identified. Those groups correspond clinically and structurally to the previously described consensus subgroups: WNT (n = 70), SHH (n = 223), group 3 (n = 144), and group 4 (n = 326) (Figures 1A–1C and S1A–S1F) (Taylor et al., 2012).

Groups 3 and 4 are more similar to each other than to SHH and WNT (Figures 1B and 1C). We tested the stability of these core subgroups, by counting samples that switch subgroup affiliation when the number of clusters increases (Figure 1A). Following each sample from k = 4 to k = 12, no sample changed affiliation between WNT and SHH, while a small minority of samples moved between groups 3 and 4.

To determine the degree of overlap between groups 3 and 4, we undertook unsupervised clustering of 470 group 3 and 4 tumors using DNA methylation array data only, and then subsequently using transcriptional profiling data only. Both k-means and non-negative matrix factorization (NMF) consensus clustering revealed a small subset of tumors (2.9%–8.9%) that switched subgroup between k = 2 and k = 3 as determined through analysis of either transcriptional or methylation data (Figures S1G and S1H). Strikingly, the set of "ambiguous group 3–4 tumors" identified by gene expression profiling had very little overlap with those identified by DNA methylation profiling (Figure 1D) suggesting that the identification of the ambiguity may be a limitation of the particular type of measurement or data, rather than the identification of a truly distinct biological subtype. Examination of tumors within the "overlap" group does not reveal any demographic, clinical, or genetic commonalities, suggesting that it could be an artifact rather than a biologically discrete, clinically important group. Subsequent application of SNF and spectral clustering to this cohort of group 3 and 4 samples demonstrates that only 13/470 (2.8%) of samples change subgroup between k = 2 to k = 3, and of these 13 only 3 (0.64%) do not track back to their original subgroup when k > 3 (Figures 1E and S1I). We conclude that group 3 and group 4 medulloblastomas are stable, mostly non-overlapping molecular subgroups, and that SNF followed by spectral clustering is a more robust method of delineating subgroups than using a single data type in isolation.

Integrated Clustering Identifies 12 Medulloblastoma Subtypes

We applied SNF and spectral clustering within each of the four subgroups as defined by k = 4 across the entire cohort to determine the extent and nature of intra-subgroup heterogeneity. SNF and spectral clustering were selected to reduce the noise introduced by biased feature selection, and to leverage the full spectrum of our dataset. We identified clusters from k = 2 to k = 8 within each subgroup. In addition, we applied seven different machine-learning classifiers to predict the SNF subtypes. Cluster assignments from spectral clustering on the SNF fused similarity matrix was used as the "ground truth" subtype assignments. We split the dataset into a 70% training set and 30% testing set, trained the various classification models in 5-fold cross-validation on the training set and repeated the procedure 100 times (Table S2). We then applied the following criteria a priori to select the optimal number of subtypes: (1) how similar are the SNF clusters on the sample-to-sample heatmap? (2) How subtype specific are the broad and focal SCNA? (3) How relevant are the clinical associations? (4) How robustly can these subtypes be predicted using supervised machine learning? Using these criteria, we identified 12 subtypes: two WNT, four SHH, three group 3, and three group 4. For each solution, we identified focal SCNA from SNP6 data and arm-level copy-number gains and losses using copy-number states inferred from the methylation arrays.

(E) Tumor clusters obtained through spectral clustering on the SNF network fused data of group 3 and 4 samples (n = 470). A small minority of samples (n = 13, 2.8%) that were initially classified as group 3 samples at k = 2, subsequently move to group 4 at k = 3. Only 3/470 (0.64%) samples remain in group 4 after k = 5. These samples are tracked up to k = 8 (orange).
See also Figures S1, S3 and Table S1.

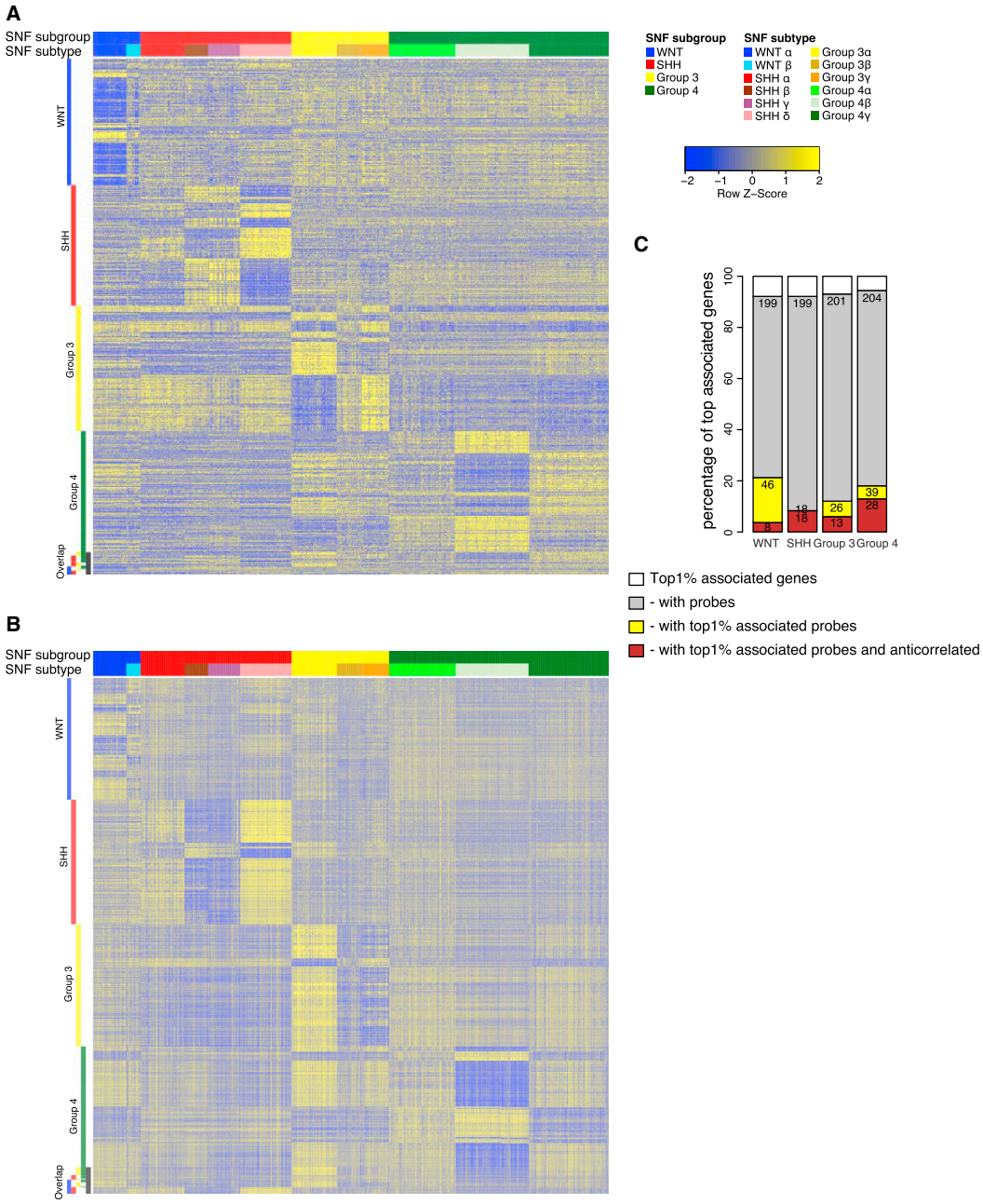

Figure 2. Differential Set of Associated Genes and Methylation Probes across the 12 Subtypes

(A and B) Heatmap of the top 1% most associated genes (A) and the top 1% most associated methylation probes (B) for the subtypes inside each subgroup (left side color bar), respectively. Top color bars indicate the subgroup and subtype sample affiliation. Samples are ordered by subtype.

(C) Percentage of genes associated for each subgroup; (1) that have methylation probes in their promoter region, (2) for which those methylation probes are in the top 1% associated probes of the respective subgroup, and (3) for which an anti-correlation can be detected between the gene expression and methylation probes levels inside the subgroup. The numbers of genes in each category are indicated.

See also Figure S2 and Tables S2 and S3.

For each subgroup, we identified the top associated genes and methylation probes that best support the final subtypes. Analysis of the top 1% of the associated genes and methylation probes for each subgroup demonstrates that the subgroups are supported by specific gene sets and methylation probes that vary substantially across subtypes (Figures 2A, 2B, and S2A–S2D;

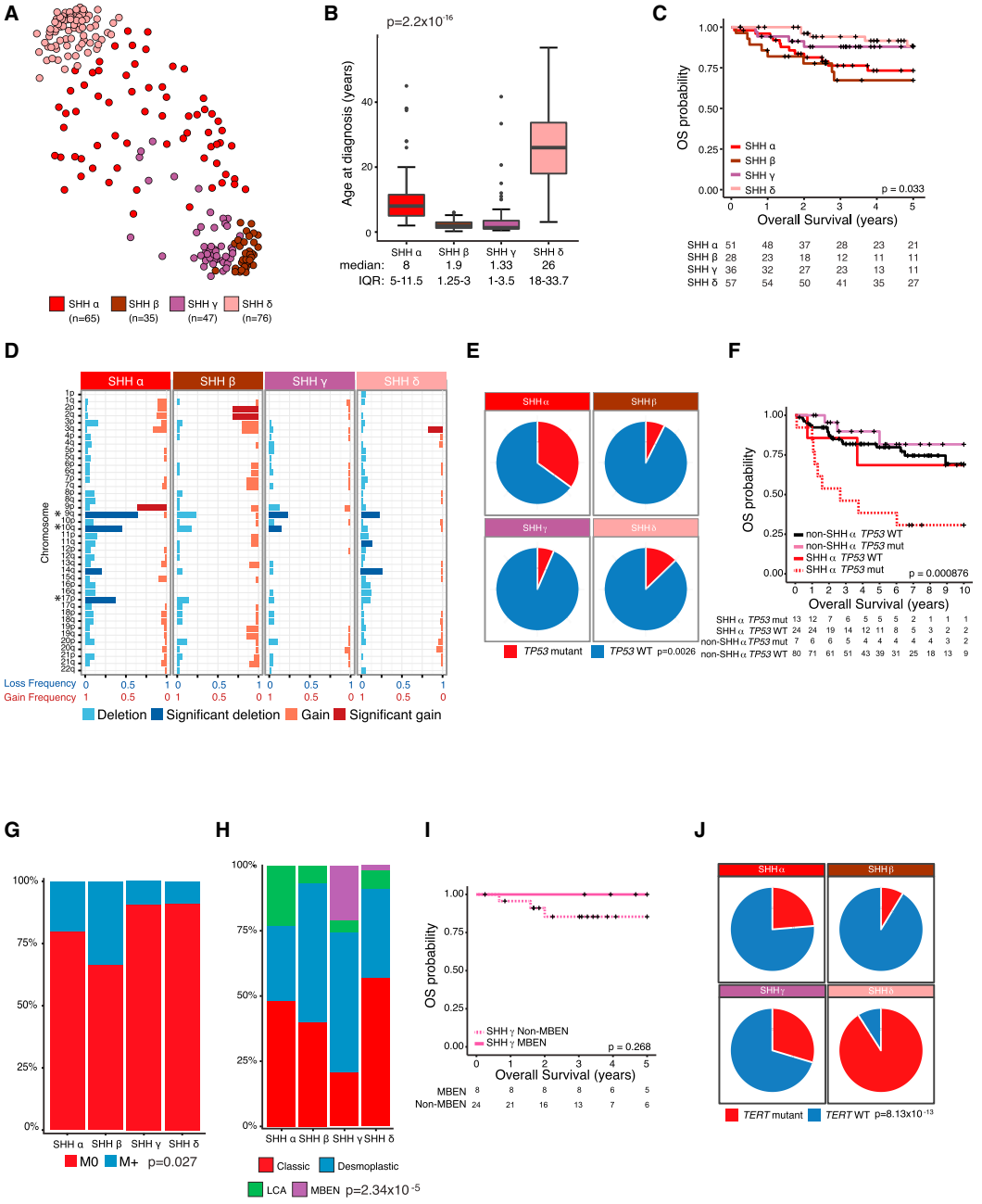

Figure 3. Clinical and Genomic Characteristics between Four SHH Medulloblastoma Subtypes

(A) Network representation map of k = 4 SNF-derived subtypes.

(B) Age at diagnosis for SHH subtypes at k = 4 (Kruskal-Wallis test). Boxplot center lines show data median; box limits indicate the 25th and 75th percentiles; lower and upper whiskers extend 1.5 times the interquartile range (IQR) from the 25th and 75th percentiles, respectively. Outliers are represented by individual points.

(C) Overall survival of SHH subtypes (log rank test). + indicates censored cases.

(D) Frequency and significance of broad cytogenetic events across the four SHH subtypes. Darker bars show significant arm-level copy-number event ($q \leq 0.1$, chi-square test). * indicates key statistically significant arm gain or deletion.

(E) Distribution of *TP53* mutations across SHH subtypes (Pearson's chi-square test).

(F) Overall survival stratified by *TP53* mutation within SHH α and non-SHH α (log rank test). + indicates censored cases.

(G) Incidence of metastatic dissemination at diagnosis across the four SHH subtypes (chi-square test).

(legend continued on next page)

Table S3). We evaluated the relationship between the associated genes and methylation probes in each subgroup. We first evaluated the number of associated genes that had methylation probes in their promoter region. Then we identified the subset of associated genes for which those probes were subgroup associated, and finally checked if we could detect an anti-correlation between the associated gene expression and the associated probe methylation levels. Only 3.7%, 8.3%, 6%, and 13% of WNT, SHH, group 3, and group 4 associated genes, respectively, follow all the criteria described above (Figure 2C). Therefore, only a small percentage of the associated genes are directly affected by DNA methylation. This is in support of both DNA methylation and gene expression contributing to the heterogeneity observed within each subgroup.

Integrative Clustering of DNA Methylation and Gene Expression Overcomes Discrepancies in Single Dataset Analysis at Defining Subtypes

To determine whether analysis of a single data type in isolation yielded similar results, we performed NMF clustering using gene expression or DNA methylation data individually. Using NMF clustering of the most variable expressed genes and methylated probes, we found that the two different types of data yield discordant subtypes as defined by both the cophenetic coefficient and silhouette value (>0.9) criteria (Figures S3A–S3D). In addition, the group memberships between the two modalities are divergent, indicating a lack of agreement between expression and methylation when analyzed in isolation (Figures S3E–S3H). When compared with the SNF subtypes, we found important differences, suggesting that both methylation and expression signatures contribute significantly and differently to define heterogeneity within the four subgroups; the data types provide distinct but complementary signals that improve over single-modality analyses. The subtypes identified by SNF are truly a combination of information present in both datasets, and therefore both data types are required to gauge the true intertumoral heterogeneity of medulloblastoma. For example, we observe that SHH α is mainly supported by the methylation data, but the defined group does not contain all SHH α samples (61%, Figure S3B). SHH δ is strongly supported by both the expression and methylation data (Figure S3B). In addition, groups 3β and 3γ are mainly defined by the signatures found in the expression data and do not separate well using the methylation data alone (Figure S3C). Finally, group 4γ is very well supported by the methylation data, and corresponds to a group obtained with the expression data, but this latter group is missing 24.4% of group 4γ samples (Figure S3D). Group 4β is well supported by both data types (Figure S3D). We conclude that methylation and expression data are complimentary, and an integrated approach allows a unified view of the underlying groups that is very valuable in elucidating heterogeneity within subgroups.

SHH Subtypes

Applying SNF and spectral clustering on SHH subgroup samples at k = 4 identified four clinically and cytogenetically distinct groups: SHH α (n = 65), SHH β (n = 35), SHH γ (n = 47), and SHH δ (n = 76) (Figures 3A, S4A, and S4B). SHH α tumors primarily affect children aged 3–16 years (Figure 3B), have the worst prognosis (p = 0.03, log rank test, Figure 3C), and are enriched for *MYCN* amplifications (SHH α 8/37, β 3/23, γ 0/29, δ 1/48; p = 0.0034 Pearson's chi-square test), and *GLI2* amplifications (SHH α 6/37, β 0/23, γ 0/29, δ 0/48; p = 0.0002 Pearson's chi-square test, Figure S4C; Table S4). Specific CNAs including 9q loss (SHH α 42/65, β 8/35, γ 11/47, δ 17/76; $p = 2.94 \times 10^{-7}$ Pearson's chi-square test), 10q loss (SHH α 29/65, β 6/35, γ 7/47, δ 6/76; $p = 1.54 \times 10^{-5}$ Pearson's chi-square test), 17p loss (SHH α 24/65, β 5/35, γ 3/47, δ 8/76; $p = 3.44 \times 10^{-5}$ Pearson's chi-square test, Figure 3D), and *YAP1* amplifications (SHH α 3/37, β 0/23, γ 0/29, δ 0/48; p = 0.04 Pearson's chi-square test, Figure S4C; Table S4) are also enriched in SHH α. The recent WHO classification includes SHH-activated *TP53* mutant tumors as a distinct category based on studies showing this group as being very high risk (Louis et al., 2016; Ramaswamy et al., 2016a; Zhukova et al., 2013). To further explore this association, *TP53* was sequenced across 145 SHH samples. *TP53* mutations are highly enriched in SHH α (SHH α 14/40, β 2/27, γ 2/31, δ 6/47; p = 0.0026 Pearson's chi-square test, Figure 3E; Table S5). When survival is analyzed stratified by *TP53* mutation and SHH α subtype, *TP53* mutations are only prognostic in SHH α (HR *TP53* mut versus WT: SHH α 6.006 [95% CI: 1.586–22.75; p = 0.00832] and non-SHH α 1.222 [95% CI: 0.2795–5.342; p = 0.79, Cox proportional hazards, Figure 3F]).

Interestingly, infant SHH tumors are mainly distributed across SHH β and SHH γ (age < 3: SHH α 5/65, β 23/35, γ 34/47, δ 0/76; $p = 2.2 \times 10^{-16}$ Pearson's chi-square test, Figure 3B), with disparate outcomes and copy-number profiles. SHH β tumors are frequently metastatic (33.3% versus 9.4% in SHH β and γ; p = 0.027 Pearson's chi-square test, Figure 3G), harbor focal *PTEN* deletions (25% in SHH β versus none in γ), have multiple focal amplifications (Figure S4C; Table S4), and have a worse overall survival compared with SHH γ (HR of SHH β versus γ: 2.956 95% CI: 0.908–9.63; p = 0.059 Cox proportional hazards, Figure 3C). The difference in outcomes between SHH β and γ is possibly related to the increased rate of metastatic dissemination in SHH β, as there is a clear trend toward metastases being a marker of poor outcome within SHH β (HR of SHH β metastatic versus non-metastatic: 3.621 95% CI: 0.798–16.44; p = 0.096 Cox proportional hazards). Conversely, SHH γ have a relatively quiet copy-number landscape, with no recurrent amplifications, only one low-level recurrent focal deletion, and no significant arm-level gains (Figures 3D and S4C). Moreover, SHH γ are enriched for the MBEN (medulloblastoma with extensive nodularity) histology (20.9%; $p = 2.34 \times 10^{-5}$, Pearson's chi-square test, Figure 3H), which is known to portend more indolent clinical behavior (Rutkowski et al., 2010). Although almost all SHH tumors with MBEN histology (n = 10) were assigned to it,

(H) WHO histological classification at diagnosis across the four SHH subtypes (chi-square test).
(I) Overall survival within SHH γ stratified by MBEN histology (log rank test). + indicates censored cases.
(J) Distribution of *TERT* promoter mutations across SHH subtypes (Pearson's chi-square test).
See also Figures S4, S5; Tables S2, S4, and S5.

only a minority of SHH γ tumors have MBEN histology, demonstrating that histology alone is an inadequate surrogate to identify SHH γ tumors. The survival difference of SHH γ patients is not statistically significant between MBEN and non-MBEN tumors, suggesting that subtype affiliation is a more powerful biomarker than histopathology in infants with SHH medulloblastoma ($p = 0.268$, log rank test, Figure 3I). SHH δ are primarily composed of adults, have a favorable prognosis, and are strongly enriched for *TERT* promoter mutations (SHH α 6/34, β 2/22, γ 7/26, δ 38/42; $p = 8.13 \times 10^{-13}$, Pearson's chi-square test, Figure 3J).

To interrogate other possible solutions and to present the full results (Figures S5A–S5E), we also compared SHH subtypes when divided into three or five SNF groups. We refer to the clusters obtained by SNF for other numbers of groups ($k = 3$, $k = 5$ here) as c1, c2, c3, etc. (see Figures S4A and S4B). When comparing $k = 4$ with $k = 3$, SHH α and δ correspond closely to c2 and c1, respectively, with c3 representing a group of infants comprising SHH β and γ (Figures S4A, S4B, and S5A). SHH $k = 5$ reveals an additional group comprised primarily of a subset of SHH α patients with a group (c3) enriched for 9q loss with a good prognosis and a second group (c5) with a poor prognosis enriched for anaplasia (Figures S4B and S5C–S5E). Several machine-learning classifiers using both data types suggest poor confidence (<80%) in predicting the c5 group. The machine-learning classifier with the best performance, elastic net (Zou and Hastie, 2005), is able to distinguish between four groups with >90% accuracy (Table S2). The identification of two groups of infant medulloblastoma with distinct clinical behavior allows for more precise and rational planning of clinical trials for infants with SHH medulloblastoma (Lafay-Cousin et al., 2016).

WNT Subtypes

We identify two WNT subtypes, WNT α ($n = 49$) and WNT β ($n = 21$) (Figures 4A, S6A, and S6B); WNT α is comprised mainly of children (Figure 4B), has similar survival as WNT β ($p = 0.5$, log rank test, Figure 4C), and has ubiquitous monosomy 6 (WNT α 48/49, β 6/21; $p = 2.365 \times 10^{-10}$ Pearson's chi-square test, Figure 4D). WNT β is enriched for older patients ($p = 4.013 \times 10^{-6}$, Kruskal-Wallis test, Figure 4B) who are frequently diploid for chromosome 6 (Figure 4D). Monosomy 6 has previously been described as a defining WNT medulloblastoma feature; clearly, patients with WNT β will be misdiagnosed if this criterion is used alone. Prior reports suggesting that adult WNT medulloblastoma might have a different biology and worse prognosis than childhood WNT medulloblastoma, are supported by our current analysis (Remke et al., 2011; Zhao et al., 2016). At $k = 3$, we observe a new group, comprised primarily of WNT β without monosomy 6 (Figures S6A and S6B); however, in the absence of any other defining feature or clear clinical relevance, we chose $k = 2$ as our preferred solution.

Group 3 Subtypes

Three very distinct subtypes of group 3 emerge from our analysis, each with characteristic copy-number and clinical variables: group 3α ($n = 67$), group 3β ($n = 37$), and group 3γ ($n = 40$) (Figures 5A, S6C, and S6D). A total of 60% of infants under the age of 3 years are in group 3α (age < 3: group 3α 14/63, 3β 4/36, 3γ 5/36; $p = 0.021$, Kruskal-Wallis test, Figure 5B). Clinically, groups 3α and 3β have a more favorable prognosis compared with group 3γ (Figure 5C). Group 3β are slightly older ($p = 0.021$, Kruskal-Wallis test, Figure 5B), and are infrequently metastatic (group 3α 23/53, 3β 5/25, 3γ 15/30; $p = 0.058$ Pearson's chi-square test, Figure 5D). Group 3α and 3γ have a similar frequency of metastatic dissemination at diagnosis (Figure 5D). Chromosome 8q (*MYC* locus at 8q24) loss is more frequent in group 3α and gain more frequent in group 3γ (8q gain: group 3α 0/67, 3β 3/37, 3γ 22/40; $p = 2.2 \times 10^{-16}$ Pearson's chi-square test, Figure 5E), group 3β tumors have a higher frequency of activation of the *GFI1* and *GFI1B* oncogenes, previously shown to be drivers of group 3 through a process termed enhancer hijacking via focal gains and losses on chromosomes 1 and 9, with a paucity of arm-level chromosomal gains and losses (*GFI1* or *GFI1B* activation: group 3α 1/67, 3β 26/37, 3γ 3/40, $p < 2.2 \times 10^{-16}$ Pearson's chi-square test, Figures S7A and S7B) (Northcott et al., 2014). *OTX2* amplifications are also enriched in group 3β, as are losses of *DDX31* on chromosome 9; previously described to lead to activation of *GFI1B* through enhancer hijacking (*OTX2*: group 3α 0/35, 3β 6/28, 3γ 0/24; $p = 0.0013$; DDX31 deletion: group 3α 1/35, 3β 9/28, 3γ 0/24; $p = 0.0031$ Pearson's chi-square test, Figure S7A; Table S4). Group 3γ have the worst prognosis ($p = 0.036$ log rank test, Figure 5C), a trend to enrichment of i17q (group 3α 17/67, 3β 5/37, 3γ 10/40; $p = 0.32$ Pearson's chi-square test, Figure 5E) and frequently harbor increased *MYC* copy number (group 3α 0/35, 3β 2/28, 3γ 5/24; $p = 0.012$, Figures 5F and S7A; Table S4), without other focal aberrations (Taylor et al., 2012). Group 3γ have a poor prognosis independent of *MYC* amplification, expanding the group of high-risk group 3 tumors beyond just *MYC* status ($p = 0.026$, log rank test, Figure 5G).

We find less support for other solutions of group 3, specifically $k = 2$ and $k = 4$ (Figures S6C, S6D, S7C, and S7D). At $k = 2$, we observe a group enriched for *MYC* amplification (c1 0/38, c2 7/48; $p = 0.014$ Pearson's chi-square test), and *GFI1* family of oncogene activations cluster together (*GFI1/1B* activation: c1 1/71, c2 29/73; $p = 1.14 \times 10^{-8}$ Pearson's chi-square test) without any meaningful clinical differences (Figure S7C). At $k = 4$, group 3α splits into two groups with minor contributions from the other two groups without any new meaningful clinical or copy-number enrichment (Figures S6D and S7D). In addition the elastic net classifier performs strongly at $k = 3$ (89%–98.8% per-group accuracy), while at $k = 4$ one group is less reliably predicted (72% accuracy, Table S2).

Group 4 Subtypes

Group 4 is the most prevalent subgroup comprising >40% of all medulloblastomas; previously described features include i17q, tandem duplications of *SNCAIP*, and high-level amplifications of *MYCN* and *CDK6* (Northcott et al., 2012b). We observe clear enrichment of key focal and arm-level SCNA at $k = 3$: group 4α ($n = 98$), group 4β ($n = 109$), and group 4γ ($n = 119$) (Figures 6A, S8A, and S8B). Clinically we observe group 4β have a slightly higher median age at diagnosis (8.22, 10, and 7 years for groups 4α, 4β, and 4γ; $p = 1.34 \times 10^{-5}$ Pearson's chi-square test, Figure 6B); however, there is no statistically significant difference in the overall survival (Figure 6C) or rate of metastatic dissemination at diagnosis (groups 4α 30/75, 4β 35/86, 4γ 36/94; $p = 0.94$ Pearson's chi-square test, Figure 6D). Group 4α are

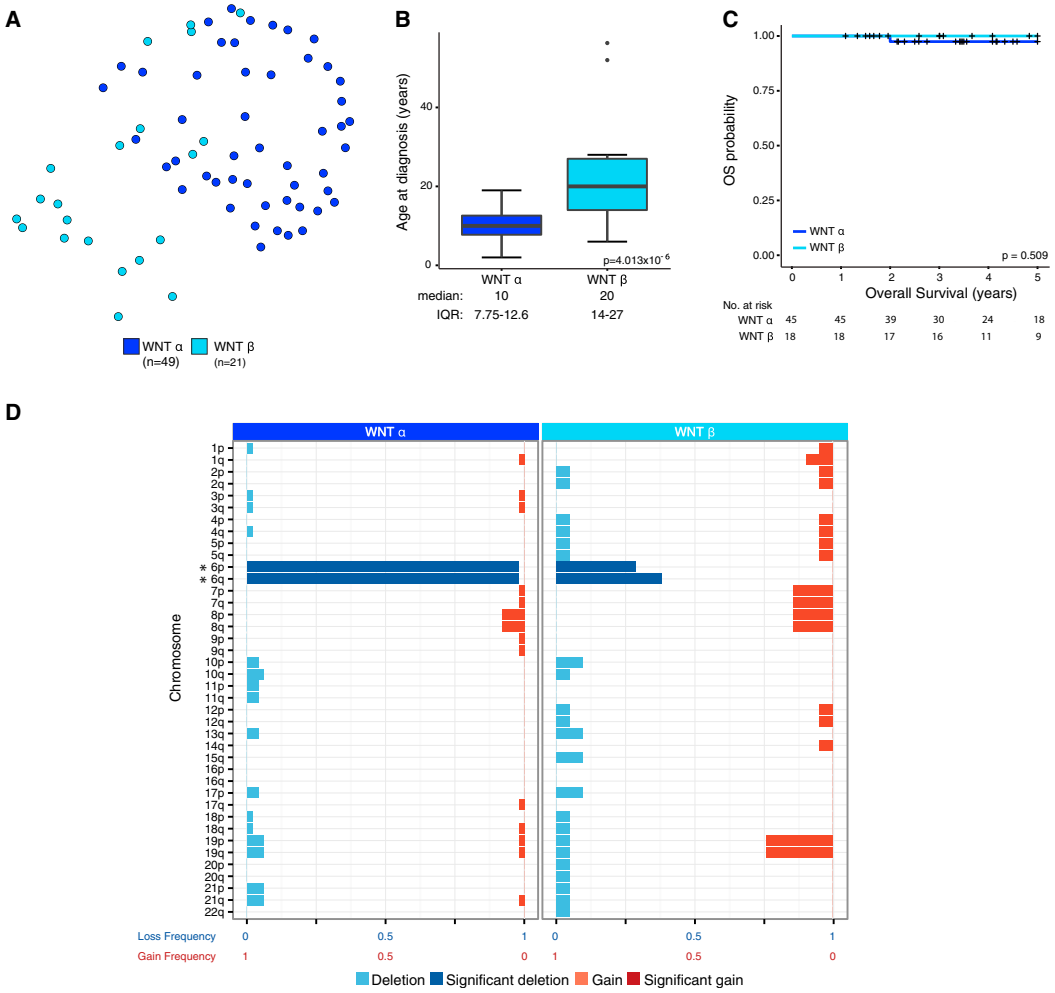

Figure 4. Clinical and Genomic Characteristics between Two WNT Medulloblastoma Subtypes

(A) Network representation map of k = 2 SNF-derived subtypes.

(B) Age at diagnosis for WNT subtypes at k = 2 (Mann-Whitney U test). Boxplot center lines show data median; box limits indicate the 25th and 75th percentiles; lower and upper whiskers extend 1.5 times the interquartile range (IQR) from the 25th and 75th percentiles, respectively. Outliers are represented by individual points.

(C) Overall survival comparing WNT α with WNT β (log rank test). + indicates censored cases.

(D) Frequency and significance of broad cytogenetic events across the two WNT subtypes. Darker bars show significant arm-level copy-number events ($q \leq 0.1$, chi-square test). * indicates key statistically significant arm gain or deletion.

See also Figure S6.

enriched for *MYCN* amplifications (11/66, compared with none in group 4β and 4γ; $p = 2.46 \times 10^{-6}$ Pearson's chi-square test, Figure S8C; Table S4). Group 4α and 4γ are strongly enriched for 8p loss (group 4α 47/98, 4β 24/109, 4γ 87/119; $p = 1.22 \times 10^{-13}$ Pearson's chi-square test) and 7q gain (group 4α 57/98, 4β 9/109, 4γ 62/119; $p = 9.5 \times 10^{-31}$, Pearson's chi-square test, Figure 6E). Group 4β are strongly enriched for *SNCAIP* duplications (group 4α 4/66, 4β 11/74, 4γ 0/73; p = 0.0019 Pearson's chi-square test) and almost ubiquitous i17q (group 4α 40/98, 4β 87/109, 4γ 31/119; $p = 9.75 \times 10^{-16}$ Pearson's chi-square test) with a paucity of other SCNA (Figures 6E and S8C; Table S4). In addition, groups 4α and 4γ are enriched for focal *CDK6* amplifications (group 4α 4/66, 4β 0/74, 4γ 6/73; p = 0.051 Pearson's chi-square test, Figure S8C; Table S4). Previous studies have suggested *GFI1* and *GFI1B* activation to be present in group 4, however we see GFI activation to be largely restricted to group 3β (Figure S8D).

At k = 2, we observe groups 4α and 4γ forming one group, and group 4β being largely preserved (Figures S8A, S8B, and S8E). At k = 4, group 4β continues to segregate from the other groups; however, no new groups emerge with any significant clinical or copy-number differences (Figures S8A, S8B, and S8F). Due to the enrichment of key SCNA at k = 3, we chose this as our preferred solution. Moreover, our classifier exhibits a decline in

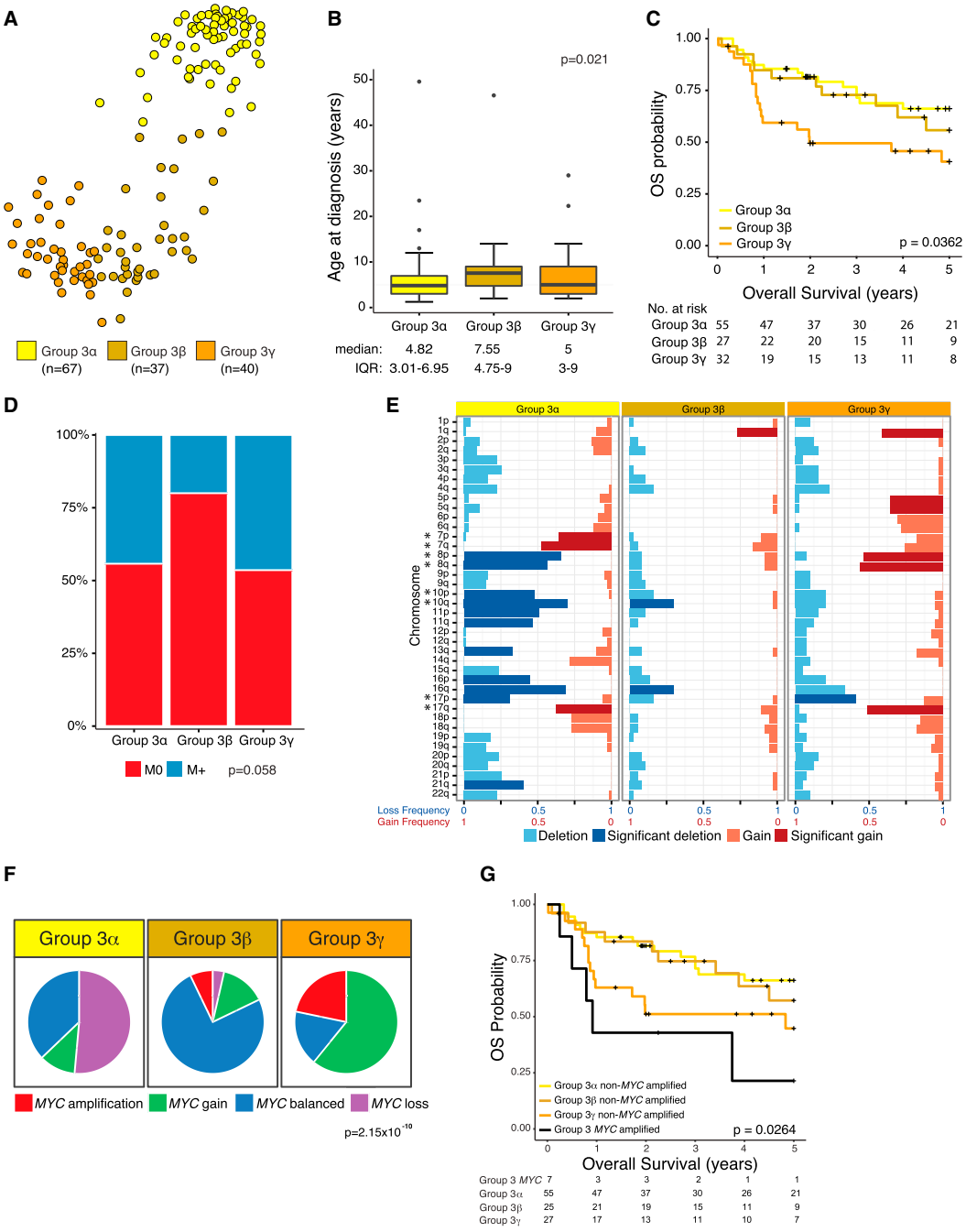

Figure 5. Clinical and Genomic Characteristics between Three Group 3 Medulloblastoma Subtypes

(A) Network representation map of k = 3 SNF-derived subtypes.

(B) Age at diagnosis of group 3 subtypes at k = 3 (Kruskal-Wallis test). Boxplot center lines show data median; box limits indicate the 25th and 75th percentiles; lower and upper whiskers extend 1.5 times the interquartile range (IQR) from the 25th and 75th percentiles, respectively. Outliers are represented by individual points.

(C) Overall survival of group 3 subtypes (log rank test). + indicates censored cases.

(D) Incidence of metastatic dissemination at diagnosis for the three group 3 subtypes (chi-square test).

(E) Frequency and significance of broad cytogenetic events across the group 3 subtypes. Darker bars show significant arm-level events ($q \leq 0.1$, chi-square test). * indicates key statistically significant arm gain or deletion.

(legend continued on next page)

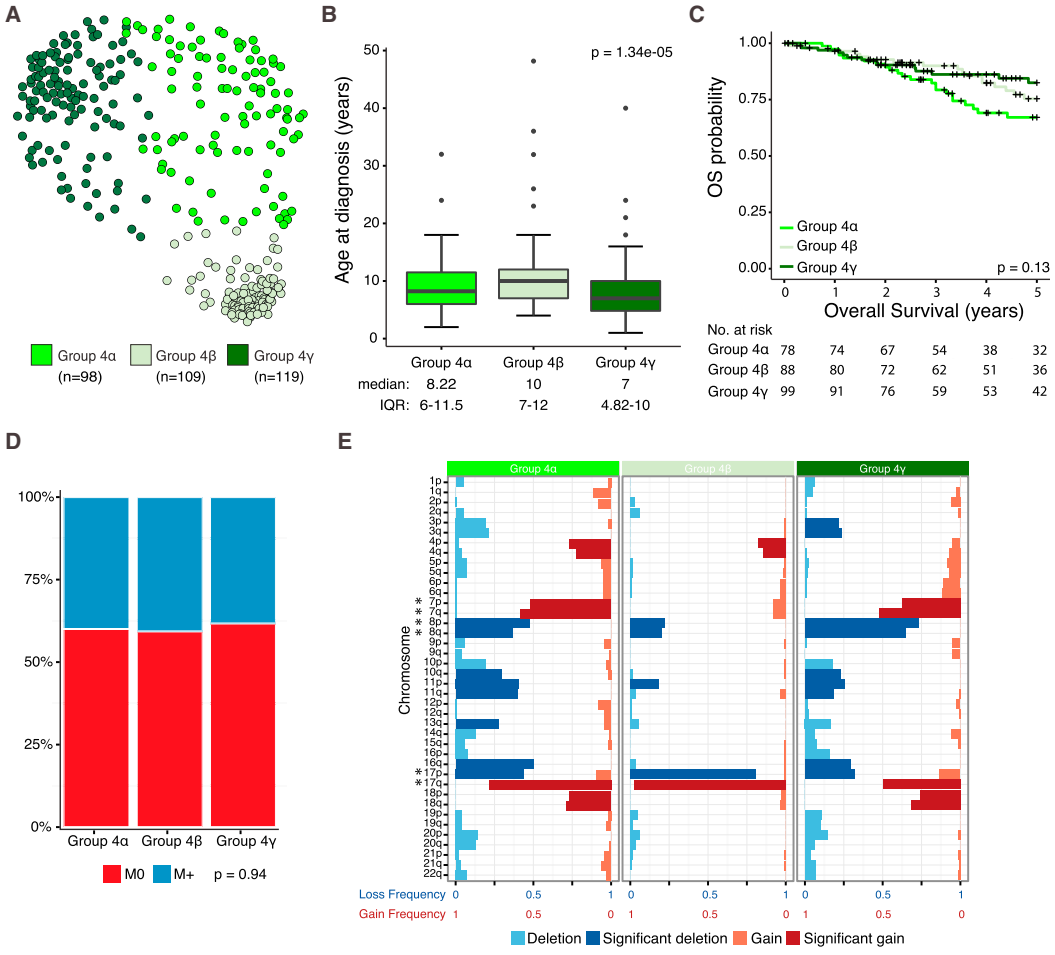

Figure 6. Clinical and Genomic Characteristics of the Three Group 4 Medulloblastoma Subtypes

(A) Network representation map of k = 3 SNF-derived subtypes.

(B) Age at diagnosis of group 4 subtypes at k = 3 (Kruskal-Wallis test). Boxplot center lines show data median; box limits indicate the 25th and 75th percentiles; lower and upper whiskers extend 1.5 times the interquartile range (IQR) from the 25th and 75th percentiles, respectively. Outliers are represented by individual points.

(C) Overall survival of group 4 subtypes (log rank test). + indicates censored cases.

(D) Incidence of metastatic dissemination at diagnosis across the three group 4 subtypes (chi-square test).

(E) Frequency and significance of broad cytogenetic events across the three group 4 subtypes. * indicates key statistically significant arm gain or deletion. Darker bars show significant arm-level events ($q \leq 0.1$, chi-square test).

See also Figure S8 and Tables S2, S4.

confidence at k = 4, suggesting these groups are not as robust as k = 3 (Table S2).

Comparable Subtypes with Key Clinical Differences Are Identified by Other Integrative Analyses

Two other integrative clustering methods have been employed by the The Cancer Genome Atlas (TCGA) consortium in previous studies of other cancer histologies. We applied both methods to our dataset; when applying the cluster of clusters (COCA) method used by TCGA in low-grade glioma and pan-cancer studies (Brat et al., 2015; Hoadley et al., 2014) we observed that the method was quite limited in the potential to leverage information from our two data types in the current manuscript. The COCA subgroups were driven by the samples that agree or disagree between the two data types clustered in isolation, which is the COCA input. COCA failed to identify one SHH infant subtype or group 3β.

(F) Distribution of *MYC* amplifications across group 3 subtypes (Pearson's chi-square test).

(G) Overall survival of group 3 subtypes without *MYC* amplifications for each subtype compared with *MYC*-amplified tumors (log rank test). + indicates censored cases.

See also Figures S6 and S7; Tables S2 and S4.

iCluster was used successfully by TCGA to identify relevant subtypes (Collisson et al., 2014). When applying iCluster to our dataset, at k = 4, the four groups did not have the demographics and SCNA consistent with the four previously described groups. When comparing the four iCluster groups with those defined by SNF, WNT and group 3 do not separate, and SHH comprises two groups. When we analyze the iCluster results for five groups, we recover two SHH groups, plus WNT, group 3, and group 4, which in this case corresponds very well to the SNF subgroup (when considering the two SHH groups together). We then asked if we could recover similar subtypes to SNF using iCluster. As we could not recover the four main groups, subgroups defined by SNF were then individually analyzed using iCluster. We observe a near 80% concordance with the SNF subtypes. The childhood and the adult SHH subtypes as well as the group 4 subtypes are recapitulated (along with a single SHH infant group). However, we identified key differences particularly within the WNT, SHH, and group 3 subgroups. Only one WNT group is identified, the two infant SHH subtypes are not identified, and the two distinct group 3 subtypes with *MYC* amplifications and *GFI1* activation are not observed. Clearly, the SNF method is superior at leveraging information of multiple datasets to identify meaningful groups of patients in a cancer cohort, specifically in a medulloblastoma cohort.

Differential Pathway Activation Defines Subtypes across All Four Medulloblastoma Subgroups

Pathway enrichment analysis was performed for each of the identified subtypes across all four subgroups using the top 10% of associated genes across each subtype. We observe several significantly enriched pathways for all identified subtypes (adj. p value < 0.05), supporting subtype-specific biological processes and transcriptional networks (Figures 7A–7D). In particular, in SHH we observe several pathways enriched in SHH β and γ, with developmental pathways more enriched in SHH γ over β (Figure 7A). Genes involved in DNA repair and cell cycle are significantly enriched in SHH α. Several actionable pathways, as defined by the availability of approved drugs, are subtype specific. Specifically, sumoylation is enriched in SHH α, ion channels are enriched in SHH β and γ, and telomere maintenance is enriched in SHH α and δ. Receptor tyrosine kinase signaling is enriched in SHH γ and, to a lesser extent, in β. DNA repair pathways are enriched in SHH α, suggesting that strategies to inhibit the DNA damage response and increase replicative stress are more likely to be effective in this group.

Group 3α tumors are enriched for photoreceptor, muscle contraction, and primary cilium-related genes (Figure 7B). Pathways involved in protein translation are enriched in groups 3β and 3γ, which are potentially actionable using modulators of protein synthesis such as proteasome inhibitors. Telomere maintenance is also more enriched in group 3γ, suggesting that telomerase inhibition may only be effective in one group. Several pathways are identified across group 4 subtypes, which, coupled with subtype-specific copy-number enrichment, further supports the existence of three group 4 subtypes (Figure 7C). Actionable pathways restricted to particular subtypes include MAPK and FGFR1 signaling in group 4β and PI3K-AKT signaling and ERBB4-mediated nuclear signaling in group 4γ. Cell migration pathways are more enriched in group 4α.

DISCUSSION

Our study identifies and delineates the intertumoral heterogeneity present within medulloblastoma subgroups. Leveraging a large cohort of medulloblastomas profiled by combined gene expression and DNA methylation, we have identified different subtypes within each of the four core subgroups. These subtypes have particular clinical and copy-number features, which allow for a refinement in our understanding of the genomic landscape of medulloblastoma (Figure 8). Combining expression and methylation data using SNF adds further proof that groups 3 and 4 are largely different biological entities. The deeper we go in clustering medulloblastoma samples, the less consistent the groups become. This is exemplified by poor predictability of putative subtypes when a large number of subtypes is assumed. Defining clinical features and CNAs also tend to lose their distinctive profiles as we increase the number of clusters, suggesting that heterogeneity is bounded by a discrete number of optimal groups.

Comparison of SNF with consensus clustering of either gene expression or DNA methylation data analyzed in isolation clearly suggests that an integrated approach provides a much more refined and accurate classification. This is particularly striking when evaluating the boundary between groups 3 and 4, where samples that are deemed indeterminate using gene expression and DNA methylation in isolation are largely non-overlapping. Moreover, in elucidating the heterogeneity within subgroups, we observe significant disagreement between gene expression and DNA methylation in isolation, suggesting that each data type makes a unique and non-redundant contribution to defining the subtypes. The very low number of samples that change subgroup affiliation using SNF strongly advocates that definition of these two groups is largely enhanced using an integrative approach. A limitation of our approach is the bulk analysis of samples. At a subclonal level, a greater degree of overlap across groups 3 and 4 cannot be discounted. More detailed analysis at a cellular level, specifically applying single-cell methods, will help delineate the full subclonal structure, potentially uncovering subsets of group 3 and 4 samples with common mechanisms and cellular origins. Further studies integrating emerging technologies such as long non-coding RNA, proteomics, and histone modifications may allow an even more refined description of the medulloblastoma landscape; however, the large cohorts of frozen tissue required for these studies are presently not available.

The identification of subtypes has significant biological and clinical implications. Several previously described copy-number alterations within medulloblastoma subgroups such as amplifications/gains of *MYC*, *MYCN*, *OTX2*, *CDK6*, *SNCAIP*, and *ACVR1*, as well as several arm-level events including i17q clearly segregate between subtypes (Northcott et al., 2012b). Our identification of unique cytogenetic aberrations that occur in concert, as well as specific biological pathways enriched within specific subtypes, will serve to inform creation of rational preclinical models that closely mirror the human diseases. Several of these aberrations are actionable and largely restricted to subtypes, which will also allow for a more personalized treatment approach. Several subtypes, particularly in SHH and group 3, have clear and drastic clinical and prognostic differences, which

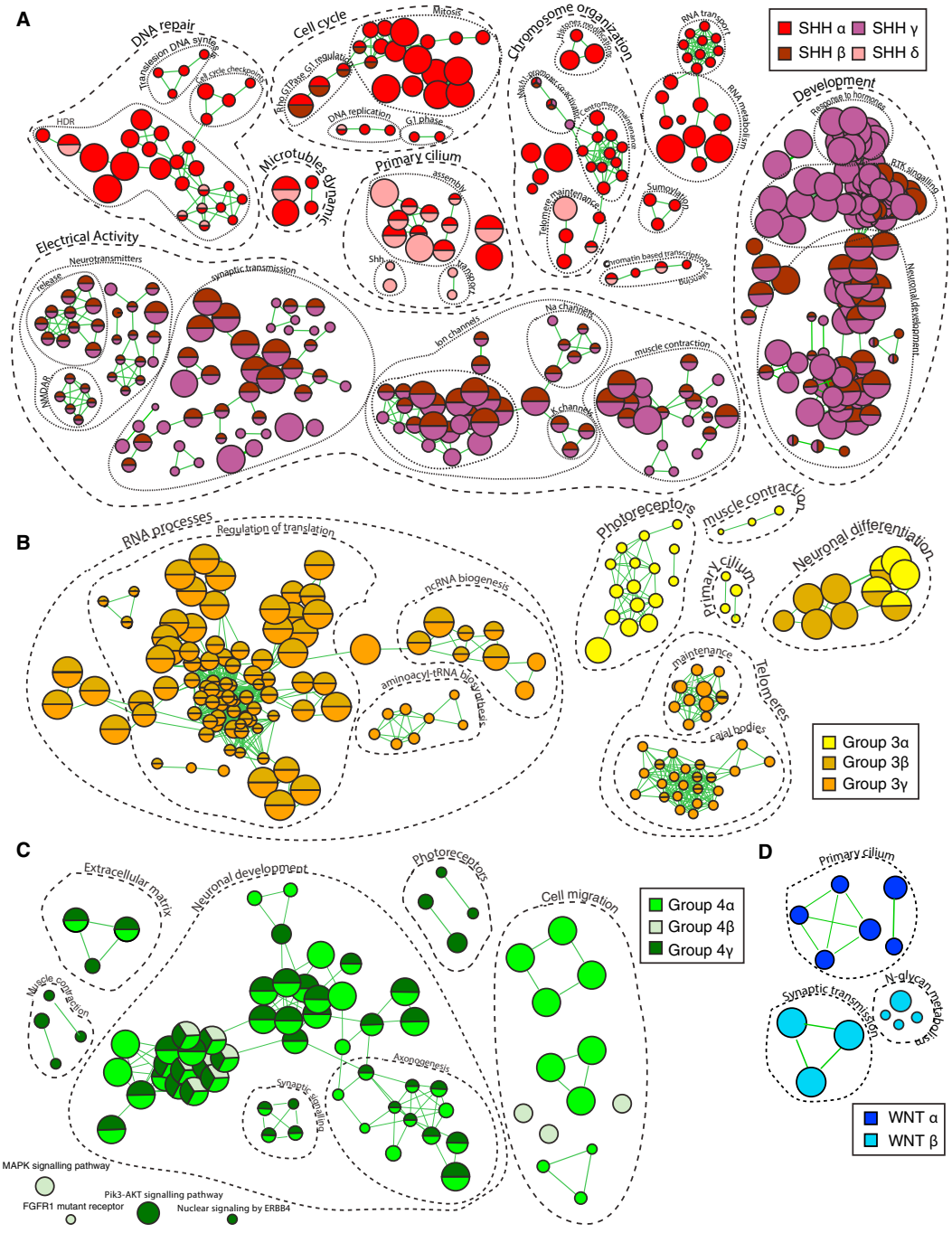

Figure 7. Subtype-Enriched Pathways

(A–D) Enrichment maps representing biological processes and pathways enriched in subtype-specific upregulated genes for SHH subtypes (A), group 3 subtypes (B), group 4 subtypes (C), and WNT subtypes (D). Each node represents a process or pathway; nodes with many shared genes are grouped and labeled by biological theme. Processes and pathways connected at edges have genes in common. Nodes are colored according to the subtype(s) in which the process is enriched; processes enriched in more than one subtype have multiple colors. Nodes sizes are proportional to the number of genes in each process, in each subgroup. Enriched processes were determined with g:Profiler (FDR-corrected q value < 0.05) and visualized with the Enrichment Map app in Cytoscape. Connected nodes and unconnected but actionable nodes are shown.

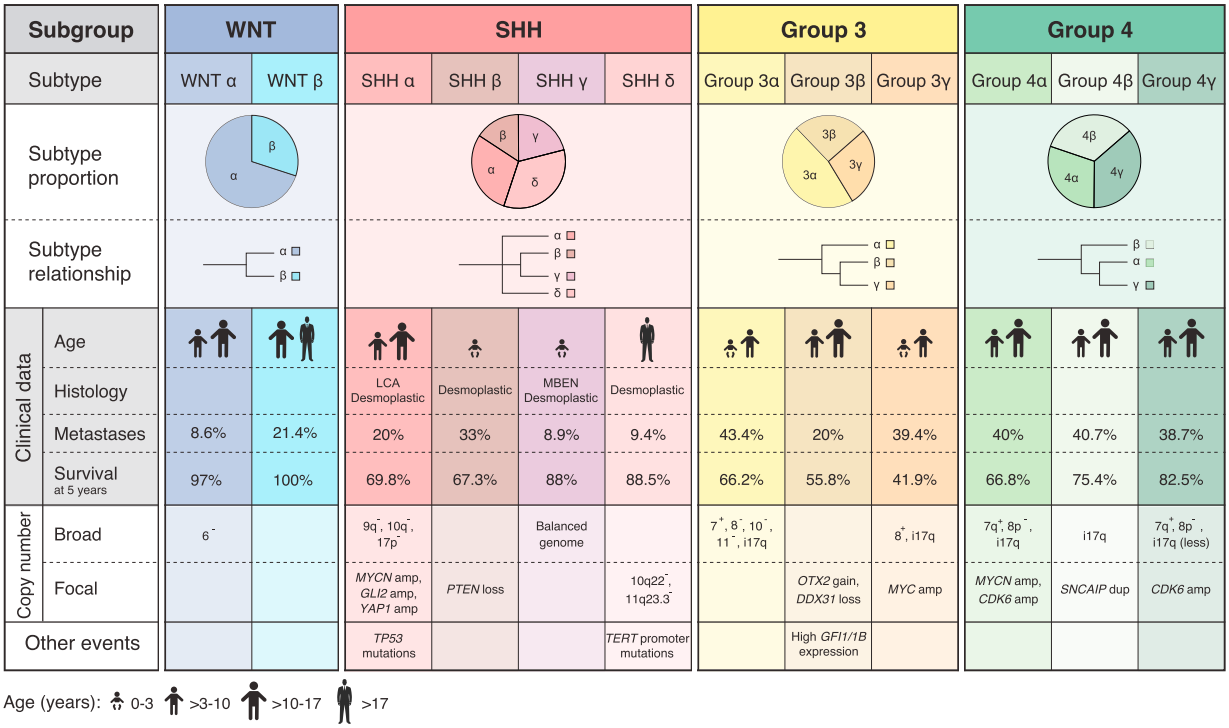

Figure 8. Graphical Summary of the 12 Medulloblastoma Subtypes

Schematic representation of key clinical data, copy-number events, and relationship between the subtypes inside each of the four medulloblastoma subgroups. The percentages of patients presenting with metastases and the 5-year survival percentages are presented. The age groups are: infant 0–3 years, child >3–10 years, adolescent >10–17 years, and adult >17 years.

will allow for more robust risk stratification in future clinical trials. Furthermore, a major hurdle to clinical trial design has been the overlap of groups 3 and 4 in current studies, which if applied today would make strata assignment difficult. The next generation of clinical trials for high-risk medulloblastoma will involve subgroup-specific therapies. The inability to stratify 10% of patients to either groups 3 or 4 has the potential to either deprive a patient of an innovative therapy or, of more concern, expose a child to an inappropriate escalation or de-escalation of therapy.

Clinically, our observed groups have immediate implications. It has been shown that *TP53* mutations are highly prognostic in SHH. We extend these findings whereby *TP53* mutations are not only enriched in SHH α but also only prognostic in SHH α. This is highly relevant for clinical trial design, where *TP53* mutant SHH has been identified as a very-high-risk group to be prioritized for novel therapies in both Europe and North America (Ramaswamy et al., 2016a); clearly, the observation that *TP53* mutations are highly enriched and prognostic in SHH α has significant implications. A limitation of this is the absence of germline status, which, based on previous studies, are likely *TP53* mutant enriched in SHH α.

The identification of two infant SHH groups has clear and immediate clinical significance. Currently, infant medulloblastomas are stratified by the presence or absence of desmoplastic morphology. However, several reports have suggested that infant SHH as a whole have a favorable prognosis independent of morphology. Our results suggest that clinical risk stratification can be refined by incorporation of integrated subtypes, whereby SHH γ are clearly a very low-risk group and could be spared the toxic effects of high-dose chemotherapy. Our observation that MBEN histology is almost exclusive to SHH γ, but represent a minority of cases within SHH γ, has significant implications for clinical trials. Current infant clinical trials stratify patients based on either classic or desmoplastic/MBEN histology. Indeed, the frequency of desmoplastic histology is similar across all four SHH subtypes, despite significant differences in survival between SHH subtypes. The most recent infant medulloblastoma study from the Children's Oncology Group ACNS1221 (NCT02017964) was closed prematurely due to an excess of relapses. This study selected infants with a "desmoplastic" morphology for treatment de-escalation, of which the vast majority are SHH. Indeed, our identification of two infant subtypes of SHH represents an example where more robust risk stratification has the potential to accurately select patients for de-escalation of therapy in future clinical trials. Overall, this further supports the idea that the incorporation of molecular stratification rather than subjective morphology alone has the potential for immediate clinical benefit.

Similarly, for group 3, we identify a high-risk group that is enriched for *MYC* amplification, but for which not all patients are *MYC* amplified. Interestingly, the majority of in vitro cell lines of

medulloblastoma do not represent the clear intertumoral heterogeneity, but rather are *MYC*-amplified or *MYC*-activated models that actually represent only group 3γ. The identification of significant heterogeneity across group 3 underlies the urgent need to develop preclinical models that faithfully recapitulate the different subtypes within each subgroup. In group 4, there are currently no robust preclinical models, and the subgroups we describe, specifically the mutually exclusivity of *MYCN* amplifications and *SNCAIP* duplications, may help with future modeling.

Taken together, our results highlight the power of combining multiple data types compared with the use of single data types in isolation. This approach has identified that there may be a limit to the degree of substructure across medulloblastoma samples; however, only a study with a much larger cohort could fully assess the extent of intertumoral heterogeneity within the subgroups. We identify clinically important substructure within subgroups, which will allow further refinement of our biological and clinical risk stratification schemes. The identification of homogeneous subtypes may simplify the identification of targets for therapy, and could allow for therapies effective across subtypes. The development of reliable biomarkers to identify subtypes will provide much needed prognostic information for patient stratification, particularly in regard to SHH and group 3 medulloblastoma.

STAR★METHODS

Detailed methods are provided in the online version of this paper and include the following:

- KEY RESOURCES TABLE
- CONTACT FOR REAGENT AND RESOURCE SHARING
- EXPERIMENTAL MODEL AND SUBJECT DETAILS
  - Acquisition of Patient Samples
- METHOD DETAILS
  - Nucleic Acid Extraction
  - Expression and Methylation Data
  - *TERT* Promoter and *TP53* Sequencing
- QUANTIFICATION AND STATISTICAL ANALYSIS
  - Microarray Gene Expression Analysis
  - Genome Wide Methylation Analysis
  - Methylation Array Copy Number Analysis
  - SNP6 Copy Number Analysis
  - Clinical Correlation and Survival Analysis
  - Group 3 and Group 4 Analysis
  - Similarity Network Fusion Analysis (SNF)
  - Groups Visualization Using Stratomex
  - Network Visualization with Cytoscape
  - Relationship between Associated Genes and Probes
  - Pathway Enrichment Analysis
  - Classifier Description
  - Training and Selection of the Classifiers
  - COCA Analysis
  - iCluster Analysis
- DATA AND SOFTWARE AVAILABILITY

SUPPLEMENTAL INFORMATION

Supplemental Information includes eight figures and five tables and can be found with this article online at http://dx.doi.org/10.1016/j.ccell.2017.05.005.

AUTHOR CONTRIBUTIONS

Conceptualization, F.M.G.C., M.R., V.R., and M.D.T.; Methodology, F.M.G.C., M.R., L.R., D.J.H.S., B.L., J.T., A.S.Mor., S.Ag., E.B., and V.R.; Investigation, F.M.G.C., M.R., L.R., J.P., L.G., C.N., A.S.Mor., Y.Y.T., C.M.K., H.F., K.I., and J.R.; Data Curation, F.M.G.C., B.L., A.S.Mor., H.F., and V.R.; Formal Analysis: F.M.G.C., L.R., D.J.H.S., L.G., J.R., and V.R.; Validation, F.M.G.C., L.R., V.R., and A.G., Writing – Original Draft, F.M.G.C., V.R., and M.D.T.; Writing – Review & Editing, F.M.G.C., C.D., J.R., A.G., V.R., and M.D.T.; Resources, B.-K.C., S.-K.K., K.-C.W., J.Y.L., W.A.G., M.P.-P., A.V., C.F.-C., A.J., C.G., A.A.N.R., K.K.W.L., H.-K.N., C.G.E., I.F.P., R.L.H., G.Y.G., J.M.O., S.L., W.A.W., B.L., L.B.C., R.C.T., M.K.C., R.V., P.H., M.-L.C.v.V., J.M.K., P.J.F., Y.S.R., T.K., E.L.-A., K.Z., J.S., G.F., M.M., E.G.v.M., S.O., T.S., A.K., M.Z., J.R.L., J.B.R., N.J., S.Al., J.M., T.E.v.M., S.J., A.S.Moo., A.R.H., J.A.C., D.P.C.T., C.G.C, M.F., J.P., C.C.F., A.G.S., L.M., L.M.L., H.W., H.N., S.K.E., M.P.-D., F.C.P.d.L, S.R., M.Z., A.L., A.H., C.E.H., U.T., E.B., U.B., P.B.D., and J.T.R., Project Administration, A.G., V.R., and M.D.T.; Supervision, G.D.B., A.G., V.R., and M.D.T.; Funding Acquisition, V.R. and M.D.T.

ACKNOWLEDGMENTS

M.D.T. is supported by funds from the Garron Family Chair in Childhood Cancer Research at The Hospital for Sick Children and The University of Toronto, and operating funds from the NIH (R01CA159859 and R01CA148699), The Terry Fox Research Institute, The Brain Tumor Foundation of Canada, The McLaughlin Center, Worldwide Cancer Research, The Canadian Institutes of Health Research, and the Pediatric Brain Tumor Foundation. M.D.T. is also supported by a Stand Up To Cancer - St. Baldrick's Pediatric Dream Team Translational Research Grant (SU2C-AACR-DT1113). Stand Up To Cancer is a program of the Entertainment Industry Foundation administered by the American Association for Cancer Research. V.R. is supported by Meagan's Walk, an Alex's Lemonade Stand Young Investigator Award, a Garron Family Cancer Center Pitblado Discovery Grant, and a Collaborative Ependymoma Research Network basic science fellowship. V.R. and M.D.T are supported by the Swifty Foundation. F.M.G.C. is supported by the Stephen Buttrum Brain Tumor Research Fellowship, granted by Brain Tumor Foundation of Canada. M.R. is supported by a fellowship from the Mildred Scheel Cancer Foundation and operating funds from the Pediatric Brain Tumor Foundation. J.R. and K.I. were supported by NSERC Discovery Grant RGPIN-2016-06485. J.R. was supported by Operating Grant 21089 of the Cancer Research Society. A.K. was supported by the Hungarian Brain Research Program (grant no. KTIA_13_NAP-A-V/3), the TÁMOP-4.2.2.A-11/1/KONV-2012-0025 project, and the János Bolyai Scholarship of the Hungarian Academy of Sciences. K.Z. acknowledges research support from the project OPVK CZ.1.07/2.3.00/20.0183. E.V.M. is funded by St. Baldrick's Foundation, and NIH R01 NS084063. We thank Susan Archer for technical writing.

Received: September 23, 2016
Revised: March 24, 2017
Accepted: May 8, 2017
Published: June 12, 2017

REFERENCES

Aryee, M.J., Jaffe, A.E., Corrada-Bravo, H., Ladd-Acosta, C., Feinberg, A.P., Hansen, K.D., and Irizarry, R.A. (2014). Minfi: a flexible and comprehensive Bioconductor package for the analysis of Infinium DNA Methylation microarrays. Bioinformatics *30*, 1363–1369.

Brat, D.J., Verhaak, R.G., Aldape, K.D., Yung, W.K., Salama, S.R., Cooper, L.A., Rheinbay, E., Miller, C.R., Vitucci, M., Morozova, O., et al. (2015). Comprehensive, integrative genomic analysis of diffuse lower-grade gliomas. N. Engl. J. Med. *372*, 2481–2498.

Cho, Y.-J., Tsherniak, A., Tamayo, P., Santagata, S., Ligon, A., Greulich, H., Berhoukim, R., Amani, V., Goumnerova, L., Eberhart, C.G., et al. (2011). Integrative genomic analysis of medulloblastoma identifies a molecular subgroup that drives poor clinical outcome. J. Clin. Oncol. *29*, 1424–1430.

Collisson, E.A., Campbell, J.D., Brooks, A.N., Berger, A.H., Lee, W., Chmielecki, J., Beer, D.G., Cope, L., Creighton, C.J., Danilova, L., et al. (2014). Comprehensive molecular profiling of lung adenocarcinoma. Nature *511*, 543–550.

Dai, M., Wang, P., Boyd, A.D., Kostov, G., Athey, B., Jones, E.G., Bunney, W.E., Myers, R.M., Speed, T.P., Akil, H., et al. (2005). Evolving gene/transcript definitions significantly alter the interpretation of genechip data. Nucleic Acids Res. *33*, e175.

Gaujoux, R., and Seoighe, C. (2010). A flexible R package for nonnegative matrix factorization. BMC Bioinformatics *11*, 367.

Gautier, L., Cope, L., Bolstad, B.M., and Irizarry, R.A. (2004). affy — analysis of Affymetrix GeneChip data at the probe level. Bioinformatics *20*, 307–315.

Gevaert, O. (2015). MethylMix: an R package for identifying DNA methylation-driven genes. Bioinformatics *31*, 1839–1841.

Hovestadt, V., Remke, M., Kool, M., Pietsch, T., Northcott, P.A., Fischer, R., Cavalli, F.M., Ramaswamy, V., Zapatka, M., Reifenberger, G., et al. (2013). Robust molecular subgrouping and copy-number profiling of medulloblastoma from small amounts of archival tumour material using high-density DNA methylation arrays. Acta Neuropathol. *125*, 913–916.

Hoadley, K.A., Yau, C., Wolf, D.M., Cherniack, A.D., Tamborero, D., Ng, S., Leiserson, M.D., Niu, B., McLellan, M.D., Uzunangelov, V., et al. (2014). Multiplatform analysis of 12 cancer types reveals molecular classification within and across tissues of origin. Cell *158*, 929–944.

Kauffmann, A., Gentleman, R., and Huber, W. (2009). arrayQualityMetrics – a bioconductor package for quality assessment of microarray data. Bioinformatics *25*, 415–416.

Kool, M., Jones, D.T., Jager, N., Northcott, P.A., Pugh, T.J., Hovestadt, V., Piro, R.M., Esparza, L.A., Markant, S.L., Remke, M., et al. (2014). Genome sequencing of SHH medulloblastoma predicts genotype-related response to smoothened inhibition. Cancer Cell *25*, 393–405.

Lafay-Cousin, L., Smith, A., Chi, S.N., Wells, E., Madden, J., Margol, A., Ramaswamy, V., Finlay, J., Taylor, M.D., Dhall, G., et al. (2016). Clinical, pathological, and molecular characterization of infant medulloblastomas treated with sequential high-dose chemotherapy. Pediatr. Blood Cancer *63*, 1527–1534.

Lex, A., Streit, M., Schulz, H.-J., Partl, C., Schmalstieg, D., Park, P.J., and Gehlenborg, N. (2012). StratomeX: visual analysis of large-scale heterogeneous genomics data for cancer subtype characterization. Computer Graphics Forum *31*, 1175–1184.

Louis, D.N., Perry, A., Reifenberger, G., von Deimling, A., Figarella-Branger, D., Cavenee, W.K., Ohgaki, H., Wiestler, O.D., Kleihues, P., and Ellison, D.W. (2016). The 2016 World Health Organization classification of tumors of the central nervous system: a summary. Acta Neuropathol. *131*, 803–820.

Maksimovic, J., Gordon, L., and Oshlack, A. (2012). SWAN: subset-quantile within array normalization for Illumina Infinium HumanMethylation450 BeadChips. Genome Biol. *13*, R44.

Merico, D., Isserlin, R., Stueker, O., Emili, A., and Bader, G.D. (2010). Enrichment map: a network-based method for gene-set enrichment visualization and interpretation. PLoS One *5*, e13984.

Mermel, C.H., Schumacher, S.E., Hill, B., Meyerson, M.L., Beroukhim, R., and Getz, G. (2011). GISTIC2.0 facilitates sensitive and confident localization of the targets of focal somatic copy-number alteration in human cancers. Genome Biol. *12*, R41.

Mo, Q., Wang, S., Seshan, V.E., Olshen, A.B., Schultz, N., Sander, C., Powers, R.S., Ladanyi, M., and Shen, R. (2013). Pattern discovery and cancer gene identification in integrated cancer genomic data. Proc. Natl. Acad. Sci. USA *110*, 4245–4250.

Morrissy, A.S., Garzia, L., Shih, D.J., Zuyderduyn, S., Huang, X., Skowron, P., Remke, M., Cavalli, F.M., Ramaswamy, V., Lindsay, P.E., et al. (2016). Divergent clonal selection dominates medulloblastoma at recurrence. Nature *529*, 351–357.

Northcott, P.A., Hielscher, T., Dubuc, A., Mack, S., Shih, D., Remke, M., Al-Halabi, H., Albrecht, S., Jabado, N., Eberhart, C.G., et al. (2011). Pediatric and adult sonic hedgehog medulloblastomas are clinically and molecularly distinct. Acta Neuropathol. *122*, 231–240.

Northcott, P.A., Jones, D.T., Kool, M., Robinson, G.W., Gilbertson, R.J., Cho, Y.J., Pomeroy, S.L., Korshunov, A., Lichter, P., Taylor, M.D., and Pfister, S.M. (2012a). Medulloblastomics: the end of the beginning. Nat. Rev. Cancer *12*, 818–834.

Northcott, P.A., Shih, D.J., Peacock, J., Garzia, L., Morrissy, A.S., Zichner, T., Stutz, A.M., Korshunov, A., Reimand, J., Schumacher, S.E., et al. (2012b). Subgroup-specific structural variation across 1,000 medulloblastoma genomes. Nature *488*, 49–56.

Northcott, P.A., Lee, C., Zichner, T., Stutz, A.M., Erkek, S., Kawauchi, D., Shih, D.J., Hovestadt, V., Zapatka, M., Sturm, D., et al. (2014). Enhancer hijacking activates GFI1 family oncogenes in medulloblastoma. Nature *511*, 428–434.

Pei, Y., Liu, K.W., Wang, J., Garancher, A., Tao, R., Esparza, L.A., Maier, D.L., Udaka, Y.T., Murad, N., Morrissy, S., et al. (2016). HDAC and PI3K antagonists cooperate to inhibit growth of MYC-driven medulloblastoma. Cancer Cell *29*, 311–323.

Ramaswamy, V., Northcott, P.A., and Taylor, M.D. (2011). FISH and chips: the recipe for improved prognostication and outcomes for children with medulloblastoma. Cancer Genet. *204*, 577–588.

Ramaswamy, V., Remke, M., Bouffet, E., Faria, C.C., Perreault, S., Cho, Y.J., Shih, D.J., Luu, B., Dubuc, A.M., Northcott, P.A., et al. (2013). Recurrence patterns across medulloblastoma subgroups: an integrated clinical and molecular analysis. Lancet Oncol. *14*, 1200–1207.

Ramaswamy, V., Remke, M., Bouffet, E., Bailey, S., Clifford, S.C., Doz, F., Kool, M., Dufour, C., Vassal, G., Milde, T., et al. (2016a). Risk stratification of childhood medulloblastoma in the molecular era: the current consensus. Acta Neuropathol. *131*, 821–831.

Ramaswamy, V., Remke, M., Adamski, J., Bartels, U., Tabori, U., Wang, X., Huang, A., Hawkins, C., Mabbott, D., Laperriere, N., et al. (2016b). Medulloblastoma subgroup-specific outcomes in irradiated children: who are the true high-risk patients? Neuro Oncol. *18*, 291–297.

Reimand, J., Arak, T., Adler, P., Kolberg, L., Reisberg, S., Peterson, H., and Vilo, J. (2016). g:Profiler – a web server for functional interpretation of gene lists (2016 update). Nucleic Acids Res. *44*, W83–W89.

Remke, M., Hielscher, T., Northcott, P.A., Witt, H., Ryzhova, M., Wittmann, A., Benner, A., von Deimling, A., Scheurlen, W., Perry, A., et al. (2011). Adult medulloblastoma comprises three major molecular variants. J. Clin. Oncol. *29*, 2717–2723.

Remke, M., Ramaswamy, V., Peacock, J., Shih, D.J., Koelsche, C., Northcott, P.A., Hill, N., Cavalli, F.M., Kool, M., Wang, X., et al. (2013). TERT promoter mutations are highly recurrent in SHH subgroup medulloblastoma. Acta Neuropathol. *126*, 917–929.

Rutkowski, S., Cohen, B., Finlay, J., Luksch, R., Ridola, V., Valteau-Couanet, D., Hara, J., Garre, M.-L., and Grill, J. (2010). Medulloblastoma in young children. Pediatr. Blood Cancer *54*, 635–637.

Shannon, P., Markiel, A., Ozier, O., Baliga, N.S., Wang, J.T., Ramage, D., Amin, N., Schwikowski, B., and Ideker, T. (2003). Cytoscape: a software environment for integrated models of biomolecular interaction networks. Genome Res. *13*, 2498–2504.

Shen, R., Olshen, A.B., and Ladanyi, M. (2009). Integrative clustering of multiple genomic data types using a joint latent variable model with application to breast and lung cancer subtype analysis. Bioinformatics *25*, 2906–2912.

Streit, M., Lex, A., Gratzl, S., Partl, C., Schmalstieg, D., Pfister, H., Park, P.J., and Gehlenborg, N. (2014). Guided visual exploration of genomic stratifications in cancer. Nat. Methods *11*, 884–885.

Sturm, D., Witt, H., Hovestadt, V., Khuong-Quang, D.A., Jones, D.T., Konermann, C., Pfaff, E., Tonjes, M., Sill, M., Bender, S., et al. (2012). Hotspot mutations in H3F3A and IDH1 define distinct epigenetic and biological subgroups of glioblastoma. Cancer Cell *22*, 425–437.

Taylor, M.D., Northcott, P.A., Korshunov, A., Remke, M., Cho, Y.J., Clifford, S.C., Eberhart, C.G., Parsons, D.W., Rutkowski, S., Gajjar, A., et al. (2012). Molecular subgroups of medulloblastoma: the current consensus. Acta Neuropathol. *123*, 465–472.

Thompson, E.M., Hielscher, T., Bouffet, E., Remke, M., Luu, B., Gururangan, S., McLendon, R.E., Bigner, D.D., Lipp, E.S., Perreault, S., et al. (2016). Prognostic value of medulloblastoma extent of resection after accounting for molecular subgroup: a retrospective integrated clinical and molecular analysis. Lancet Oncol. *17*, 484–495.

Wang, B., Mezlini, A.M., Demir, F., Fiume, M., Tu, Z., Brudno, M., Haibe-Kains, B., and Goldenberg, A. (2014). Similarity network fusion for aggregating data types on a genomic scale. Nat. Methods *11*, 333–337.

Wilkerson, D.M., and Hayes, D.N. (2010). ConsensusClusterPlus: a class discovery tool with confidence assessments and item tracking. Bioinformatics *26*, 1572–1573.

Zhao, F., Ohgaki, H., Xu, L., Giangaspero, F., Li, C., Li, P., Yang, Z., Wang, B., Wang, X., Wang, Z., et al. (2016). Molecular subgroups of adult medulloblastoma: a long-term single-institution study. Neuro Oncol. *18*, 982–990.

Zhou, W., Laird, P.W., and Shen, H. (2016). Comprehensive characterization, annotation and innovative use of Infinium DNA Methylation BeadChip probes. Nucleic Acids Res. *45*, e22.

Zhukova, N., Ramaswamy, V., Remke, M., Pfaff, E., Shih, D.J., Martin, D.C., Castelo-Branco, P., Baskin, B., Ray, P.N., Bouffet, E., et al. (2013). Subgroup-specific prognostic implications of TP53 mutation in medulloblastoma. J. Clin. Oncol. *31*, 2927–2935.

Zou, H., and Hastie, T. (2005). Regularization and variable selection via the elastic net. J. R. Stat. Soc. Ser. B *67*, 301–320.

STAR★METHODS

KEY RESOURCES TABLE

REAGENT or RESOURCE	SOURCE	IDENTIFIER
Biological Samples		
763 primary medulloblastoma samples	This paper	N/A
Deposited Data		
Expression and methylation array raw and analyzed data	This paper	GEO: GSE85218
Expression array data (285 samples) (included as well in GSE85218)	Northcott et al., 2012b	GEO: GSE37382
SNP6 data	Northcott et al., 2012b	GEO: GSE37384
Oligonucleotides		
Primer for P53 see Table S5	Zhukova et al., 2013	N/A
TERT forward primer, 5′-CAG CGC TGC CTG AAA CTC-3′	Remke et al., 2013	N/A
TERT reverse primer, 5′-GTC CTG CCC CTT CAC CTT C-3′	Remke et al., 2013	N/A
Software and Algorithms		
Affy R Biocondcutor package	Gautier et al., 2004	http://bioconductor.org/packages/release/bioc/html/affy.html
custom chip definition file (CDF) hugene11sthsensgcdf (v19.0.0).	Dai et al., 2005	http://brainarray.mbni.med.umich.edu/Brainarray/Database/CustomCDF/19.0.0/ensg.asp
arrayQualityMetrics R Bioconductor package (v3.22.0)	Kauffmann et al., 2009	https://www.bioconductor.org/packages/release/bioc/html/arrayQualityMetrics.html
minfi R Bioconductor package (v1.6.0) including SWAN normalization method	Aryee et al., 2014; Maksimovic et al., 2012	http://bioconductor.org/packages/release/bioc/html/minfi.html
NMF R package (v0.20.6)	Gaujoux and Seoighe, 2010	https://cran.r-project.org/web/packages/NMF/index.html
conumee R Bioconductor package (v0.99.4)	Hovestadt et al., 2013; Sturm et al., 2012	http://bioconductor.org/packages/release/bioc/html/conumee.html
GISTIC2 method (v6.2)	Mermel et al., 2011	http://portals.broadinstitute.org/cgi-bin/cancer/publications/pub_paper.cgi?mode=view&paper_id=216&p=t
ConsensusClusterPlus R Bioconductor package (v1.24.0)	Wilkerson and Hayes, 2010	https://www.bioconductor.org/packages/release/bioc/html/ConsensusClusterPlus.html
SNFtool R package (v2.2.0)	Wang et al., 2014	https://cran.r-project.org/web/packages/SNFtool/index.html
MethylMix R Bioconductor package (2.0.0)	Gevaert, 2015	https://www.bioconductor.org/packages/release/bioc/html/MethylMix.html
Infinium DNA Methylation BeadChip (450K) probe annotation on hg38	Zhou et al., 2016	http://zwdzwd.github.io/InfiniumAnnotation
StratomeX tool as part of the Caleydo suite (v3.1.5)	Streit et al., 2014; Lex et al., 2012	http://caleydo.org/tools/stratomex/
g:profiler	Reimand et al., 2016	http://biit.cs.ut.ee/gprofiler/
Cytoscape (v3.2.0)	Shannon et al., 2003	http://www.cytoscape.org/
Cytoscape Enrichment map	Merico et al., 2010	http://apps.cytoscape.org/apps/enrichmentmap
IClusterPlus R Bioconductor package (v1.10.0)	Mo et al., 2013	https://www.bioconductor.org/packages/release/bioc/html/iClusterPlus.html

CONTACT FOR REAGENT AND RESOURCE SHARING

Further information and requests for resources and reagents should be directed to and will be fulfilled by the Lead Contact, Michael D Taylor (mdtaylor@sickkids.ca).

EXPERIMENTAL MODEL AND SUBJECT DETAILS

Acquisition of Patient Samples

All medulloblastoma samples were collected at diagnosis after obtaining informed consent from subjects as part of the Medulloblastoma Advanced Genomics International Consortium. Approval was obtained from institutional research ethics boards at the following institutions: The Hospital for Sick Children, Children's Hospital of Pittsburgh, Seoul National University Children's Hospital, The Children's Memorial Health Institute, Institute of Pediatric Hematology and Oncology, Mayo Clinic, The Chinese University of Hong Kong, John Hopkins University School of Medicine, University of Alabama at Birmingham, Seattle Children's Hospital, University of California San Francisco, Burdenko Neurosurgical Institute, McMaster University, Erasmus University Medical Center, Asan Medical Center, Kitasato University School of Medicine, Hospital Pediatría Centro Médico Nacional Century XXI, Masaryk University, Fondazione IRCCS Istituto Nazionale Tumori, Emory University, Osaka National Hospital, University of Debrecen, University of Naples, Washington University School of Medicine, Montreal Children's Hospital, Hospital Sant Joan de Déu, Virginia Commonwealth University, Chonnam National University Hwasun Hospital and Medical School, Children's Health Queensland Hospital and Health Service, University of Calgary, University of Sao Paulo, Cincinnati Children's Hospital Medical Center, Hospital de Santa Maria, Lisbon, University of Arkansas for Medical Sciences, Catholic University Medical School, David Geffen School of Medicine at UCLA, The University of Sydney, Kumamoto University Graduate School of Medical Science, Saint Louis University School of Medicine, Hospital Infantil de Mexico Federico Gomez, Rainbow Babies & Children's Hospital. Patients were selected only if their treatment plan required surgical resection. Samples were obtained as fresh frozen tissue from the time of diagnosis and stored at -80°C until processed for the purification of nucleic acids. Tumor isolates were partitioned for both DNA and RNA extraction. Using all information in our hands, we selected only primary tumor medulloblastoma samples for this study and removed duplicates. The sex and gender of the 763 medulloblatoma patients used in this study are presented in Table S1.

METHOD DETAILS

Nucleic Acid Extraction

DNA extraction was performed by incubation with proteinase K overnight at 55°C followed by three sequential phenol extractions and ethanol precipitation. Total RNA was isolated using the TriZol method where tissue was homogenized in a Precellys 24 tissue homogenizer (Bertin Technologies, France) in Trizol using strict RNAase free conditions. DNA was quantified using the Picogreen method and RNA quantified using a NanoDrop 1000 instrument (Thermo Scientific) and integrity assessed by agarose gel electrophoresis (DNA) or Agilent 2100 Bioanalyzer (RNA) at the Centre for Applied Genomics (TCAG) at the Hospital for Sick Children in Toronto, Canada. RNA with an RNA integrity number of 7 or higher was required for analysis by Affymetrix Gene Arrays.

Expression and Methylation Data

To generate gene expression array profiling, 400ng of total RNA was processed and hybridized to the Affymetrix Gene 1.1 ST array at the Centre for Applied Genomics (TCAG) at the Hospital for Sick Children (Toronto, Canada) according to manufacturers instructions. In addition, all samples were analyzed on the Illumina Infinium HumanMethylation450 BeadChips at TCAG (Toronto, ON) according to manufacturer's instructions.

TERT Promoter and *TP53* Sequencing

TERT promoter mutational status was determined using direct sanger sequencing and genotyping as previously described where sufficient DNA was available (Remke et al., 2013). Two primers (forward primer, 5′-CAG CGC TGC CTG AAA CTC-3′; reverse primer, 5′-GTC CTG CCC CTT CAC CTT C-3′) were designed to amplify a 163-bp product encompassing C228T and C250T hotspot mutations in the *TERT* promoter—corresponding to the positions 124 and 146 bp, respectively, upstream of the ATG start site. Two fluorogenic LNA probes were designed with different fluorescent dyes to allow single-tube genotyping. One probe was targeted to the WT sequence (*TERT* WT, 5′-5HEX-CCC CTC CCG G-3IABkFQ-3′), and one was targeted to either of the two mutations (*TERT* mut, 5′-56FAM-CCC CTT CCG G-3IABkFQ). Primer and probes were custom designed by Integrated DNA Technologies (Coralville, Iowa, USA) using internal SNP design software, and sequence homogeneity was confirmed by comparison to all available sequences on the GenBank database using BLAST (). Primers were optimized to avoid for hairpins and homo- and heterodimers. Primers and probes were obtained from Integrated DNA Technologies.

Real-time PCR was performed in 25 μl reaction mixtures containing 12.5 μl of TaqMan Universal Master Mix II with UNG (Applied Biosystems), 900 nM concentrations of each primer, 250 nM *TERT* WT probe, 250 nM *TERT* MUT probe, and 1 μl (25 ng) of sample DNA. Thermocycling was performed on the StepOnePlus (Applied Biosystems) and consisted of 2 min at 50 °C, 10 min at 95 °C, and 40 cycles of 95 °C for 15 s and 60 °C for 1 min.

Analysis was performed using StepOne Software, version 2.1. Samples were considered mutant if they had CT values of $\leq$39 cycles. Each sample was verified visually by examining the PCR curves generated to eliminate false positives due to aberrant light emission. End-point allelic discrimination genotyping was performed by visually inspecting a plot of the fluorescence from the WT probe versus the MUT probe generated from the post-PCR fluorescence read.

TP53 mutational status was determined using direct sanger sequencing as previously described where sufficient DNA was available (Zhukova et al., 2013). We used amplitaq gold and after purification with ampure beads, forward and reverse sequencing primers using dGTP BigDye Terminator v3.0 Cycle Sequencing Ready Reaction Kit (Life Technologies), and 5 % DMSO on the ABI3730XL capillary genetic analyzer (Life Technologies). The sequencing primers are the same as the PCR primers. The *TP53* primers along with the melting temperature are presented in Table S5.

QUANTIFICATION AND STATISTICAL ANALYSIS

Microarray Gene Expression Analysis

To generate gene expression array profiling, 400ng of total RNA was processed and hybridized to the Affymetrix Gene 1.1 ST array at TCAG according to manufacturer's instructions. Two hundred and eighty-five arrays were previously generated (GEO accession GSE37382) and included in the analysis. Expression data were analyzed in the R environment (v3.1.1). We used the affy package (v1.44.0) (Gautier et al., 2004) and the custom chip definition file (CDF) hugene11sthsensgcdf (v19.0.0).

(http://brainarray.mbni.med.umich.edu/Brainarray/Database/CustomCDF/19.0.0/ensg.asp) (Dai et al., 2005) to load and summarize the expression of 21,641 Ensembl (ENSG) genes and process the data. Samples flagged by the arrayQualityMetrics Bioconductor package (v3.22.0) (Kauffmann et al., 2009) were removed due to low quality. Expression data were normalized using the rma method.

Unsupervised clustering using NMF using top 10,000 most variably expressed genes (determined by the standard deviation) was carried out using the NMF package (v0.20.6) (Gaujoux and Seoighe, 2010). We reselected the top most 10,000 variably expressed genes for each subset of samples on which we ran NMF.

Genome Wide Methylation Analysis

All samples were analyzed on the Illumina Infinium HumanMethylation450 BeadChips at TCAG (Toronto, Ontario) according to manufacturer's instructions. Bisulfite conversion was performed using the EZ DNA Methylation™ Kit (Zymo, Irvine, CA). Samples were processed as per manufacturer's instructions. Raw data files (.idat) generated by the Illumina iScan array scanner were processed in the R statistical environment (v3.0.0 and 3.1.1) using the minfi (v1.6.0) (Aryee et al., 2014) and IlluminaHumanMethylation450kmanifest (v0.4.0) R Bioconductor packages. We checked all samples for unexpected genotype matches by pairwise correlation of the 65 genotyping probes on the 450k arrays, allowing us to remove remaining duplicates. We ran the detectionP function from the minfi package to identify probes and samples with low quality. Samples were removed if more than 1% of their probes had a p value above 0.01 and probes were removed if their p value was above 0.01 in at least 5% of samples. We removed probes on sex chromosomes as well as those located on or close to known single nucleotide polymorphisms (SNP). We retained a total of 321,174 probes for the analysis. The data was normalized using the SWAN method as part of the minfi package (Maksimovic et al., 2012). We generated both the beta and logitB values matrix values. Unsupervised clustering using the top 10,000 most variably methylated probes defined by the standard deviation was carried out using the NMF package (v0.20.6). We reselected the top most 10,000 variably methylated probes for each subset of samples on which we ran NMF.

Methylation Array Copy Number Analysis

Copy number inference from methylation arrays and identification of recurrent broad events. Copy number segmentation was performed from genome wide methylation arrays using the conumee package (v0.99.4) in the R statistical environment (v3.2.3) as previously described (Hovestadt et al., 2013; Sturm et al., 2012). Segment files were generated for each subgroup and subtype.

Identification of recurrent broad copy number events (arm level chromosomal events) was performed from segmented copy number derived from methylation data (as described above). The log2 R ratio (LRR) of each chromosome was calculated using a size-weighted mean of all segments mapping to the chromosome. A chromosome was declared gained if its LRR was greater than 0.2, lost if the LRR was less than -0.2, and balanced otherwise. Unlike GISTIC, gained and lost broad events were analyzed together. The significance of the frequency of each broad event was tested using the exact binomial test. Each broad event frequency was compared to the background frequency, which was determined from a robust regression of the observed frequencies with respect to gene content (i.e. number of RefSeq genes) across all chromosomes. This approach was motivated by GISTIC's broad event analysis.

SNP6 Copy Number Analysis

Affymetrix SNP6 CEL files were processed as previously described (Northcott et al., 2012b) (GEO accession GSE37384). Copy number states were estimated as described previously using the hg18 reference genome. Segmented copy number estimates from SNP6 arrays were processed for input with the GISTIC2 method (v6.2) using the default parameters (Mermel et al., 2011) for the identification of recurrent focal copy number events.

Clinical Correlation and Survival Analysis

Progression-free survival and overall survival was right-censored at 5 years and analyzed by the Kaplan-Meier method and p value were reported using the log-rank test. Associations between covariates and risk groups were tested by the Fisher's exact test. Continuous variables were tested using non-parametric measures, specifically the Mann-Whitney U test or Kruskal-Wallis test. The significance of chromosome arm frequencies were evaluated using the exact binomial test, comparing the observed frequency to the expected frequency derived from a robust regression of event frequency and gene content, in a similar manner to the 'broad analysis' in GISTIC2. All statistical analyses were performed in the R statistical environment (v3.2.3), using R packages survival (v2.37-7), and ggplot2 (v1.0.0).

Group 3 and Group 4 Analysis

K-means clustering was performed using the top 10,000 most variable methylation probes (determined by median absolute deviation) of Group 3 and Group 4 samples (n=470). Consensus clustering was obtained using the ConsensusClusterPlus R Bioconductor package (v1.24.0) (Wilkerson and Hayes, 2010) with 1,000 repetitions in the R statistical environment (v3.2.2). Similar approach was used on the top 10,000 most variable genes of this set of 470 Group 3 and Group 4 samples. In addition, the NMF method was run (as described above) for both expression and methylation data on the same set of Group 3 and Group 4 samples.

We identified the outlier samples moving from Group 3 to Group 4 from the gene expression and DNA methylation NMF results using the following rule. We identified at k=2 the Group 3 and Group 4 clusters using the known subgroups of the samples (each group had a larger proportion of samples of a particular subgroup). At k=3, we identified which cluster(s) are largely composed of Group 3 and Group 4 (two Group 3 and one Group 4 clusters for the expression data, and one Group 3 and two Group 4 clusters for the DNA methylation data, Figure S1G). Then we counted the number of samples that were initially considered to be of a particular subgroup for k=2 and moved to be in another subgroup at k=3 (Figure 1D). Similar approach has been used to detect the outlier samples moving from Group 3 to Group 4 in the k-means consensus clustering (Figures 1D and S1H).

Similarity Network Fusion Analysis (SNF)

The Similar Network Fusion (SNF) method was run on 763 primary tumor samples using both gene expression and DNA methylation data (Wang et al., 2014). The SNF method does not require any prior feature selection so we used the full matrix of gene expression (21,641 genes) and the full matrix of methylation data (logitB values, 321,174 probes). We used the SNFtool R package (v2.2.0) with the parameters K = 50, alpha = 0.6, T = 50. Spectral clustering implemented in the SNFtool package was run on the SNF fused similarity matrix to obtain the groups corresponding to k=2 to 20.

We obtained four cluster at k=4 corresponding to the four medulloblastoma subgroups; WNT (n= 70), SHH (n=233), Group 3 (n=144), Group 4 (n=326). For each of these four subgroups we then ran the SNF method independently with the following parameters and clustered the resulting fused similarity matrix with spectral clustering using k=2 to 8.

Parameters:

WNT: K = 10, alpha = 0.6, T = 50

SHH: K = 40, alpha = 0.6, T = 50

Group 3: K = 40, alpha = 0.6, T = 50

Group 4: K = 60, alpha = 0.6, T = 50

Group 3 and Group 4: K = 80, alpha = 0.6, T = 50

We identified the top associated genes and methylation probes that have the largest agreement with the final fused network structure. To do so we computed the Normalized Mutual Information (NMI) score (as part of the SNFtool package) for each feature (i.e each gene and methylation probe). For each feature, we constructed a patient network based on the feature alone and subsequently used spectral clustering. We then compared the result of the resultant clustering to the one obtained from the whole fused similarity matrix by computing the NMI score as previously described (Wang et al., 2014). As mentioned in this paper, a score of 1 indicates the strongest feature and shows that the network of patients based on the given feature leads to the same groups as the fused network. A score of 0 means that there is no agreement between the groups that can be derived from the feature and the fused network groups. We therefore ranked all features according to their NMI scores that represent their importance for the fused network. We then selected a list of top 1% and top 10% features (also called associated genes and methylation probes) for each dataset (Figure 2 and S2A–S2D) for subsequent analysis. Those top features have expression or methylation patterns that are the most informative when determining our final subtypes using individual features.

Groups Visualization Using Stratomex

We used the StratomeX tool as part of the Caleydo suite (v3.1.5) to visualize the grouping of samples and the relationship between the groups resulting from different datasets, methods and/or parameterization of clustering (Streit et al., 2014; Lex et al., 2012). Sample group labels obtained by spectral clustering of the SNF fused similarity matrix or independent NMF clustering was imported to StratomeX software. The groups were colored according to the subgroup or subtype (if any) and reordered to show the relationship between the different clustering results (columns). In this study, we only used StatromeX for visualization and did not use its analytical functionalities.

Network Visualization with Cytoscape

From the fused similarity matrix returned by the SNF method, we retrieved all the patient pairs for which the values (W) was superior to the median values of all W pairs and imported those paired in Cytoscape (v3.2.0) (Shannon et al., 2003). We used the edged-weighted Spring embedded layout with the W values for visualization showing the edges in Figure 1B, and hiding the edges to only show the nodes (i.e patients) for Figures 3A, 4A, 5A, and 6A.

Relationship between Associated Genes and Probes

We evaluated the relationship between the gene expression features and the DNA methylation probe features in each subgroup. We applied the MethylMix R Bioconductor package (Gevaert, 2015) developed to identify potential cancer driver genes affected by hypo or hypermethylation changes, i.e. looking for anti-correlation between the methylation level and gene expression levels across samples. We obtained the probes annotations for hg38 from Zhou et al. (Zhou et al., 2016, Online supplemental data, http://zwdzwd.github.io/InfiniumAnnotation). We focused on probes within 1500 bp of the transcription start site (TSS) and identify 1342, 1573, 1673 and 1673 candidate driver genes for WNT, SHH, Group 3 and Group 4, respectively. Among those, 8, 18, 13 and 28 WNT, SHH, Group 3 and Group 4 genes, respectively, where in our features genes and had anti-correlated probes present in the top DNA methylation features, representing therefore only 3.7, 8.3, 6 and 13% of the feature genes (Figure 2C).

Pathway Enrichment Analysis

Pathway enrichment analysis was performed with g:Profiler and visualized as Enrichment Map in Cytoscape (Reimand et al., 2016; Merico et al., 2010; Shannon et al., 2003). We considered the top 10% associated genes (as described above) that were the most relevant for the final subtypes. For each subtype, we ranked up-regulated genes by their z-scores and analyzed the resulting gene lists with the ordered query setting of g:Profiler using pathways and processes with more than 5 and up to 1000 genes. Multiple testing correction was conducted with the default method of g:Profiler. Biological processes from the Gene Ontology, pathways from Reactome and KEGG, and protein complexes from CORUM were included in the enrichment analysis and other data sources were excluded. Electronic annotations (IEA) from Gene Ontology were excluded to only cover high-confidence gene annotations. Processes and pathways with g:profiler FDR corrected q values <0.05 were considered significant. Enriched categories were further filtered: pathways and processes with less than three associated genes were discarded.

Enrichment maps represent biological processes and pathways enriched in subtype-specific up-regulated genes. Each node represents a process or pathway; nodes with many shared genes are grouped and labeled by biological theme. Nodes sizes are proportional to the number of genes in each process, in each subgroup. Process and pathways connected by edges have genes in common, shorter edges represent stronger edges with Jaccard and Overlap coefficient combined by the Enrichment Map app of Cytoscape at cutoff value 0.66. Nodes are colored according to the subtype in which the process is enriched; processes enriched in more than one subtype have multiple colors.

Enrichment map visualization was manually curated to group functionally similar groups of pathways and to remove redundant groups and singletons. Connected nodes and unconnected but actionable nodes are shown.

Classifier Description

In this study, we used seven classifiers based on diverse machine learning approaches. Ridge logistic regression (labeled as *Ridge LR*) is a regression model, assigning weight to each feature to make a binary prediction. L2 regularization shrinks the weights to avoid overfitting. Lasso logistic regression (labeled as *Lasso LR*) works the same way as Ridge but uses L1 regularization instead, which sets some of the weights to zero, effectively performing feature selection again to avoid overfitting. Elastic net logistic regression (labeled as *Elastic Net*) also works similarly to Ridge but uses a linear combination of L1 and L2 regularizations and is able to select correlated features (through L2) while still performing feature selection (setting some of the weights to zero) through L1. Decision tree (labeled as *Decis.Tree*) utilizes a tree-structured graph with inner nodes representing decision rules and end nodes representing the classification decisions. Each path from root to a leaf in such a tree represents a classification rule. The individual decision rules are selected according to the information gain criterion. Random forest (labeled as *Rand.Forest*) uses an ensemble of decision trees to make classification predictions. Each decision tree uses a random subset of features trained on a bootstrapped set of samples. The output is the mode of the classification from all decision trees in the random forest. Support Vector Machines (SVM) make classification predictions by first transforming the data according to a chosen kernel and then constructing a maximum margin classifier such that the different classes are separated by the decision hyperplane as much as possible. SVM with linear kernel (labeled as *SVM lin*) performs a linear transformation of the data, whereas SVM with radial basis function kernel (labeled as *SVM rbf*) performs a Gaussian transformation of the data.

Prior to training any of the classifiers, we used Kruskal-Wallis H test, also know as ''one-way ANOVA on ranks'' to constrain the feature space. This way we selected top 1% of genes (resulting in 216 genes) and top 1% of CpG methylation probes (resulting in 3212 methylation probes) whose expression and methylation, respectively, is most predictive of the cluster assignment (done by the spectral clustering on the SNF fused similarity matrix) of samples in the training set. This feature selection procedure was repeated in each training / testing split of the data set, using the training set only.

All analyses were performed in R version 3.2.3. We used the glmnet package for Elastic Net, Lasso, and Ridge; the rpart package for Decision tree; the randomForest package for Random forest, the kernLab package for SVM. Training of Random forest and SVM was done using the caret package. The AUPRC (area under the precision-recall curve) values were calculated using the PRROC package.

Training and Selection of the Classifiers

We performed five classification tasks: the medulloblastoma subgroup classification, and then subtype classification within each of the four medulloblastoma subgroups. Cluster assignment by spectral clustering on the SNF fused similarity matrix was taken as the ground truth label assignment for the study cohort subgroup and subtype classification. For each of these tasks we trained 7 classification models using the concatenation of the top 1% expression and the top 1% methylation features as feature set.

For each task, we split the study cohort data set randomly to 70% training set and 30% testing set splits. The top 1% feature selection procedure, as described above, was then run on the training set. The selected features were used for both training and testing of the classifiers. Individual classification models were subsequently trained in 5-fold cross validation on the training set. On the testing set we measured the performance of the classifiers in the terms of classification accuracy and the area under the precision-recall curve (AUPRC). The entire described procedure was repeated 100 times. We report AUPRC and accuracy means and standard deviation over these 100 runs, as well as the average percentages of subtype predicted for the reference subtypes (Table S2).

COCA Analysis

We performed the COCA analysis as described in the TCGA pan cancer paper (Hoadley et al., 2014). We applied NMF clustering on gene expression and DNA methylation data individually for each subgroup. We proceeded to create a matrix of 0 and 1 with all the samples (as column) and the different groups (as row, one row per group obtained for each clustering). 1 indicated the presence of a sample in a group. This matrix was then clustered with k-means consensus clustering as performed in the TCGA pan cancer paper.

iCluster Analysis

We also performed multi-platform clustering using iCluster. We applied the R Bioconductor IClusterPlus package (the newest version of iCluster) to perform the analysis (Shen et al., 2009; Mo et al., 2013). It is necessary to select a set of features for each dataset to run iCluster. We tested selection of features on the maximum variance and on the MAD (median absolute deviation) and different percentages of features. We selected the top 15% most variable expressed genes and 1% most variable methylated probes as defined by median absolute deviation. We chose these numbers to allow for an equal representation of variable genes and methylated probes, which resulted in 3000 features per dataset. We performed multiple clusterings with different values of the lambda parameter and settled on Lambda =1. After performing the clustering, we confirm that almost all features are used to some degree in the model which implies that the results are not entirely driven by one data type. Indeed, this reassured us that the parameters we selected would allow for a robust multi-platform integrated analysis.

When applying iCluster across the entire dataset, we are unable to recover the 4 subgroups of medulloblastoma at k=4. When comparing the demographics of these 4 groups, and cross referencing to the SNF subgroups, WNT and Group 3 cluster together with two SHH groups emerging. When we increased to 5 groups we are able to clearly split WNT and Group 3. To determine the congruence between iCluster and SNF in defining the subtypes of subgroups, we first defined the subtypes using SNF, and then applied iCluster individually to each subgroup. Overall the subtypes as defined by iCluster were in agreement with SNF/Spectral clustering groups in 72-84% of instances. When we take into account that in some instances, iCluster recovered similar subtypes at a different number of groups, then the agreement increases to 74-90% (for example, some groups in iCluster split in two but correspond strongly to one cluster by SNF).

DATA AND SOFTWARE AVAILABILITY

The expression and methylation array data has been deposited in GEO under the accession number GSE85218. The previously published data is available in GEO under the accession numbers GSE37382 and GSE37384.

Cancer Cell
Previews

From One to Many: Further Refinement of Medulloblastoma Subtypes Offers Promise for Personalized Therapy

Abhishek Bavle[1,2] and D. Williams Parsons[1,2,*]
[1]Section of Hematology/Oncology, Department of Pediatrics, Baylor College of Medicine, Houston, TX 77030, USA
[2]Texas Children's Cancer Center, Houston, TX 77030, USA
*Correspondence: dwparson@bcm.edu
http://dx.doi.org/10.1016/j.ccell.2017.05.013

There is significant intertumoral heterogeneity within the four molecular subgroups of medulloblastoma. In this issue of *Cancer Cell*, Cavalli et al. apply similarity network fusion to gene expression and DNA methylation data to identify 12 medulloblastoma subtypes with distinct molecular and clinical profiles, making an important step toward molecularly tailored therapy.

Medulloblastoma (MB) is the most common malignant brain tumor in children (Ostrom et al., 2014). Historically, MB patients have been stratified as average risk (AR) or high risk (HR) based on clinical features and tumor histopathology, with HR-MB patients receiving higher doses of radiation therapy (RT). With conventional therapy—i.e., maximal safe tumor resection, RT to the whole brain and spine, and chemotherapy—5 year overall survival (OS) for AR-MB and HR-MB are ~80% and ~70%, respectively (Gajjar et al., 2006).

Two fundamental challenges must be overcome to improve the care of children with MB. The first is to identify MB patients who can be treated effectively on regimens that either omit or reduce dosing of RT. Being cured of MB comes at a significant neurocognitive cost to survivors, with decreases in intelligence quotient (IQ) and cognitive functioning that correlate with higher RT dose and younger age at treatment (Ris et al., 2001). A reduction in radiation therapy has been successfully accomplished without significantly compromising survival for one specific subset of MB patients under the age of 5 years (infant MB): those with desmoplastic nodular or medulloblastoma with excessive nodularity (DNMB/MBEN) architecture (Rutkowski et al., 2010). Unfortunately, this group accounts for only a minority of MB patients.

The second challenge is to improve survival for MB patients who do not respond well to current therapies. It has long been known that MB is a very heterogeneous disease with varied clinical outcomes. In the last decade, our understanding of the biology underlying this heterogeneity has improved exponentially after multiple studies showed that MB can be classified into discrete subgroups based on gene expression or DNA methylation profiling, culminating in the identification of four subgroups with distinct molecular profiles and correlated clinical outcomes (Figure 1A): WNT, Sonic Hedgehog (SHH), Group 3, and Group 4 (Kool et al., 2012; Northcott et al., 2011; Ramaswamy et al., 2016). WNT-subgroup MB has the best prognosis, with a 5-year OS >90% for average-risk disease, whereas Group 3 MB has the worst prognosis, especially when associated with *MYC* amplification. While SHH subgroup and Group 4 MB patients are considered to have an intermediate prognosis overall, studies have demonstrated that there is a wide variation in patient outcomes within each subgroup (Ramaswamy et al., 2016; Zhukova et al., 2013). A recent consensus statement proposed to redefine the risk stratification of MB into four groups: low, average, high-risk, and very-high-risk patients (Ramaswamy et al., 2016). A salient feature of this new classification system is that tumors from the same molecular subgroup can fall into different risk groups based on the presence or absence of certain molecular and clinical features. For example, studies have shown that in the SHH subgroup, patients with tumors with *TP53* mutation have a dismal prognosis, whereas younger patients (<3 years) whose tumors are *TP53* wild-type have a more favorable outcome (Zhukova et al., 2013). A better biological understanding of the heterogeneity within these subgroups is needed to reliably risk-stratify MB patients in order to identify high-risk patients in need of novel treatment approaches and low-risk patients for whom therapy can be safely de-escalated to reduce long-term adverse sequelae.

In this issue of *Cancer Cell*, Cavalli et al. further define the intertumoral heterogeneity within each of the four known MB subgroups through the integrated molecular profiling of a large MB dataset (Cavalli et al., 2017). The investigators have utilized a similarity network fusion (SNF) approach to analyze genome-wide DNA methylation and gene expression data across 763 MB samples, identifying a total of 12 subtypes with distinct molecular and clinical features (Figure 1A). These subtypes could not be recapitulated using either DNA methylation or gene expression profiling alone, instead requiring the combination of the two methods.

This improved understanding of the intertumoral heterogeneity within MB subgroups is a crucial step toward improving outcomes for MB patients through personalized risk-adapted therapy. The current study by Cavalli et al. accounts for the disparity in outcomes previously noted in SHH-MB patients by delineating four SHH subtypes (Figure 1B): two with a good prognosis (SHH γ/infants; SHH δ/adults) and two with a poor prognosis (SHH β/infants; SHH α/children 3–16 years). Importantly, the SHH γ subtype consists of young patients (<3 years) with excellent survival, even for those with tumors that do not have the

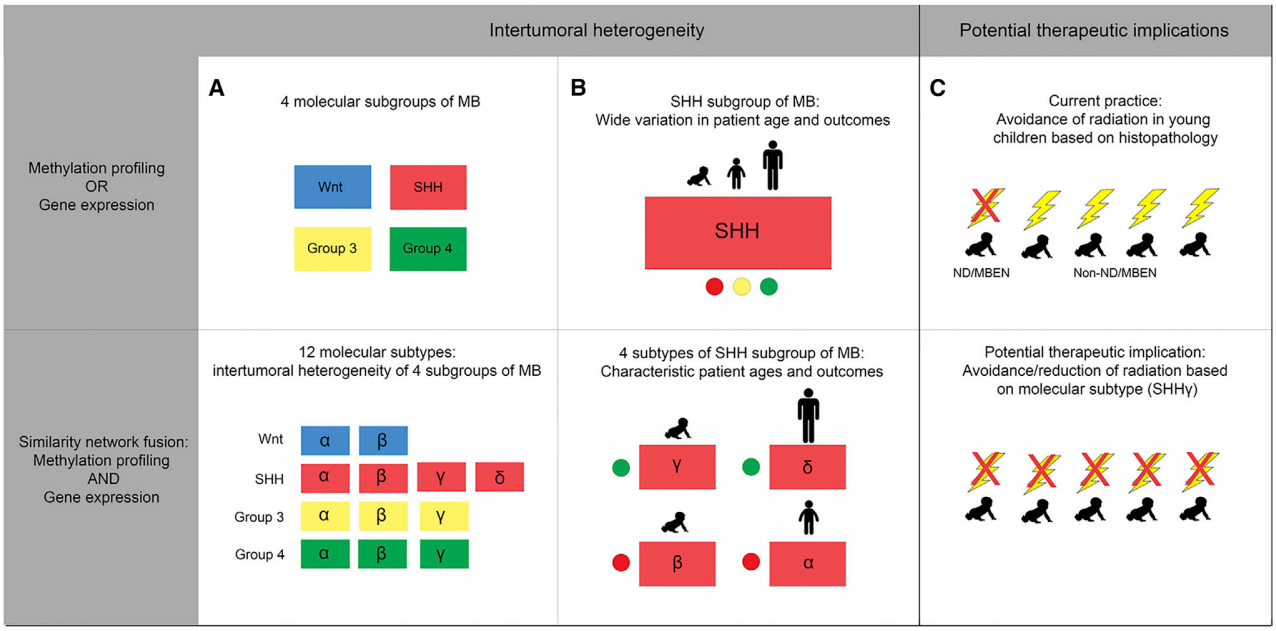

Figure 1. Use of Similarity Network Fusion to Characterize the Intertumoral Heterogeneity of Medulloblastoma
(A) Wnt, SHH, Group 3, and Group 4 are the four known molecular subgroups of medulloblastoma (MB). Similarity network fusion (SNF) was used to identify distinct subtypes within each subgroup. (B) There is wide variation in age at presentation and clinical outcomes (green, yellow, and red circles denote good, intermediate, and poor outcomes, respectively) for patients with SHH subgroup MB. SNF identified four distinct molecular subtypes within the SHH subgroup, each with characteristic age at presentation and clinical outcome. (C) Radiation can be avoided or deferred while maintaining good survival in young children with the DNMB/MBEN histology. The SHH γ subtype of MB occurs in young children and was associated with an excellent prognosis, irrespective of histopathology, potentially increasing the number of young patients for whom radiation might be reduced.

traditionally favorable MBEN histopathology, suggesting that the molecular signature of these tumors is a more powerful biomarker than histopathology alone and potentially broadening the group of young MB patients for whom radiation might be avoided without a compromise in survival (Figure 1C). On the other hand, this study also highlights the "bad players" among young MB patients who would likely not be good candidates for de-escalation of therapy. Infant SHH-MB (<3 years) patients who are not in the SHH γ subtype generally have SHH β tumors; these tumors are frequently metastatic and have multiple focal chromosomal amplifications, and these patients have a worse overall survival, meriting therapy escalation and/or novel treatment approaches. The 2016 World Health Organization (WHO) classification of central nervous system (CNS) tumors recognizes "SHH-activated and *TP53*-mutant" MB as a distinct entity based on previous evidence of the very poor prognosis of these tumors (Louis et al., 2016). Cavalli et al. take this a step further and show that *TP53* mutations are only prognostic in the SHH α subtype, compared to non-SHH α subtypes.

Another limitation of the current molecular subtyping of MB with either DNA methylation profiling or gene expression analysis alone is an overlap between Group 3 and Group 4 MB, as compared to WNT and SHH subgroups that are more distinct and have pathognomonic molecular aberrations. This ambiguity is reflected in the 2016 WHO classification of CNS tumors, which defines Group 3 and Group 4 subgroups as a single entity, "non-WNT/non-SHH MB" (Louis et al., 2016). The present study more clearly delineates these two subtypes, providing evidence that they are distinct from one another. Interestingly, Cavalli et al. found that the set of overlapping Group 3 and Group 4 tumors identified by DNA methylation profiling was different than that identified using gene expression analysis, suggesting that this is more a function of the testing modality rather than biology. Using SNF, the authors could make a clearer distinction between these two subgroups, with only 0.64% of samples not tracking back to their original subgroup.

Finally, the authors performed pathway enrichment analysis using the top 10% of associated genes across each of the 12 MB subtypes. Significantly enriched pathways were identified for all subtypes, including MAPK and FGFR1 signaling in Group 4β, RTK signaling in SHH γ, DNA repair pathways in SHH α, and pathways involved in protein translation in Groups 3β and 3γ. Many of these pathways are potentially targetable by novel agents, highlighting intriguing areas for future research in efforts to improve MB outcomes, especially for the subtypes with poor response to current conventional therapies.

This report from Cavalli et al. represents a significant contribution to the evolving understanding of MB as a group of genomically, biologically, and clinically diverse diseases. Moving forward, it will be critical to build upon these findings to develop biomarkers for identification of MB subtypes in the context of clinical trials, facilitating the prospective study of outcomes in uniformly treated patient populations and stratification of therapies tailored to the clinical and molecular features of each subtype. De-escalation of therapy could be evaluated for subtypes with an excellent prognosis, such as the WNT and SHH γ subtypes. Conversely, for

subtypes associated with poor response to conventional therapies, novel treatment approaches and agents targeting implicated pathways can be investigated.

REFERENCES

Cavalli, M.G., Remke, M., Rampasek, L., Peacock, J., Shih, D., Luu, B., Garzia, L., Torchia, J., Nor, C., Morrissy, S.A., et al. (2017). Cancer Cell *31*, this issue, 737–754.

Gajjar, A., Chintagumpala, M., Ashley, D., Kellie, S., Kun, L.E., Merchant, T.E., Woo, S., Wheeler, G., Ahern, V., Krasin, M.J., et al. (2006). Lancet Oncol. *7*, 813–820.

Kool, M., Korshunov, A., Remke, M., Jones, D.T., Schlanstein, M., Northcott, P.A., Cho, Y.J., Koster, J., Schouten-van Meeteren, A., van Vuurden, D., et al. (2012). Acta Neuropathol. *123*, 473–484.

Louis, D.N., Perry, A., Reifenberger, G., von Deimling, A., Figarella-Branger, D., Cavenee, W.K., Ohgaki, H., Wiestler, O.D., Kleihues, P., and Ellison, D.W. (2016). Acta Neuropathol. *131*, 803–820.

Northcott, P.A., Korshunov, A., Witt, H., Hielscher, T., Eberhart, C.G., Mack, S., Bouffet, E., Clifford, S.C., Hawkins, C.E., French, P., et al. (2011). J. Clin. Oncol. *29*, 1408–1414.

Ostrom, Q.T., Gittleman, H., Liao, P., Rouse, C., Chen, Y., Dowling, J., Wolinsky, Y., Kruchko, C., and Barnholtz-Sloan, J. (2014). Neuro Oncol. *16*, iv1–iv63.

Ramaswamy, V., Remke, M., Bouffet, E., Bailey, S., Clifford, S.C., Doz, F., Kool, M., Dufour, C., Vassal, G., Milde, T., et al. (2016). Acta Neuropathol. *131*, 821–831.

Ris, M.D., Packer, R., Goldwein, J., Jones-Wallace, D., and Boyett, J.M. (2001). J. Clin. Oncol. *19*, 3470–3476.

Rutkowski, S., von Hoff, K., Emser, A., Zwiener, I., Pietsch, T., Figarella-Branger, D., Giangaspero, F., Ellison, D.W., Garre, M.L., Biassoni, V., et al. (2010). J. Clin. Oncol. *28*, 4961–4968.

Zhukova, N., Ramaswamy, V., Remke, M., Pfaff, E., Shih, D.J., Martin, D.C., Castelo-Branco, P., Baskin, B., Ray, P.N., Bouffet, E., et al. (2013). J. Clin. Oncol. *31*, 2927–2935.

Paradoxical Effects of MLL Paralogs in MLL-Rearranged Leukemia

Michael J. Thirman[1,*]
[1]Section of Hematology/Oncology, Department of Medicine, University of Chicago, Chicago, IL 60637, USA
*Correspondence: mthirman@medicine.bsd.uchicago.edu
http://dx.doi.org/10.1016/j.ccell.2017.05.014

Conflicting data exist on the requirement for wild-type MLL1 in MLL-rearranged leukemia. In this issue of *Cancer Cell*, Chen et al. describe complementary approaches demonstrating that MLL1 is dispensable for MLL-fusion-mediated leukemogenesis. They also observe an unexpected role for MLL2 in MLL-rearranged leukemia cells and identify potential therapeutic targets.

11q23 translocations result in the formation of *MLL1* fusion genes that act as potent drivers of acute myeloid and acute lymphoblastic leukemia and confer a poor prognosis. MLL1 fusion proteins, which are formed as a result of these translocations, contribute to leukemogenesis by imposing an aberrant transcription program. The critical consequence of 11q23 chromosomal translocations is the formation of a chimeric oncogenic transcription factor that retains the amino terminus of MLL1 but replaces carboxyl-terminal domains, including the SET domain, with sequences from its partner proteins (Figure 1). As a result of 11q23 gene rearrangements, MLL fuses in frame with more than 70 different partner proteins. The most common partners are AF4, AF9, ENL, AF10, and ELL, which together account for over 85% of all MLL-rearranged leukemias. AF4, AF5q31, ENL, AF9, and ELL form a super elongation complex (SEC) that recruits the positive regulator of Pol II transcription elongation factor b (P-TEFb) kinase and the histone-3 lysine-79 methyltransferase DOT1L (Lin et al., 2010). The recruitment of the activities of the partner protein complex to MLL1 targets is a key molecular mechanism in MLL1 fusion protein-induced dysregulation of gene expression. Aberrant transcriptional elongation and H3K79 methylation lead to inappropriate activation of certain targets, including the *HOXA* cluster and *MEIS1*, that are critical to the transforming properties of MLL fusions.

Leukemia cells that harbor 11q23 translocations express one *MLL1* fusion gene and one wild-type (WT) *MLL1* allele. Prior studies on the importance of the remaining WT allele of *MLL1* in MLL1-fusion leukemia have yielded confounding results, leading Chen and colleagues (2017) in this issue of *Cancer Cell* to undertake a rigorous series of experiments to address this issue. MLL-rearranged leukemia cells also express *MLL2*, a paralog of *MLL1* that regulates distinct sets of target genes. Chen and colleagues also analyzed the role of MLL2 in MLL1-rearranged leukemia, which had previously not been examined.

MLL1 (KMT2A) is critical for the maintenance of expression of its target genes, and it mediates chromatin modifications associated with transcriptional activation. A SET domain in the carboxy terminus of MLL1, conserved with Set1 in *S. cerevisiae*, acts as a histone-3 lysine-4 (H3K4) methyltransferase. Germline deletion of *Mll1* resulted in embryonic lethality, with embryos exhibiting hematopoietic and skeletal defects, and loss of *Hoxa-7* and *Hoxc-9* expression (Yu et al., 1995). *Mll1* heterozygous mice exhibited growth retardation, anemia, thrombocytopenia,